Modelling excitation coupling in ventricular cardiac myocytes

Dissertation

zur Erlangung des akademischen Grades
Doctor rerum naturalium
(Dr. rer. nat.)
im Fach Biophysik

eingereicht an der
Lebenswissenschaftlichen Fakultät der Humboldt-Universität zu Berlin

von
Frau M. Sc. Janine Vierheller

Präsidentin der Humboldt-Universität zu Berlin:
Frau Prof. Dr.-Ing. Dr. Sabine Kunst

Dekan der Lebenswissenschaftlichen Fakultät
der Humboldt-Universität zu Berlin:
Herr Prof. Dr. Bernhard Grimm

Gutachter/innen:

1. Prof. Dr. Dr. h.c. Edda Klipp
2. Prof. Dr. Martin Falcke
3. Prof. Dr. Hermann-Georg Holzhütter

eingereicht am: 19.10.2017

Tag der mündlichen Prüfung: 20.03.2018

Abstract

Excitation contraction coupling (ECC) is of central importance to enable the contraction of the cardiac myocyte via calcium influx. The electrical signal of a neighbouring cell causes the membrane depolarization of the sarcolemma and L-type Ca^{2+} channels (LCCs) open. The amplification process is initiated. This process is known as calcium-induced calcium release (CICR). The calcium influx through the LCCs activates the ryanodine receptors (RyRs) of the sarcoplasmic reticulum (SR). The Ca^{2+} release of the SR accumulates calcium in the cytoplasm.

For many decades models for these processes were developed. However, previous models have not combined the spatially resolved concentration dynamics of the dyadic cleft including the stochastic simulation of individual calcium channels and the whole cell calcium dynamics with a whole cardiac myocyte electrophysiology model.

In this study, we developed a novel approach to resolve concentration gradients from single channel to whole cell level by using quasistatic approximation and finite element method for integrating partial differential equations. We ran a series of simulations with different RyR Markov chain models, different parameters for the SR components, sodium-calcium exchanger conditions, and included mitochondria to approximate physiological behaviour of a rabbit ventricular cardiac myocyte. The new multi-scale simulation tool which we developed makes use of high performance computing to reveal detailed information about the distribution, regulation, and importance of components involved in ECC. This tool will find application in investigation of heart contraction and heart failure.

Keywords: cardiac myocyte, calcium cycling, spatially resolved model, finite elements, stochastic, Markov chain, sarcoplasmic reticulum, sodium-calcium exchanger, mitochondria

Zusammenfassung

Um die Kontraktion einer Herzmuskelzelle durch den Kalziumeinstrom zu ermöglichen, ist die Kopplung von Erregung und Kontraktion (ECC) von zentraler Bedeutung. Durch das elektrische Signal einer Nachbarzelle wird die Depolarisation des Sarkolemmas verursacht, wodurch sich die L-Typ-Kalziumkanäle (LKK) öffnen und der Amplifizierungsprozess eingeleitet wird. Letzterer ist bekannt als Kalzium induzierte Kalzium Freisetzung (CICR). Durch die LKK wird ein Kalziumeinstrom in die Zelle ermöglicht, welcher zur Öffnung der Ryanodinrezeptoren (RyR) des Sarkoplasmatischen Retikulums (SR) führt. Durch die Kalziumfreisetzung des SR wird dieses im Cytoplasma akkumuliert.
Modelle für diese Prozesse werden seit mehreren Jahrzenten entwickelt. Bisher fehlte jedoch die Kombination aus räumlich aufgelösten Kalziumkonzentrationen der dyadischen Spalte mit stochastischen Simulationen der einzelnen Kalziumkanäle und die Kalziumdynamiken in der ganzen Zelle mit einem Elektrophysiologiemodell einer ganzen Herzmuskelzelle.
In dieser Arbeit entwickleten wir ein neues Modell, in welchem die Konzentrationsgradienten von einzelnen Kanälen bis zum Ganzzelllevel räumlich aufgelöst werden. Es wurde der quasistatische Ansatz und die Finite-Elemente-Methode zur Integration partieller Differentialgleichungen verwendet. Es wurden Simulationen mit unterschiedlichen RyR Markow-Kette-Modellen, verschiedenen Parametern für die Bestandteile des SR, verschiedenen Konditionen des Natrium-Kalzium-Austauschers und unter Einbindung der Mitochondrien durchgeführt. Ziel war es, das physiologische Verhalten einer Kaninchen-Herzmuskelzelle zu simulieren. In dem neu entwickelten Multiskalenmodell wurden Hochleistungsrechner verwendet, um detaillierte Informationen über die Verteilung, die Regulation und die Relevanz von den im ECC involvierten Komponenten aufzuzeigen. Zukünftig soll das entwickelte Modell Anwendung bei der Untersuchung von Herzkontraktionen und Herzmuskelversagen finden.

Schlüsselwörter: Herzmuskelzelle, Kalziumzirkulation, Räumlich aufgelöstes Model, Finite Elemente, Stochastisch, Markow-Kette, Sarkoplasmatisches Retikulum, Natrium-Kalzium-Austauscher, Mitochondrien

Contents

List of Figures

List of Appendix Tables

Abbrevations

Abbrevations	Explanation
ANT	Adenine nucleotide translocator
AP	Action potential
ADP	Adenosine diphosphate
APD_{90}	Action potential duration at 90 % repolarisation
ATP	Adenosine triphosphate
ATPase	Adenosine triphosphatase
BCL	Basic cycle length
CRU	Calcium release unit
CICR	Calcium-induced calcium release
CPU	Central processing unit
CVD	Cardiovascular disease
DI	Diastolic interval
ECC	Excitation contraction coupling
FAD	Flavin adenine dinucleotide
FDHM	Full duration at half maximum amplitude
FWHM	Full width at half maximum amplitude
GPU	Graphics processing unit
IMM	Inner mitochondrial membrane
IMS	Intermembrane space
jSR	Junctional sarcoplasmic reticulum
LCC	L-type calcium channel
MCU	Mitochondrial calcium uniporter
NAD	Nicotinamide adenine dinucleotide
NCX	Sodium-calcium exchanger
NCLX	Mitochondrial sodium-calcium exchanger
nSR	Network sarcoplasmic reticulum
ODE	Ordinary differential equation
OMM	Outer mitochondrial membrane
OMP	Outer membrane potential
PDE	Partial differential equation
PMCA	Plasma membrane Ca^{2+} ATPase
RyR	Ryanodine receptor
SCS	Specialized conduction system
SD	Standard deviation
SERCA	Sarcoplasmic reticulum calcium ATPase
SR	Sarcoplasmic reticulum
T-tubule	Transverse tubule
TCA cycle	Tricaboxylic acid cycle
VDAC	Voltage-dependent anion channel

1 Introduction

In 2013, almost one third of the deaths in the United States were accounted by cardiovascular diseases (CVDs), of which heart failure accounted for 36 % [7]. CVDs include coronary heart disease, cerebrovascular disease, peripheral vascular disease, congestive heart failure, hypertension, and valvular and congestive heart disease [8]. It has been predicted that by 2020 CVDs will become the leading cause of death and disability worldwide [9, 10]. Developing new prevention strategies and therapies requires a deep knowledge about the function of the heart in health and disease.

1.1 The cardiovascular system

The cardiovascular system is divided into the pulmonary circulation and the systemic circulation [8]. The heart pumps blood continuously through the blood vessels of both circulation systems providing the body with oxygen, nutrients, and other essential molecules and removing waste products [8]. The heart is covered and protected by the pericardium, a fluid-filled sac. From the outside to the inside, the heart wall is composed of the epicardium, the myocardium, and the endocardium. The myocardium is composed of muscle fibers made of cardiomyocytes or cardiac myocytes. The cardiac myocytes rely on available blood and electrical supply [11].
The mammalian heart consists of the right and left atria for receiving blood and the right and left ventricle to pump blood to the lungs and the body, respectively. The whole heart functions electrically and mechanically as a syncytium, which is enabled by intercalated discs [11]. The process of a single heart beat is described in [9]:
An electrical signal is generated in the specialized conduction system (SCS) tissue and conducted to the myocardium. Pacemaker cells and the sino-atrial node belong to the SCS tissue. Each single heart beat consists of a cardiac cycle, which is divided into the phases of systole and diastole. Systole is the contractile phase and diastole is the relaxation phase. The propagation of a membrane-based depolarizing action potential (AP) initializes the systole. The electrical signal travels along the SCS tissue to the atria, where it causes the atrial contraction and forces blood to the ventricles. The electrical signal travels from the atrioventricular node, which is a group of specialized cardiac myocytes slowing down the signal, over a more distal band of cardiac myocytes, known as His bundle, to the left and right bundles. Their smallest bundles are called Purkinje system fibers, which allow the activation of the ventricles. The contraction wave of the ventricular cardiac myocytes pumps blood into the pulmonary artery and into the arterial system.
The series of cellular events responsible for the contraction is described below.

1.2 The ventricular cardiac myocyte

The cardiac myocyte is an elongated cell with dimensions of $\sim$140 µm $\times <$ 20 µm in rabbits [11, 12]. The cells are electrically and mechanically interconnected by intercalated discs. The outer cell membrane, known as the sarcolemma, has many cylindrical invaginations known as transverse tubules (t-tubules) [13]. The sarcoplasmic reticulum (SR) is a luminal organelle spread throughout the entire interior of the cell. The SR forms terminal cisternae, which are either associated with the peripheral sarcolemma or with a t-tubule [14]. These cisternae make up the junctional SR (jSR) [14]. The SR

excluding the jSR is known as network SR (nSR) [14]. L-type calcium channels (LCCs) are preferentially located in the sarcolemma of the t-tubules [15]. Facing to the LCCs are the ryanodine receptors (RyRs), which are embedded in the membrane of the jSR. The RyRs form clusters of different sizes and irregular shape [13]. The short distance between the LCCs and the RyRs of 10 nm to 15 nm [13] is tightly regulated and sometimes modified in disease [16]. This small volume of cytoplasm between the sarcolemma and the jSR is called dyadic cleft. When including the LCCs and the RyRs it is referred to as calcium release unit (CRU). One ventricular myocyte has 10,000 - 20,000 such CRUs [11, 17, 18, 19] or maybe even as much as 50,000 CRUs [20]. The CRUs and the t-tubules are located at the z-discs, which act as an anchor for the sarcomeres [11]. Sarcomeres are the basic unit of striated muscle tissue and are composed of protein filaments [11].
The cardiac myocyte has three systems which are important for the contraction: (1) the sarcolemmal excitation system which propagates the AP, (2) the intracellular excitation contraction coupling (ECC) system which converts the electrical signal to a chemical signal and activates (3) the contractile system which is formed of chemical bridges of actin and myosin [8]. The membrane potential (V) is determined by the intra- and extracellular concentration of ions [21]. At rest the membrane potential of a ventricular cardiac myocyte has a value between -80 mV and -90 mV [8]. A transient, local depolarization of the membrane potential opens voltage-gated channels and generates ionic currents of sodium (Na^+), potassium (K^+), and calcium (Ca^{2+}) across the membrane [21]. The membrane potential reaches a peak value of $\sim$+40 mV and then repolarizes to the resting value by opening of concentration-dependent ion channels. The shape of a cardiac AP differs between different locations in the heart because it depends on the expression level of ionic channels [21]. It also differs largely between species because of variations in outward membrane currents [22]. Beat-to-beat alternans in Ca^{2+} transient amplitude (Ca^{2+} alternans) are observed during rapid electrical stimulation or under pathological conditions and linked with life-threatening ventricular arrhythmias [23].
The contraction of the heart is mediated by Ca^{2+} entering the muscle cell, activating the ECC system and binding to the myofilaments (see Figure 1). The depolarizing current of a neighbouring cell brings the membrane potential near the threshold for an AP [11]. The change of the membrane potential opens the voltage-dependent sodium channels, which cause a rapid, inward Na^+ influx [8]. The positive charge of the sodium ions further depolarizes the membrane voltage. This results in the opening of voltage-dependent LCCs and a relatively slow inward Ca^{2+} current increasing the local [Ca^{2+}] in the dyadic cleft [9]. The rise of the [Ca^{2+}] in the dyadic cleft activates the RyRs and large amounts of Ca^{2+} from the SR are released [24]. This process is known as calcium-induced calcium release (CICR) [13]. The triggered or spontaneous elementary Ca^{2+} release event by RyRs is known as Ca^{2+} spark [21]. The RyR openings cause a considerable rise of the local [Ca^{2+}] in the dyadic clefts. Ca^{2+} diffuses into the cytosol and the global [Ca^{2+}] ($[Ca^{2+}]_i$) is amplified. Ca^{2+} binds to troponin C of the myofilaments and initiates the contraction of the cell via the cross-bridge cycle [25]. The Ca^{2+} entered the cell during systole is extruded mainly through the sarcolemmal sodium-calcium exchanger (NCX) and through the sarcoplasmic reticulum calcium ATPase (SERCA) [13]. SERCA returns Ca^{2+} to the SR. The jSR is refilled by Ca^{2+} diffusion from the nSR [13]. As the $[Ca^{2+}]_i$ is restored to its diastolic value, Ca^{2+} dissociates from the troponin C and terminates the contraction [13].
Fundamental properties of ECC/CICR are [26]: (1) that through a mechanism of local control of CICR, a graded LCC current produces a graded RyR Ca^{2+} release [27, 28, 29],

(2) high whole cell CICR-gain at negative membrane potential and lower whole cell CICR-gain at positive membrane potential [30], (3) CICR is achieved by local Ca^{2+} release in highly localized cell-subcompartments, with dyadic cleft $[Ca^{2+}]$ rising to $\sim$1000$\times$ cytoplasmic $[Ca^{2+}]$ [31] and strong gradients inside the dyadic clefts [32, 33, 34], (4) stochastic transition rates of LCCs depending on membrane potential [35] and small fluctuations in the number of LCCs can result in variability of AP duration and in early after depolarisation formation [36].
Cardiac myocytes constantly require energy in form of adenosine triphosphate (ATP), which is almost exclusively produced by the mitochondria [37]. The most energy-consuming processes are cross-bridge cycle, Ca^{2+} re-uptake by SERCA, and basal cell metabolism [8]. Besides their important role for energy supply, mitochondria have also a role as Ca^{2+}-buffering compartments [38]. Ca^{2+} enters the mitochondria via the mitochondrial calcium uniporter (MCU) and leaves it via the mitochondrial NCX (NCLX).
Ca^{2+} is in a dynamic yet delicate balance and is highly regulated by multiple modulators [38]. Microdomains, which are small domains of transient or oscillatory ion accumulation [39], such as the dyadic cleft, and a local control of Ca^{2+} play a crucial role during ECCs by maintaining this balance. It is a challenging task to capture and understand such complex processes through experiments in order to deepen the knowledge about physiology, pathophysiology, and therapeutic implications. Furthermore, it is difficult to get human samples and experimental data of human cardiac myocytes. Rabbit cardiac physiology are similar to human physiology, because rabbits have comparably slow heart rates. Thus, rabbit cardiac myocytes provide a more adequate proxy for human cardiac myocytes compared to other laboratory animals, such as mice and rats [40].

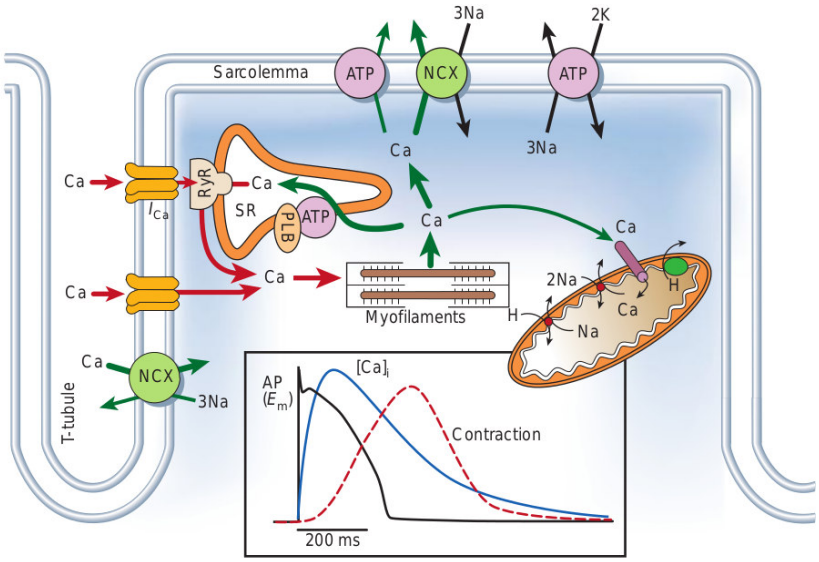

Figure 1: **Excitation contraction coupling in a cardiac myocyte:** Ca^{2+} cycling during systole (red arrows) and diastole (green arrows). Inset shows the time course of an action potential (black line), Ca^{2+} transient (blue line) and contraction (dashed red line) measured in a rabbit ventricular myocyte at 37°C. ATP - ATPase, NCX - Na^+/Ca^{2+}-exchanger, PLB - Phospholamban, RyR - Ryanodine receptor, SR - Sarcoplasmic reticulum. Figure by [38].

1.3 Controversies in cardiac myocytes

For many years, the role and function of Ca^{2+} in the cardiac myocyte has been the focus of research. As new details were detected, so proliferated models and hypotheses on Ca^{2+} handling and dynamics. Hence, there are still many controversies in cardiac myocyte Ca^{2+} electrophysiology, CICR, and ECC.
One principal controversy is by which robust mechanism the jSR Ca^{2+} release is rapidly terminated to guarantee a stable Ca^{2+} flux through the RyRs [13]. Many such mechanisms have been proposed from experimental and modelling studies, such as inactivation via Ca^{2+} binding, "stochastic attrition", decreased RyR sensitivity, and allosteric attrition [13]. The controversy remains, but the induction decay mechanism, which is also the simplest mechanism, is now widely accepted [13]. We conducted further testing for the feasibility of this mechanisms using our whole cell model.
The quantitative determination of SR Ca^{2+} dynamics are challenging, because approaches are based on many assumptions and few direct measurements [41]. Moreover, it is a requirement for all myocyte models that they must replicate known SR dynamics. Therefore, the parameters from single channels up to the compartments had to be defined and adjusted to match physiology. This is a major part of model development and is the basis for further analyses and model extensions.
Another issue of controversy is the potential multiple role of NCX in CICR. Its main role is the removal of Ca^{2+} from the cytoplasm, but an hypothesis arose that in its reverse mode, in which it brings Ca^{2+} into the cell, it could play a role in triggering CICR and even in contraction of cardiac myocytes [42]. Moreover, models suggest that NCX could decrease the Ca^{2+} spark frequency during diastole, which is only possible, if NCX is mainly located in and near the RyR clusters [43]. This assumption led to the hypothesis by Chu et al. (2016) [43] of a "dual-role hypothesis" for NCX: During diastole NCX extrudes Ca^{2+} released by spontaneous RyR openings and prevents regenerative Ca^{2+} release events. Then, during systole, NCX briefly operates in reverse mode and favours Ca^{2+} import and provides additional Ca^{2+} for CICR. To our knowledge, this hypothesis has not been tested yet. We developed a NCX model which is suited to investigate further the hypothesis by Chu et al. (2016) [43].
Mitochondria provide ATP for the ECC, which is a cellular process with a high energy demand. ATP production has to be coupled to the cardiac myocyte workload, but underlying mechanisms in the cell are still unclear. However, Ca^{2+} is often thought to be the key regulator [44]. Although the total Ca^{2+} uptake via MCU is relatively small, the close localisation of the mitochondria to the CRUs [45, 46] and to the SR [47, 48] could allow mitochondria to be regulated by locally high $[Ca^{2+}]$. Under this condition, Ca^{2+} might regulate energy supply by activating dehydrogenase enzymes, which increase NADH, and hence, ATP production [49]. Moreover, the regulation might be bi-directional meaning that the mitochondria could influence the CICR through their potential role as a buffer. This bi-directional feedback regulation is controversial and so far has not been demonstrated in an experiment or modelling setting, and appropriate models do not yet exist [13, 44]. Moreover, the kinetics of the mitochondrial channels, such as MCU, NCLX, and voltage-dependent anion channels (VDAC), are barely investigated. To this end we have extended the ODE-Mahajan model [6] by the addition of a simple, time-dependent mitochondria model. This model is suited to investigate the potential role of mitochondria as a Ca^{2+}-buffer space and its influence on CICR.

1.4 Modelling approaches

The high number of channels and compartments involved in processes in the heart and their complex interplay led to the evolution of diverse computational models. From single channel models, to individual cardiac myocyte models, and to tissue level models. These different modelling approaches focus on a variety of aspects and problems and are used to improve the understanding of heart function and dysfunction. Advances in modelling of single cells can help to build more realistic tissue and whole heart models [50]. The first model of excitable cells was developed by Hodgkin and Huxley (1952) [51] in their model of a nerve axon AP. Noble (1962) [52] modified this model and applied it to Purkinje cells. The first computational model of a ventricular cardiac myocyte was the Beeler-Reuter model (1977) [53]. This model and the model by McAllister et al. (1975) [54] formed the basis for the important DiFrancesco-Noble model (1985) [55]. It was the first model which described key features including Ca^{2+} transport via SERCA, Ca^{2+} extrusion by NCX, diffusion of Ca^{2+} from nSR to jSR, and CICR.
Often, the focus lays on ECC. Here, two main types of models can be classified: detailed models of a single or several dyadic clefts and whole cardiac myocyte models with simpler CRU descriptions. One type of cardiac myocyte models are the common-pool models in which Ca^{2+} fluxes through all LCCs and RyRs enter a common Ca^{2+} pool [27]. These models show an all-or-none release, but experiments by Fabiato (1985) [56] revealed a graded Ca^{2+} release and high CICR gain. Both are key physiological phenomena of ECC [23]. The first biophysically detailed common-pool model was developed by Luo and Rudy (1991) [57] for guinea pigs and was extended in 1994 with the addition of Ca^{2+} dynamics [58, 59]. Jafri et al. (1998) [60] complemented common-pool models by introducing a Markov chain model for the LCCs. Moreover, they subdivided the Ca^{2+} pool in a bulk and a dyadic space [60]. The Ca^{2+} subsystem was used by Winslow et al. (1999) [61] to develop a heart failure model.
Models showing graded Ca^{2+} release have to have LCCs which locally control the RyRs. The opening of the RyRs is caused by local, and not global, rise of $[Ca^{2+}]$ in the dyadic cleft. This effect is the core mechanisms of the ECC and known as local control theory of ECC and was first considered by Stern et al. (1999) [1] in their "calcium-synapse" model. In this model each dyadic cleft contained a single LCC and a single RyR. Many similar models (for example [62, 63, 60, 64, 65, 66]) were developed with similarly detailed Ca^{2+} dynamics, which emphasized the importance of the Ca^{2+} dynamics inside the dyadic cleft for the control of ECC. However, such stochastic models are computationally demanding [23].
It became generally accepted that the summation of single, local Ca^{2+} release events, known as Ca^{2+} sparks, results in the SR Ca^{2+} release [43]. Hence, models of Ca^{2+} sparks were developed. These models can explain a wide range of properties of CICR, ECC, and whole cell Ca^{2+} transients, but the mechanism of Ca^{2+} spark termination remains controversial [50]. Some models investigated the spatial spread of sparks (for example [67, 68, 69]). Other topics addressed in the literature are the regulation of cardiac proteins [70], Ca^{2+} alternans [6], Ca^{2+} waves [17, 71], and heart failure [61]. Other groups were interested in interval force relations [72] and the effects of β-adrenergic signalling [73]. Another modelling approach was to add further compartments, for example mitochondria, in which Ca^{2+} is localized [74].
Greenstein and Winslow [18] incorporated the local control of SR Ca^{2+} release in a model of cardiac AP, and thus, laid the foundation for multi-scale models. Therefore, they com-

bined 12,500 CRUs to the common-pool model of Winslow et al. [61]. The stochastic simulation of LCCs and RyRs was embedded in a set of ordinary differential equations (ODEs) describing the ionic currents, ionic concentrations and SR Ca^{2+} cycling [75]. Although, the model was computationally expensive, it was an important step towards whole cell models. The increasing interest in whole cell models demanded computationally more efficient methods, for example the quasistatic approximation based on separation of time scales and the reduction of the number of states for the Ca^{2+} channels [68, 76, 77]. Such models are applicable for long pacing and still reproduce a range of experimentally measured properties of ECC. Other reduction methods are simplified Monte Carlo ECC models [68], the probability density approach [78] and the moment closure technique [79]. The improvements in computer technology have allowed even highly complex models to be simulated in reasonable time scales. Approaches include parallel computing to distribute the data over several CPUs (central processing units) [80] or GPUs (graphics processing units) [17]. It has thus been possible to create realistic whole cell models with spatially distributed Ca^{2+} release sites and to produce physiological Ca^{2+} dynamics (for example [3, 80, 81, 82, 83, 84, 85, 86]). However, in these models the dyadic cleft is still represented by a single compartment without concentration gradients. Another modelling approach has been the development of detailed spatially resolved models of the CRUs (for example [34, 31, 87, 88]).
The model by Rovetti et al. (2010) [89] simulates the quasi-two-dimensional Ca^{2+} cycling in a network of 100 by 100 CRUs. These CRUs are coupled by Ca^{2+} diffusion of a nSR domain and a cytoplasmic domain and by the SR Ca^{2+} release and uptake [89]. Gaur et al. (2011) [90] simulated also 10,000 diffusively coupled CRUs with stochastic LCCs and RyRs. This model was used to implement a single sarcomere with equally distributed CRUs [91]. A model of a CRU with Ca^{2+} gradients and a t-tubule was developed by Cannell et al. (2013) [2]. A multi-scale model considering physiologically detailed description of the stochastic Ca^{2+} channels in a network of $\sim$20,000 CRUs was developed by Restrepo and colleagues [83, 84, 20]. Each CRU contains five subvolumes: a local cytosol, a submembrane space, a proximal space, a JSR space, and a nSR space [83]. However, the CRU is considered as a common-pool for Ca^{2+} gradients [23]. Sato et al. (2016) [92] improved this model, for example by increasing the number of RyRs to several hundreds, varying their number per CRU, and adding Ca^{2+} diffusion. They focused on how the spark duration depends on the number of RyRs per CRU [92]. Rajagopol et al. (2015) [93] modelled the spatial distribution of RyR clusters, myofibrils, and mitochondria based on three-dimensional electron microscopy data.
The number of parameters rises noticeably with increasing complexity and every compartment added to a model brings along its own parameters, which have to be adjusted. This makes a proper parameter choice difficult, especially in the case of Markov chain models of the channels which contain many parameters [50]. The higher the number of the Markov states, the higher is the number of kinetic parameters. Cells and experimental designs are highly variable, and therefore, there is usually a wide range of parameter values [50]. Moreover, some model organisms are better investigated than others and often a parameter value is known for one species but not for another.

1.5 Aims of this study

As outlined in the previous chapters, many attempts have been made to solve open questions regarding CICR and ECCs and there was great progress in the last decades, but

detailed models of dyadic clefts are often not able to predict global effects and less detailed whole cell models neglect local effects.
The first aim of the study is to develop a multi-scale, whole cell model of a rabbit ventricular myocyte, which captures the Ca^{2+} dynamics at the single channel level. This is recognised to be a challenging problem and demands high performance computing. However, this approach provides a highly useful tool to study Ca^{2+} spark dynamics, Ca^{2+} waves and the role of channels and single compartments in disease [21]. A detailed CRU model has not yet been coupled to whole cell Ca^{2+} dynamics and to whole cell electrophysiology, with a detailed representation of the spatial distributions of CRUs, challenges we address in this study. We developed a novel computational approach to resolve the concentration gradients from dyadic space to cell level by using a quasistatic approximation within the dyad and finite element methods for integrating the partial differential equations. The dimension of the computational domain can be defined by the number of z-discs and the number of CRUs. Each CRU has defined spatial coordinates and a defined number of RyRs and LCCs. Within each CRU, each RyR and LCC is modelled in a stochastic manner by Markov chain models. $[Ca^{2+}]$ and Ca^{2+}-buffers (troponin C, calmodulin, calsequestrin, Fluo-4) are spatially resolved. The membrane potential dynamics for a rabbit ventricular myocyte are modelled through the inclusion of the ODE model by Mahajan et al. (2008) [6]. Moreover, the electric field in the dyadic cleft caused by surface charges at the sarcolemma is considered [87]. The model is designed to be easily scalable by defining the number of z-discs, CRUs, and Ca^{2+} channels. Furthermore, it has a modular implementation so that submodels developed as modules can easily be exchanged. The stating concept was to develop a model with sufficient detail to model local effects of Ca^{2+} gradients and stochastic channel gating.
The second aim is to use the model to investigate controversies and areas of limited understanding of cardiac myocyte electrophysiology, CICR, and ECC, and by this means, to contribute to resolve knowledge gaps. We address questions concerning global cellular effects of the choice of channel model, the spatial distribution of channels, and mitochondria as Ca^{2+}-buffers on CICR and ECC. Therefore, we introduce our model and show how we address problems including modularity, performance, and multi-scale coupling in Chapter 2. Then, through simulating a subset of a ventricular cardiac myocyte, we investigate which RyR Markov chain model shows the best physiological behaviour when used in conjunction with our model in Chapter 3. We evaluate and adapt the most important parameters of the components of SR in Chapter 4. We use this improved model, showing more physiological Ca^{2+} dynamics, to investigate the distribution of NCX and its implications on its role in CICR in Chapter 5. Moreover, we investigate different models for Ca^{2+} channels of the mitochondria, and finally, we incorporate a mitochondria model in our whole cell model to investigate the role of mitochondria as Ca^{2+}-buffer in Chapter 6.

2 Whole cell model

2.1 Introduction

Our aim is to develop a detailed, spatially resolved stochastic simulation model for a ventricular cardiac myocyte. Modelling ECC of a cardiac myocyte is a multi-scale problem comprising several magnitudes of length and time scales. Our model simulates the whole cardiac myocyte electrophysiology of a rabbit, including stochastic gating dynamics of each Ca^{2+} channel, spatially detailed concentration dynamics in dyadic clefts, and a reaction-diffusion system of the cytosolic and sarcoplasmic free Ca^{2+} and Ca^{2+}-binding molecules. We aim to improve key features of our whole cell model, such as channels, pumps, and exchangers, with respect to experimentally measured properties and to extend our model through the addition of spatially resolved mitochondria.
In the mathematical model three separate concepts are coupled: (1) a system of partial differential equations (PDE) for the cytosolic and sarcoplasmic concentration dynamics, (2) N_c models for the individual CRUs, and (3) a system of ODEs for the electrophysiology (Figure 2). Later an ODE model of mitochondria was included in the whole cell model. These four models are first described as separate components, followed by their coupling to a whole cell model. The parameter values are listed in the Tables A.1 to A.5 and the parameter values for the mitochondria are listed in the Tables A.12 and A.13. The model description except for the mitochondria was published by us in [26].

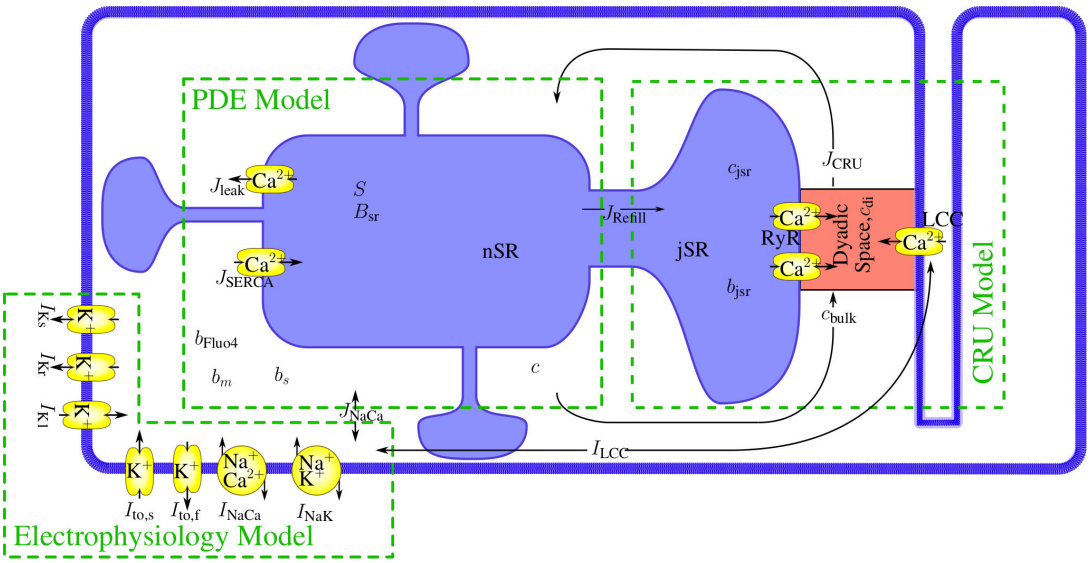

Figure 2: **The modules of the model and their interaction:** The PDE module comprises a set of PDEs for the bulk concentrations of cytosolic and sarcoplasmic free Ca^{2+}, cytosolic and sarcoplasmic mobile buffers, and a cytosolic stationary buffer. Each N_c Ca^{2+} release unit (CRU) is simulated individually and the combined Ca^{2+} fluxes are source terms in the PDEs for the bulk concentration dynamics. The $[Ca^{2+}]$ in the dyadic cleft is modelled in spatial detail with a quasistatic approximation, the dynamics of the concentrations of free Ca^{2+} and buffer in the jSR are determined by release into the dyadic cleft and refilling from the nSR. The electrophysiology model was developed by Mahajan et al. (2008) [6]. The LCC current in the CRUs and the NCX flux (J_{NaCa}) couple the membrane potential dynamics directly to the $[Ca^{2+}]$ dynamics.

2.2 Reaction-diffusion model

The reaction-diffusion model simulates the dynamics of the cytosolic $[Ca^{2+}]$ (c), which depends on Ca^{2+} transport across the sarcolemma, release and uptake by the SR, and binding to buffers. Sarcolemma Ca^{2+} transport is controlled by the Ca^{2+} channels of the CRUs and NCX. The t-tubules allow membrane fluxes, such as NCX (J_{NaCa}), to contribute to the bulk concentration dynamics. The J_{NaCa} through the sarcolemma ($J^{\mathrm{pm}}_{\mathrm{NaCa}}$) enters the PDEs as flux boundary condition. The flux J_{pump} describes the pumping of Ca^{2+} by SERCAs into the SR. The leak flux of the SR (J_{leak}) is attuned to establish a $[Ca^{2+}]$ of 0.1 µM during diastole and is modelled as:

$$J_{\mathrm{leak}} = f_{\mathrm{target}} \frac{V_P^{\max}(f_{\mathrm{target}} + K_p)}{S_0 - f_{\mathrm{target}}}, \tag{1}$$

where f_{target} is the target $[Ca^{2+}]$ of 0.1 µM, $V_P^{\max}$ is the maximum pump current of SERCA, S_0 is the resting SR $[Ca^{2+}]$, and K_P is the concentration at half-maximal uptake of SERCA. The J_{leak} can be switched off. In this case the stochastic RyR openings during diastole account for SR leak. Three Ca^{2+}-binding molecules ($b_j, j = s, m, f$) are included in the cytosol: troponin C as stationary buffer (s), calmodulin as mobile buffer (m), and Fluo-4 (f), which is used in experiments to measure the $[Ca^{2+}]_i$ of cells. The total concentration (b_j^{tot}) is spatially homogeneous for all three buffers. The PDEs for the cytosolic concentration fields and their boundary conditions are:

$$\frac{\partial c}{\partial t} = \nabla \cdot (\mathbf{D}\nabla c) + J_{\mathrm{cru}} + J_{\mathrm{NaCa}} + J_{\mathrm{leak}} - J_{\mathrm{pump}} - \sum_{j=m,s,f} R_j(c, b_j) \tag{2}$$

$$\frac{\partial b_j}{\partial t} = \nabla \cdot (\mathbf{D}_b^j \nabla b_j) + R_j\left(c, b_j\right), \quad j = s, m, f \tag{3}$$

$$\vec{n} \cdot \mathbf{D}\nabla c\big|_\Gamma = J^{\mathrm{pm}}_{\mathrm{NaCa}}$$

$$\vec{n} \cdot \mathbf{D}_b^j \nabla b_j\big|_\Gamma = 0, \quad j = s, m, f,$$

where $\mathbf{D}$ and $\mathbf{D}_b^j$ are diagonal diffusion matrices. We denote the sarcolemma by Γ, and the cell volume by $\nu_{\mathrm{cell}} \subset \mathbb{R}^3$. We simulate between 0.25 and 16 z-discs in a subvolume $\Omega < \nu_{\mathrm{cell}}$.

The expressions for the fluxes are:

$$R_j\left(c, b_j\right) = k_j^+ \left(b_j^{\mathrm{tot}} - b_j\right) c - k_j^- b_j, \quad j = s, m, f \tag{4}$$

$$J_{\mathrm{cru}} = \sum_{i=1}^{N_c} \frac{\nu_{\mathrm{cell}}}{\nu_{\mathrm{cyt}}} \frac{\Theta(R^i_{\mathrm{cru}} - |\vec{r} - \vec{r}_i|)}{\frac{4}{3}\pi \left(R^i_{\mathrm{cru}}\right)^3} \left[\sum_{j=1}^{N^i_{\mathrm{LCC}}} I^{i,j}_{\mathrm{LCC}}(t) + \sum_{j=1}^{N^i_{\mathrm{RyR}}} I^{i,j}_{\mathrm{RyR}}(t) \right] \tag{5}$$

$$J_{\mathrm{leak}} = V_l(S - c) \tag{6}$$

$$J_{\mathrm{pump}} = \frac{V_P^{\max} c^2}{K_P^2 + c^2}, \tag{7}$$

where $\Theta(x)$ denotes the step function:

$$\Theta(x) = \begin{cases} 0 & x < 0 \\ 1 & x \geq 0 \end{cases} \tag{8}$$

Ca^{2+} influx and release through LCCs ($I^{i,j}_{\mathrm{LCC}}(t)$) and RyRs ($I^{i,j}_{\mathrm{RyR}}(t)$) occurs in dyadic clefts. They are represented in the bulk dynamics by spherical source volumes with a

radius determined by the numbers of LCCs (N^i_{LCC}) and RyRs (N^i_{RyR}) in the dyadic cleft. Their dependence on time t is caused by their stochastic behaviour described in detail in Chapter 2.4.1. If an individual channel is open, its current obeys Equation (22) or Equation (23), and is 0 otherwise.
We use the bi-domain concept [94] for modelling cytosol and SR processes. It perceives both compartments to fill the same volume continuously with volume ratio $\nu_{\mathrm{cyt}}/\nu_{\mathrm{cell}}$ and $\nu_{\mathrm{sr}}/\nu_{\mathrm{cell}}$, respectively. We include the buffer calsequestrin (B_{sr}) in the SR lumen. The PDEs for the SR [Ca^{2+}] (S) and calsequestrin are:

$$\frac{\partial S}{\partial t} = \nabla \cdot (\mathbf{D}_S \nabla S) - k^+_{\mathrm{sr}} \left(B^{\mathrm{tot}}_{\mathrm{sr}} - B_{\mathrm{sr}}\right) S + k^-_{\mathrm{sr}} B_{\mathrm{sr}} - J_{\mathrm{jsr}} + \frac{\nu_{\mathrm{cyt}}}{\nu_{\mathrm{sr}}}(J_{\mathrm{pump}} - J_{\mathrm{leak}}) \quad (9)$$

$$\frac{\partial B_{\mathrm{sr}}}{\partial t} = \nabla \cdot (\mathbf{D}_B \nabla B_{\mathrm{sr}}) + k^+_{\mathrm{sr}} \left(B^{\mathrm{tot}}_{\mathrm{sr}} - B_{\mathrm{sr}}\right) S - k^-_{\mathrm{sr}} B_{\mathrm{sr}} \quad (10)$$

$$\vec{n} \cdot \mathbf{D}_S \nabla S|_\Gamma = \vec{n} \cdot \mathbf{D}_B \nabla B_{\mathrm{sr}}|_\Gamma = 0.$$

$\mathbf{D}_S$ and $\mathbf{D}_B$ are diffusion matrices. Release appears as the flux J_{jsr} in the S-dynamics, which refills the individual jSR. Their concentration (c^i_{jsr}) dynamics are described in the context of the CRU models (Equation (29)). The volume of the ith jSR is ν^i_{jsr}. The refill flux is localized within a spherical volume with radius R^i_{jsr} in the network SR:

$$J_{\mathrm{jsr}} = \sum_{i=1}^{N_c} \frac{\nu_{\mathrm{cell}} \nu^i_{\mathrm{jsr}}}{\nu_{\mathrm{sr}}} \frac{\Theta(R^i_{\mathrm{jsr}} - |\vec{r} - \vec{r}_i|)}{\frac{4}{3}\pi \left(R^i_{\mathrm{jsr}}\right)^3} \frac{S(\vec{r}_i) - c^i_{\mathrm{jsr}}}{\tau_{\mathrm{refill}}}. \quad (11)$$

2.3 Electrophysiology model

We use the AP model of a rabbit ventricular myocyte developed by Mahajan et al. (2008) [6]. We assume that the membrane potential is uniform over the computational domain. The dynamics of the membrane potential (V) is described by:

$$\frac{dV}{dt} = -\left(I_{\mathrm{ion}} + I_{\mathrm{stim}}\right). \quad (12)$$

I_{stim} is the stimulus current to depolarize the cell. I_{ion} comprises [6]:

$$I_{\mathrm{ion}} = I_{\mathrm{Na}} + I_{\mathrm{to,f}} + I_{\mathrm{to,s}} + I_{\mathrm{Kr}} + I_{\mathrm{Ks}} + I_{\mathrm{K1}} + I_{\mathrm{NaK}} + I_{\mathrm{CaL}} + I_{\mathrm{NaCa}}. \quad (13)$$

$\mathrm{I_{Na}}$ is the fast Na^+ current, $\mathrm{I_{K1}}$ is the inward rectifier current, $\mathrm{I_{to,f}}$ is the fast component of the rapid outward K^+ current, $\mathrm{I_{to,s}}$ is the slow component of the rapid outward K^+ current, $\mathrm{I_{Kr}}$ is the rapid component of the delayed rectifier current, $\mathrm{I_{Ks}}$ is the slow component of the delayed rectifier current, and $\mathrm{I_{NaK}}$ is Na^+/K^+ pump current. These currents and the equations defining them are described in detail in [6]. The NCX current I_{NaCa} is determined by the spatial integral of the corresponding fluxes in the cytosolic concentration dynamics:

$$I_{\mathrm{NaCa}} = \frac{\nu_{\mathrm{cyt}} F}{\nu_{\mathrm{cell}} C_m} \left(\frac{\nu_{\mathrm{cell}}}{\Omega} \int_\Omega J_{\mathrm{NaCa}} d\Omega + \frac{A_{\mathrm{cell}}}{\Gamma} \int_\Gamma J^{\mathrm{pm}}_{\mathrm{NaCa}}\, d\Gamma \right). \quad (14)$$

The LCC current I_{CaL} is the sum of all individual single channel currents (Equation (23)) from the CRU models:

$$I_{\mathrm{CaL}} = -2\alpha \sum_{i=1}^{N_c} \sum_{j=1}^{N^i_{\mathrm{LCC}}} I^{i,j}_{\mathrm{LCC}}. \quad (15)$$

The factor $\alpha = F\nu_{\text{cell}}/C_m\Omega$ converts the current in terms of ions/s into µA/µF and, at the same time, scales the currents up from values obtained with the simulation volume Ω, which is set by the number of simulated z-discs, to values corresponding to a realistic cell volume ν_{cell}. Similarly, the factor A_{cell}/Γ in Equation (14) scales the sarcolemma component from simulated (Γ) to whole cell area (A_{cell}). C_m is the cell membrane capacitance and F the Faraday constant.

2.4 CRU model

The original CRU model was developed by Schendel (2010) [87, 95]. We adapted the model to fit to our whole cell model. The CRU model consists of the dyadic cleft and the jSR. The dyadic cleft is modelled as a cylinder. We assumed a height of 15 nm with the LCCs protruding 2.5 nm such that there is a gap of 12.5 nm to the RyRs, which is in accordance with the literature [31, 96, 97]. Initially, the height of the RyRs was not considered, in Chapter 6 the height was set to 6.0 nm. The radius of a CRU depends on its number of channels. The rare T-type calcium channels and sparse RyRs outside the dyadic cleft are omitted. RyRs are arranged in regular arrays in nature [98]. In our model they are located at a distance of 30 nm of the channel centres at the top of the cylinder (see Figure 3). The LCCs are located on the bottom of the cylinder such that each LCC has the same distance to the four nearest RyRs. The LCC/RyR ratio was initially set to 1:4, since Chapter 4 to 1:5 [99]. We implemented an algorithm, which fills the channels from the inside to the outside in a spiral till the determined channel number is reached. The number of RyRs is randomly determined using an exponential distribution with a mean of 50, since Chapter 4 with a mean of 63 [100]. The diameter of each CRU is the diameter of its RyR array and a margin of 60 nm.

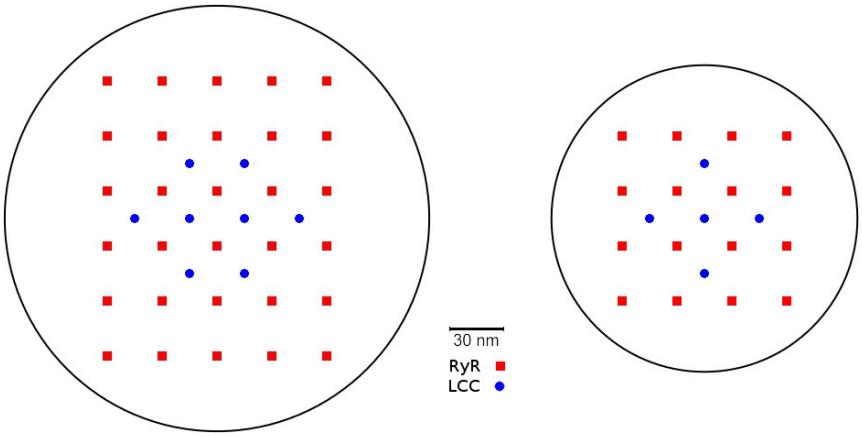

Figure 3: **Two examples for channel placement in the CRU model:** For 30 RyRs and 8 LCCs (left) and 16 RyRs and 5 LCCs (right). The number of RyR channels per CRU obeys an exponential distribution with an average of 50 (later 63) across all CRUs.

2.4.1 Stochastic channel gating

The LCCs and RyRs are simulated with a Markov chain model, the simplest Markov model. It simulates the current state of the channel with a random variable changing over time [101]. For the RyRs we investigated three existing models (see Chapter 3). The first is a model originally developed by Stern et al. (1999) [1] in it's modified version by Schendel (2010) [87]. It is a 4-state model (see Figure 4A(i)), including one open, one resting, and two inactivated states. It features RyR inhibition in case of high cytosolic or low jSR $[Ca^{2+}]$ (c_{jsr}). The second model is the 2-state model (see Figure 4A(ii)) developed by Cannell et al. (2013) [2], in which termination of CICR is mediated through the steep Ca^{2+} dependence of the RyR closed time. With a small decline in c_{jsr} the Ca^{2+} flux via open RyRs declines, causing a decline in local dyadic $[Ca^{2+}]$, which in turn causes a decrease in the open probability of neighbouring RyRs. This process is known as induction decay and is a biophysical mechanism for CICR termination. The third model is the 2-state model (see Figure 4A(iii)) developed by Walker et al. (2014) [3] (adapted from Williams et al. (2011) [85]), which incorporates modulation of the RyR-opening rate by c_{jsr}. This model has a fixed closing rate and, in accordance with the experimental data of Cannell et al. (2013) [2], there is only weak regulation of the RyR opening-rate when c^i_{jsr} is < 1 mM. Theoretically the opening rate of this last RyR model is unbound, however in our simulations opening rates larger than 0.7 ms^{-1} were not encountered. The precise definition of the transition rates for the three RyR models are given in [87], [2], and [3], respectively.

Schendel (2010) [87] used a 3-state LCC Markov chain model from Hinch et al. (2004) [76], which is a simplification of a 12-state model by Jafri et al. (1998) [60]. For the purpose of Schendels study the simple 3-state Markov chain model was sufficient, but for our whole cell model it is not. We wanted to run multiple APs and we had many, partly very large CRUs. On this scale slower kinetics, such as the voltage-dependent inactivation rate, are important and that is why a simple 3-state model was not appropriate for our whole cell model. We used the 7-state model developed by Mahajan et al. (2008) [6] (see Figure 4B), because this model exhibits Ca^{2+}-dependent and voltage-dependent inactivation and is fitted to experimental data from rabbit ventricular myocytes [6]. The transition rates are defined in [6] and the accompanying CellML data [102] for the LCC model. Note that there are slight discrepancies in the equations between the CellML data and the original paper; the equations we use are from the CellML data. In some cases we had to adjust the constants involved in the equations, which are listed in Table A.4.

Each initial channel's state was set to be closed, since Chapter 4 it was chosen randomly according to the steady state distribution for the initial values. The transition times between different states were determined using the Gillespie Algorithm for time dependent transition rates [103]. Each transition rate of the individual Markov chains is described by a propensity function and if the time crosses a random threshold by the integrated propensity, the transition occurs [103]. With the given rates of change in V and c, propensities are strongly time dependent. Hence, before we finally accept a calculated update of V and c, we verify that we have taken into account all events triggered by the propensity crossings of the update during the iteration step.

The frequency of transitions becomes very large with an increasing number of CRUs and with many channels in each CRU. While this in itself does not have a significant impact on the speed of the stochastic algorithm, it can force very small time steps on the PDE model. In order to alleviate this problem and allow for longer time steps we take

advantage of the properties of the stochastic process. Channel state transitions which do not represent openings or closings are, within a given iteration step, independent stochastic events. We can therefore execute an arbitrary number of such transitions in a single iteration. This approach scales almost independently of the total number of channel states. It is only dependent on the frequency of transitions from open to closed state or vice versa.

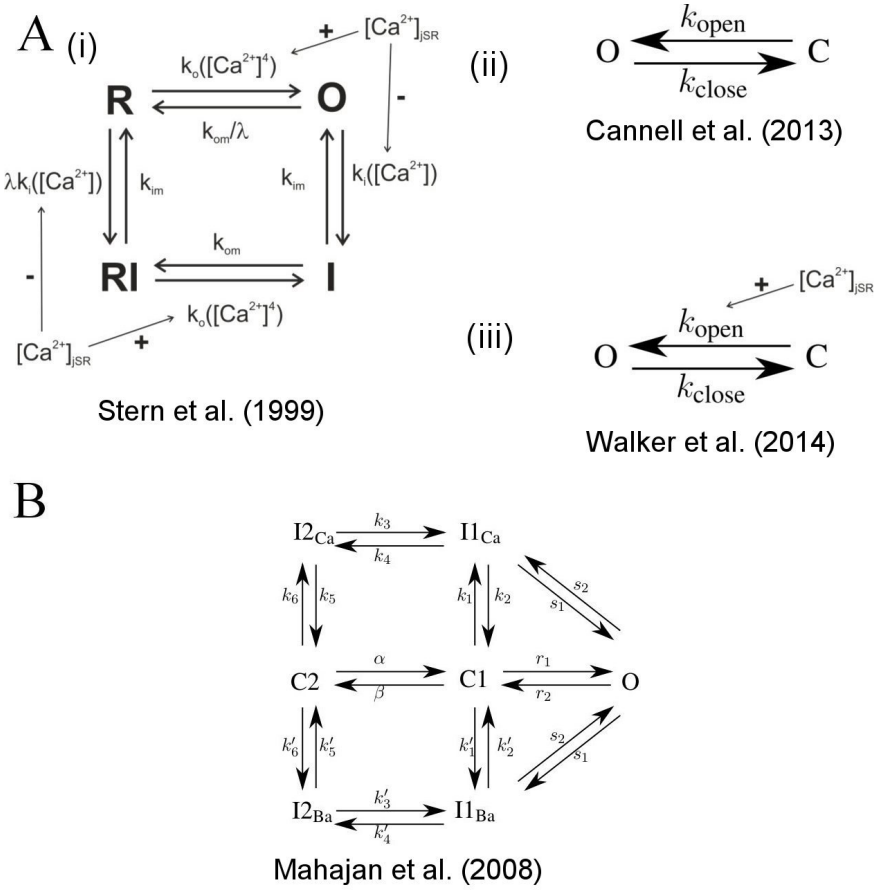

Figure 4: **State scheme for the RyR and LCC Markov chain models: A(i)** - 4-state RyR model of Stern et al. (1999) [1] (modified by Schendel (2010)[87]); O denotes the open, I the inactivated and R the resting state. The activation rate k_o is a fourth order Hill function of dyadic Ca^{2+}, the inactivation rate k_i is a first order Hill function of Ca^{2+}. The Ca^{2+} dependent rates are influenced by the Ca^{2+} concentration in the jSR. **A(ii)** - 2-state RyR model of Cannell et al. (2013) [2], where O denotes the open and C the closed state and k_{open} and k_{close} are polynomial functions of $[Ca^{2+}]$. **A(iii)** - 2-state RyR model of Walker et al. (2014) [3], where O denotes the open and C the closed state, k_{open} is a polynomial function of both $[Ca^{2+}]$ and $[Ca^{2+}]_{jsr}$ and k_{close} is a constant. **(B)** - 7-state LCC model of Mahajan et al. (2008) [6] with the states O open, $I1_{Ca}$, $I2_{Ca}$ Ca^{2+}-dependent inactivated states, C1, C2 closed states, $I1_{Ba}$, $I2_{Ba}$ Ca^{2+}-independent inactivated states (for details see [6]).

2.4.2 Ca^{2+} profile in the dyadic cleft

The $[Ca^{2+}]$ in the dyadic cleft (c_{di}) is modelled by the following equation in cylindrical coordinates:

$$\frac{\partial c_{di}}{\partial t} = \sum_{i=1}^{N_{\mathrm{LCC}}} J^i_{\mathrm{LCC}} + \sum_{j=1}^{N_{\mathrm{RyR}}} J^j_{\mathrm{RyR}} + D_c \Delta_{r,\varphi} c_{di}(\vec{r}) - \frac{\partial}{\partial z} J_z. \tag{16}$$

Because the time to reach the stationary concentration profile upon opening or closing of a channel is about one order of magnitude shorter than the time scale of channel state transitions, we assume a steady state for c_{di}. We make a separation ansatz (yielding only a negligible error as discussed in [87]):

$$c_{di}(r, \varphi, z) = f(r, \varphi) \cdot Z(z). \tag{17}$$

The large aspect ratio radius/height of the dyadic cleft renders gradients negligible in the z-direction of the cylinder due to channel fluxes [87]. However, electro-diffusion due to differential charge densities on t-tubule and jSR membrane causes a substantial gradient. Soeller and Cannell (1997) [104] determined the charge density profile shaping $Z(z)$. With their result we obtain:

$$Z(z) = e^{-2\phi_0 e^{-\kappa z}}. \tag{18}$$

The values of ϕ_0 and κ are listed in Table A.3. To find f we consider Equation (16) for a given configuration of open channels. The flux through the channels is constant due to the steady state assumption. We describe the channel fluxes as Dirac-δ-functions in space with the channel currents as pre-factors, integrate the equation over z and obtain:

$$\Delta_{r,\varphi} f(r, \varphi) = -\frac{1}{D_c h^*} \left[\sum_{i=1}^{N_{\mathrm{LCC}}} I^i_{\mathrm{LCC}} \delta(r - r_i, \varphi - \varphi_i) + \sum_{j=1}^{N_{\mathrm{RyR}}} I^j_{\mathrm{RyR}} \delta(r - r_j, \varphi - \varphi_j) \right], \tag{19}$$

where $h^* = \int_0^h Z(z) dz$[1]. Solving this using the Green function $G((r, \varphi), (r_i, \varphi_i))$ we find:

$$f(r, \varphi) - c_{\mathrm{bulk}} = \frac{1}{h^* D_c} \sum_{i=1}^{N_{\mathrm{LCC}}} I^i_{\mathrm{LCC}}\, G((r, \varphi), (r_i, \varphi_i)) + \sum_{j=1}^{N_{\mathrm{RyR}}} I^j_{\mathrm{RyR}}\, G((r, \varphi), (r_j, \varphi_j)) \tag{20}$$

$$G(\mathbf{r}, \mathbf{r_i}) = \frac{1}{2\pi} \log \left(\frac{\|\hat{\mathbf{r}}_\mathbf{i} - \mathbf{r}\|}{q \, \|\mathbf{r_i} - \mathbf{r}\|} \right) \text{ for } \mathbf{r_i} \neq 0$$

$$G(\mathbf{r}, 0) = \frac{1}{2\pi} \log \left(\frac{R}{\|\mathbf{r}\|} \right),$$

where R is the radius of the dyadic cleft, $q = \frac{R}{\|\mathbf{r_i}\|}$, and $\hat{\mathbf{r}}_\mathbf{i} = q^2 \mathbf{r_i}$. c_{bulk} is the $[Ca^{2+}]$ at the boundary of the dyadic cleft (cylinder barrel) as computed by the PDE model.
With

$$\eta(\vec{r_i}, \vec{r}) = \frac{Z(z)}{h^* D_c} G((r, \varphi), (r_i, \varphi_i))$$

c_{di} can be written as:

$$c_{di}(\vec{r}) = Z(z_i) c_{\mathrm{bulk}} + \sum_{i=1}^{N_{\mathrm{LCC}}} I^i_{\mathrm{LCC}}\, \eta(\vec{r_i}, \vec{r}) + \sum_{i=1}^{N_{\mathrm{RyR}}} I^i_{\mathrm{RyR}}\, \eta(\vec{r_i}, \vec{r}). \tag{21}$$

[1] A factor of h on the rhs of Equation (19) cancels with the same factor in the denominator of Equations (22) and (23) turning point sources into line densities.

The currents I^i_{LCC} and I^i_{RyR} depend themselves on the local [Ca^{2+}] at the channel mouth:

$$I^i_{\mathrm{RyR}} = g(c_{\mathrm{jsr}} - c_{di}(\vec{r}_i)) \qquad \text{for } i \in N_{\mathrm{RyR}} \tag{22}$$

$$I^i_{\mathrm{LCC}} = J_L \delta V \frac{c_{\mathrm{ext}} e^{-\delta V} - c_{di}(\vec{r}_i)}{1 - e^{-\delta V}} \qquad \text{for } i \in N_{\mathrm{LCC}} \tag{23}$$

with $\delta = 2F/(RT)$. Here $\vec{r}_i$ denotes the location of the mouth of the ith channel. Inserting Equations (22) and (23) into Equation (21) and evaluating it at each channel mouth defines a system of linear equations for the concentration values setting the currents for given values of c_{jsr} and c_{bulk}. The coefficients of that system can be calculated in advance of a simulation from the cleft geometry, which renders the simulation very efficient.

2.4.3 Buffers in the dyadic cleft

In order to employ the 2-state RyR models by Cannell et al. (2013) [2] and Walker et al. (2014) [3] (see Chapter 2.4.1) we found it necessary to introduce a form of Ca^{2+}-buffering in the dyadic cleft, because in the original papers the models were fitted to data from experiments conducted in the presence of buffers, such as calmodulin, Fluo-4, and ATP. Cannell et al. (2013) [2] used in their simulations high buffer concentrations within the dyadic cleft, and in order to adapt our model to this degree of buffering we introduce a linear buffer factor β. The coupling factor η now takes the form:

$$\eta(\vec{r}_i, \vec{r}) = \frac{1}{\beta} \frac{Z(z)}{h^* D_c} G((r, \varphi), (r_i, \varphi_i)). \tag{24}$$

We adjusted β so that the [Ca^{2+}] at the channel mouths and the average dyadic [Ca^{2+}] matched the values given in the paper by Cannell et al. (2013) [2]. An approximation of the $[Ca^{2+}]_i$ that would be measured by a single-wavelength Fluo-4 experimental recording (denoted as $[Ca^{2+}]^{\mathrm{exp}}_i$) was calculated from the Ca^{2+}-bound Fluo-4. The *in vitro* calibration approach described in [105] was used:

$$[Ca^{2+}]^{\mathrm{exp}}_i = K_d \frac{F - F_{\mathrm{min}}}{F_{\mathrm{max}} - F}, \tag{25}$$

where K_d is the dissociation constant of Fluo-4, F is the experimentally measured fluorescence intensity (here the [Ca^{2+}-bound Fluo-4]), F_{max} is the measured fluorescence intensity in Ca^{2+}-saturated dye (here this is set as the maximum [Ca^{2+}-bound Fluo-4] ($b^{\mathrm{tot}}_{\mathrm{Fluo\text{-}4}}$), and F_{min} is the measured fluorescence intensity in the absence of Ca^{2+} (here set to zero) (see Table A.1).

2.4.4 Ca^{2+} concentrations at the boundary of the dyadic cleft

The bulk [Ca^{2+}] (c_{bulk}) contributes to the [Ca^{2+}] of the dyadic cleft (see Equation (21)). At the end of each iteration of Equation (2) with the time increment Δt, c_{bulk} is fixed by its solution. However, the stochastic algorithm requires evaluation of the [Ca^{2+}] changes (Equation (2)) at intermediate time points, at which its solution is not known but the dyadic fluxes have changed. In Chapter 6 we used a linear estimate of c_{bulk} assuming c_{bulk} not to be constant during Δt, because of the fast concentration changes inside the dyadic cleft. We linearise all Ca^{2+} flux contributions around the CRU at the beginning of the time step. Then we compute the [Ca^{2+}] profile in a spherical shell with the radius R_{CRU}

+ L and inner radius R_{CRU}. In this volume the fluxes are given by the fluxes in the CRU's vicinity, the total flux from all channels of the CRU (J_{CRU}). The boundary conditions are given as Dirichlet boundary conditions at the outer surface, the concentration around the CRU (c^{far}_{bulk}), and as Neumann boundary conditions at the inner surface, as described by the following differential equation:

$$\frac{\partial c}{\partial t} = D\Delta c - kc \tag{26}$$

$$\left.\frac{\partial c}{\partial \overrightarrow{r}}\right|_{r=R_{CRU}} = J_{CRU} \tag{27}$$

$$c(R_{CRU} + L) = c^{far}_{bulk}, \tag{28}$$

where k is the linearisation of the external Ca^{2+} flux terms, J_{CRU} is the total channel flux from the channels in the dyadic cleft, c^{far}_{bulk} is the $[Ca^{2+}]$ outside the CRU. Solving Equation (26) yields the value $c_{bulk} = c(R_{CRU})$.

2.4.5 Modelling jSR dynamics

Each dyadic cleft is paired with its own jSR compartment. We assume spatially uniform Ca^{2+}concentration in the jSR. Ca^{2+}dynamics in the jSR depends on the release flux through the RyRs and a refill flux from the nSR, which we assume to depend simply on the concentration difference $S - c_{jsr}$. The buffering by calsequestrin is modelled using the fast buffer approximation.

$$\frac{dc_{jsr}}{dt} = \beta_{jsr}\left(\frac{S(\vec{r}) - c_{jsr}}{\tau_{refill}} - \frac{1}{\nu_{jsr}}\sum_{j=1}^{N_{RyR}} I^j_{RyR}\right) \tag{29}$$

$$\beta_{jsr} = \left(1 + \frac{nK_{csqn}B_{csqn}}{(K_{csqn} + c_{jsr})^2}\right)^{-1},$$

where $S(\vec{r})$ denotes the free network SR Ca^{2+}concentration at the location $\vec{r}$ of the spherical volume representing refilling in the S-dynamics of Equation (9). This equation is solved numerically by linearisation with very small time steps ($< 10^{-4}$ ms).
In Chapter 6 we consider the dependency of the jSR volumes ν^i_{jsr} on the number of RyRs in the corresponding ith CRU:

$$\nu_{jsr} = \frac{\nu_{jsr}}{\sum_{i=1}^{N_c} R_i^2} 2\pi R_i^2, \tag{30}$$

where ν_{jsr} is the total jSR volume, N_c is the number of CRUs, and R is the radius of the corresponding ith CRU.

2.5 Mitochondria model

In Chapter 6.3.1 we investigated the mitochondria model of a pancreatic β-cell developed by Magnus and Keizer (1997) [106]. The mitochondrial membrane potential ($\Delta\Psi$) is described by:

$$C_{mito}\frac{d\Delta\Psi}{dt} = -(-J_{H,res} + J_{H,F1} + J_{ANT} + J_{H,leak} + 2J_{uni}), \tag{31}$$

where C_{mito} is the inner membrane capacitance, $J_{\text{H,res}}$ is the H^+ efflux of the single-electron transfer, $J_{\text{H,F1}}$ is the H^+ uptake by F_1F_0-ATPase, J_{ANT} is the exchange flux of ADP_i and ATP_m by the adenine nucleotide translocator (ANT), $J_{\text{H,leak}}$ is the H^+ leak flux, and J_{uni} is the Ca^{2+} influx through MCU. The mitochondrial $[Ca^{2+}]$ (c_{mito}) is defined by:

$$\frac{d[c_{\text{mito}}]}{dt} = f_m(J_{\text{uni}} - J_{\text{NCLX}}), \tag{32}$$

where f_m is the fraction of free mitochondrial Ca^{2+} and J_{NCLX} is the Ca^{2+} flux through the mitochondrial NCX. The mitochondrial ADP concentration ($[ADP]_m$) is calculated by:

$$\frac{d[ADP]_m}{dt} = (J_{\text{ANT}} - J_{\text{p,F1}}), \tag{33}$$

where $J_{\text{p,F1}}$ is the ATP production by F_1F_0-ATPase. The H^+ efflux of the single-electron transfer is defined by:

$$J_{H,res} = 360\rho_{res}\frac{r_a 10^{6\Delta pH}\exp\left(\frac{FA_{res}}{RT}\right) - [r_a + r_b]\exp\left(\frac{g6F\Delta\Psi}{RT}\right)}{\left[1 + r_1\exp\left(\frac{FA_{res}}{RT}\right)\right]\exp\left(\frac{6F\Delta\Psi_B}{RT}\right) + \left[r_2 + r_3\exp\left(\frac{FA_{res}}{RT}\right)\right]\exp\left(\frac{g6F\Delta\Psi}{RT}\right)}. \tag{34}$$

The H^+ uptake by F_1F_0-ATPase is defined by:

$$J_{H,F1} = -180\rho_{F1}\frac{p_a 10^{3\Delta pH}\exp\left(\frac{FA_{F1}}{RT}\right) - [p_a + p_b]\exp\left(\frac{3F\Delta\Psi}{RT}\right)}{\left[1 + p_1\exp\left(\frac{FA_{F1}}{RT}\right)\right]\exp\left(\frac{3F\Delta\Psi_B}{RT}\right) + \left[p_2 + p_3\exp\left(\frac{FA_{F1}}{RT}\right)\right]\exp\left(\frac{3F\Delta\Psi}{RT}\right)}. \tag{35}$$

The exchange flux of ADP_i and ATP_m by the ANT is defined by:

$$J_{ANT} = J_{max,ANT}\frac{1 - \frac{[ATP^{4-}]_i[ADP^{3-}]m}{[ADP^{3-}]_i[ATP^{4-}]_m}\exp\left(\frac{-F\Delta\Psi}{RT}\right)}{\left\{1 + \frac{[ATP^{4-}]_i}{[APD^{3-}]_i}\exp\left(\frac{-fF\Delta\Psi}{RT}\right)\right\}\left\{1 + \frac{[ADP^{3-}]_m}{[ATP^{4-}]_m}\right\}}. \tag{36}$$

The H^+ leak flux is defined by

$$J_{H,leak} = g_H\Delta p. \tag{37}$$

The Ca^{2+} influx through MCU is defined by

$$J_{uni} = J_{max,uni}\frac{\frac{[Ca^{2+}]_i}{K_{trans}}\left(1 + \frac{[Ca^{2+}]_i}{K_{trans}}\right)^3}{\left(1 + \frac{[Ca^{2+}]_i}{K_{trans}}\right)^4 + \frac{L}{\left(1 + \frac{[Ca^{2+}]_i}{K_{act}}\right)^{na}}}\frac{\frac{2F(\Delta\Psi - \Delta\Psi*)}{RT}}{1 - \exp\left\{\frac{-2F(\Delta\Psi - \Delta\Psi*)}{RT}\right\}}. \tag{38}$$

The Ca^{2+} flux through the mitochondrial NCX is defined by

$$J_{NCLX} = J_{mean,Na^+/Ca^{2+}}\frac{\exp\left\{\frac{bF(\Delta\Psi - \Delta\Psi*)}{RT}\right\}}{\left(1 + \frac{K_{Na}}{[Na^+]_i}\right)^n\left(1 + \frac{K_{Ca}}{[Ca^{2+}]_m}\right)}. \tag{39}$$

The ATP production by F_1F_0-ATPase is calculated by

$$\begin{aligned} J_{p,F1} = -60\rho_{F1}&\left[p_a 10^{3\Delta pH} + p_{c1}\exp\left(\frac{3F\Delta\Psi_B}{RT}\right)\right]\exp\left(\frac{FA_{F1}}{RT}\right) \\ &- p_a\exp\left(\frac{3F\Delta\Psi}{RT}\right) + p_{c2}\exp\left(\frac{FA_{F1}}{RT}\right)\exp\left(\frac{3F\Delta\Psi}{RT}\right) \\ &\times\frac{1}{\left[p_1\exp\left(\frac{FA_{F1}}{RT}\right)\right]\exp\left(\frac{3F\Delta\Psi_B}{RT}\right) + \left[p_2 + p_3\exp\left(\frac{FA_{F1}}{RT}\right)\right]\exp\left(\frac{3F\Delta\Psi}{RT}\right)}. \end{aligned} \tag{40}$$

This model [106] was combined with the electrophysiology ODE-model developed by Mahajan et al. (2008) [6]. The $[Ca^{2+}]_i$ and the $[Na^+]_i$ of the ODE-Mahajan model is used as input parameters for the mitochondria model and the Ca^{2+} flux of the mitochondria is added to the $[Ca^{2+}]_i$ of the ODE-Mahajan model.
In Chapter 6.3.2 the mitochondria model by Magnus and Keizer (1997) [106] was included in our whole cell model. The mitochondria are modelled as cuboids with a dimension of 0.65 × 0.65 × 1.1 µm (including an overlap region), which yields a total mitochondria volume (ν_{mito}) of 27.885 µm^3 for 60 mitochondria of a quarter of one z-disc setup. This represents ∼24.8 % of the cell volume. We assumed that the mitochondrial membrane potential ($\Delta\Psi$) is uniform over the domain of each mitochondrion. The Ca^{2+} fluxes across the mitochondria membrane are solved in a 0.05 µm thick overlap region around the mitochondria and boundary conditions are not necessary. The $[Ca^{2+}]$ of this overlap region depends on the Ca^{2+} flux across the mitochondria membrane:

$$\begin{aligned}\frac{\partial c}{\partial \overrightarrow{n}} &= \nabla \cdot (\mathbf{D}\nabla c) + J_{\text{cru}} + J_{\text{NaCa}} + J_{\text{leak}} - J_{\text{pump}} - \sum_{j=m,s,f} R_j(c, b_j) \\ &\quad - \frac{\nu_{\text{mito}}}{\nu_{\text{cell}}} J_{\text{uni}} + \frac{\nu_{\text{mito}}}{\nu_{\text{cell}}} J_{\text{NCLX}}.\end{aligned} \tag{41}$$

$[Ca^{2+}]_{\text{mito}}$ depends on the cytosolic $[Ca^{2+}]$ in the overlap region and on $[Na^+]_i$. The $[Ca^{2+}]_{\text{mito}}$ is spatially resolved by the following PDE:

$$\frac{\partial [Ca^{2+}]_{\text{mito}}}{\partial \overrightarrow{n}} = \nabla \cdot (\mathbf{D}_{\text{mito}} \nabla c_{\text{mito}}) f_{\text{mito}} (J_{\text{uni}} - J_{\text{NCLX}}). \tag{42}$$

2.6 Module interaction

The modules interact on a time scale longer than a single iteration step by the dependencies of the dynamics on Ca^{2+}, V, and other state variables. Instantaneous interactions are important for the algorithmic realization of the time integration. We use for the completely coupled system an Euler forward method. The instantaneous interactions between the PDE system and the CRU models are mediated by Ca^{2+} currents and concentrations, between the CRU models and the electrophysiological model by the LCC current, and between the PDE system and the electrophysiological model via the bulk and sarcolemma components of the NCX flux (see also Figure 2).

2.6.1 Bulk concentrations - Electrophysiology

We use the spatially resolved $[Ca^{2+}]$ (c) at the sarcolemma for calculating local values of $J^{\text{pm}}_{\text{NaCa}}$ and analogously in the bulk for J_{NaCa}, and then average over the finite elements (Equation (14)) to obtain the current entering the membrane potential dynamics. Vice versa, $J^{\text{pm}}_{\text{NaCa}}$ serves as boundary condition and J_{NaCa} as bulk source term for the PDEs.

2.6.2 Bulk concentrations - CRUs

The value of the $[Ca^{2+}]$ (c) determined by the PDEs of the reaction-diffusion model is averaged along the rim of a dyadic cleft volume and then serves as boundary condition c_{bulk} in Equation (21) to determine the RyR and LCC currents ($I^{i,j}_{\text{LCC}}$ and $I^{i,j}_{\text{RyR}}$) in each CRU. Vice versa, these currents determine the source terms for the bulk concentration dynamics in Equation (2).

2.6.3 Bulk concentrations - Mitochondria

In Chapter 6.3.2 mitochondria were included in our whole cell model. The Ca^{2+} fluxes J_{uni} and J_{NCLX} of the mitochondria affect the $[Ca^{2+}]_i$ in the overlap region around the mitochondria (Equation (42)). Both fluxes depend on the cytosolic $[Ca^{2+}]$ of the overlap region and the $[Na^+]_i$.

2.6.4 Electrophysiology - CRUs

The membrane potential affects the LCC currents (Equation (23)) and vice versa the sum of all individual LCC currents the membrane potential (Equation (15)).

2.7 Numerical Approach

We used a piecewise bi-linear finite element method for the solution of the spatially three-dimensional reaction-diffusion model, including the complex distribution of CRUs at multiple z-discs. The first challenge was the fine scale resolution of the computational grid to resolve the strong concentration gradients at the boundary of the CRUs. We take the equidistant cubic elements with an edge length of 0.05 µm in our computations. The next challenge was to deal with the adaptive time stepping schemes for solving the reaction-diffusion systems. Due to the fast transitions of the channel openings/closings in a CRU, the time scales vary from tens of micro seconds to milliseconds. To resolve such rapid changes adaptive and higher order time steppings are inevitable to treat the very smooth diffusion effects as efficiently as possible. To this end, we use higher order linearly implicit Runge-Kutta methods for time discretization of reaction-diffusion systems, see [107, 108]. These belong to a large class of methods which try to avoid the non-linear system and replace it by a sequence of linear ones. Also, this allows the use of adaptive time scales in the simulations. Specifically, we employed a second order Rosenbrock method called ROWDA [107], and we avoid the time discretization implications of this problem as described in chapter 4.2 of [109].
Our parallel implementation of the discretization routines is based on the public domain package DUNE [110], especially the *dune-pdelab* discretization module. The parallel linear solvers depend on the *dune-istl* module. Based on this, we developed a finite element simulator to solve the whole cell Ca^{2+} cycling model. The internal parallel Cartesian (called Yasp) grid in DUNE is used for the parallel grid constructions. In our domain decomposition approach, the original domain is partitioned into subdomains and each subdomain is assigned to a single processor. In our computations, we used a non-overlapping domain decomposition approach to solve the discretized PDE model. In this regard, we parallelized our code by using minimum global communications for solving the stochastic part of the problem. The time discretization results in a system of linear equations which can be solved by using efficient iterative solvers. We use the BiCGSTAB [111] with Jacobi preconditioner as the linear solver with a relative tolerance of 10^{-6} as the stopping criteria for the linear solver at each step of the ODE time integrator.
Here we propose a novel technique to determine the new time step during the stochastic opening of many CRUs. Due to the presence of the large numbers of CRUs, the stochastic algorithm that governs the time step for the next channel transition plays an important role for the computations. As mentioned before, channel state transitions which do not represent openings or closings are, within a given iteration step, independent stochastic events. We can therefore execute several of them within a single iteration. Additionally,

typical time steps during an AP are in the range of 0.01 ms meaning they are shorter than the diffusion time between neighbouring CRUs. Consequently, conductance changing events in different CRUs are statistically independent on the time scale of a single iteration and we can allow for several of them in (distinct) CRUs within one time step.
We introduce two time steps: first the deterministic time step τ_{det} (which is allowed by the numerical integration of the PDEs) and second the stochastic time step τ_{stoc}. We propose the following algorithm:
The bulk Ca^{2+} cycling PDE model and the electrophysiology model are integrated from t to $t + \tau_{\text{det}}$, where τ_{det} is the accepted deterministic time step of the PDE solver. Then the stochastic channel transitions are predicted from t to $t + \tau_{\text{det}}$. Suppose there were N_s stochastic events for conductance changes at times $t + \tau_i$ where $i = 1 \dots N_s$, $\tau_i \leq \tau_{\text{det}}$, and $0 \leq N_s \leq N_c$. Here the time of the stochastic event is τ_i for the ith CRU. In case that there is no stochastic event for a CRU, τ_i is set to $\tau_i = \tau_{\text{det}}$. The stochastic time step τ_{stoc} is determined from the τ_i as the time by which a maximum number of acceptable transitions is reached. The maximum number has been determined empirically to be sufficiently small with 0.1 N_s to cause no essential difference to simulations with τ_{stoc} sufficiently small to guarantee $N_s = 1$. Now all the occurring events in the CRUs up to $t + \tau_{\text{stoc}}$ are set to take place at time $t + \tau_{\text{stoc}}$. By doing so, we avoid too small time steps. A schematic illustrating a single iteration and how the time steps are determined can be found in Figure 5.
In Chapter 6, we used a deterministic instead of the stochastic time stepping scheme, where $\Delta t_{\text{stoc}} = \Delta t$, to achieve speedup as the error between both time stepping schemes is much smaller than the difference between individual simulations.

We used R version 3.2.3 and ParaView version 4.3.1 and 4.4.0 to plot simulation results.

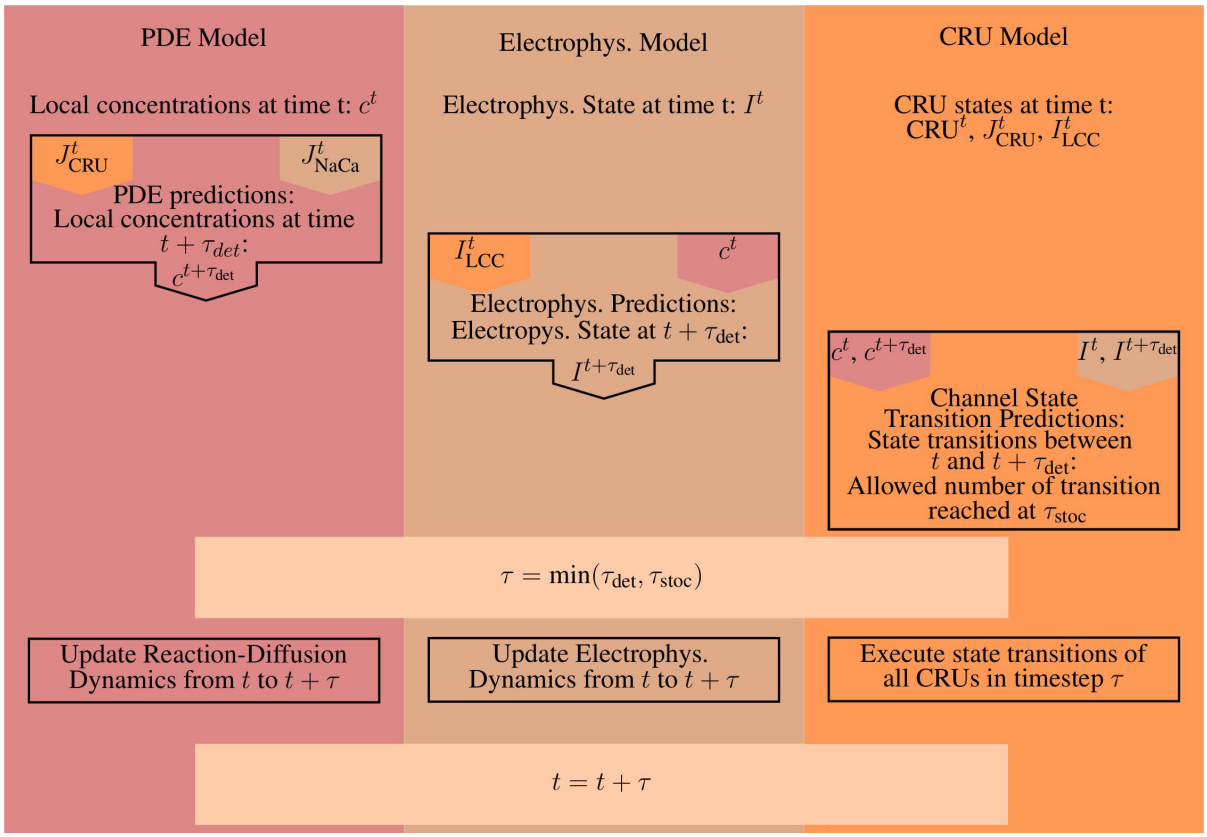

Figure 5: **A schematic illustrating the basic steps for a single iteration:** Orange marks all values produced and all work done by the CRU model. The work and results of the PDE model are marked in red, everything involved with the electrophysiology ODE model (Electrophys. in the diagram) is marked in brown. A superscript t marks the value of a given quantity at time t, while a superscript $t + \tau$ denotes the predicted value of that quantity at time $t + \tau$, for example the prediction step for the PDE model uses the flux values from the CRU and ODE model at time t. The CRU transition prediction step uses both the current values at time t and the predicted values at time $t + \tau$ from the PDE and ODE model.

3 Investigation of ryanodine receptor (RyR) Markov chain models

3.1 Introduction

First steps have been made to develop a computationally reasonable model of a CRU by Schendel (2010) [87, 95] which we want to include in a whole cell model. The properties of the ECC/CICR involve multiple length scales (tens of nanometers in the dyadic cleft to 100 µm cell size) and time scales (submillisecond for $[Ca^{2+}]$ changes in the dyadic cleft to tens of seconds for SR dynamics). Merging models of different types and scales causes challenges for the implementation and the parametrization, which we address in this chapter. The focus is the fitting of the CRU model [87] by investigating different Markov chain models for the RyRs. Afterwards, we aim to simulate our whole cell model, which is supposed to show physiological behaviour of a rabbit ventricular myocyte. We used mathematical multi-scale techniques, such as Green Function and quasistatic approximation, in combination with dynamic PDEs to simulate up to 5120 CRUs with spatially resolved $[Ca^{2+}]$ and stochastic state dynamics of all individual LCCs and RyRs. The results and discussion of this chapter were published by us in [26].

3.1.1 RyRs

RyRs are large, homotetrameric protein complexes located in the SR membrane and mediate the release of Ca^{2+} from the SR to the cytosol [112, 113]. The cytoplasmic assembly has dimensions of $\sim 28 \times 28 \times 12$ nm, the transmembrane assembly is much smaller [113]. In mammals, there are three RyR isoforms (RyR1 - 3) and RyR2 is the most abundant isoform in cardiac muscle [114]. In the cytoplasm, important regulators of RyRs are Mg^{2+}, ATP, and the Ca^{2+}-buffer calmodulin [112]. Ca^{2+} regulates RyRs at both sites in the cytoplasm and in the SR lumen [112], where it is buffered by calsequestrin [112]. There are many more regulators, for example FK506-binding proteins, protein kinase A, and junctin [112].

3.1.2 Aims

For many years, one main interest was to identify a robust mechanism which rapidly closes RyR to guarantee a stable jSR Ca^{2+} release [13]. Many different mechanisms have been proposed [13]: (1) The binding of Ca^{2+} to inactivation sites of the RyRs could increase their closing probability over time, and hence, inactivate the RyRs. (2) Spontaneous closing of individual RyRs reduces the Ca^{2+} flux locally and less RyRs are activated. This promotes the closure of other RyRs in the CRU and is known as "stochastic attrition". (3) The local Ca^{2+} signal could also be reduced by the local depletion of the jSR $[Ca^{2+}]$, which is known as induction decay. (4) Experiments showed that RyRs are less sensitive to the dyadic Ca^{2+} with decreased jSR $[Ca^{2+}]$ and the RyR open probability decreases during Ca^{2+} release. (5) RyRs themselves could promote closure of neighbouring RyRs by allosteric interactions. This mechanism is known as "coupled gating" and a potential mediator is the FK506-binding protein 12.6.
Experiments revealed that *in vitro* the RyR inactivation occurs at physiologically unrealistic high $[Ca^{2+}]$ and that the kinetics are too slow [13]. Furthermore, modelling approaches showed that RyR inactivation is not necessary for release termination, but

stochastic attrition and coupled gating alone are not sufficient [1, 3, 115, 68, 116]. In contrast, local jSR depletion in combination with coupled gating and jSR Ca^{2+} dependency is capable to account for release termination [3, 115], but there are uncertainties about the experimental evidence [13]. Hence, this issue is not fully resolved yet, even though local depletion of jSR Ca^{2+} is the simplest and most accepted mechanism [13]. We want to address this issue by our whole cell model and chose a compatible and physiologically realistic Markov chain model of the RyRs.

3.2 Modelling of RyRs

The module interactions and the time stepping scheme were presented in Chapter 2. We used the single CRU model by Schendel (2010) [87] and adapted it to fit into our whole cell model. Schendel (2010) [87] used the 4-state Markov chain model by Stern et al. (1999) [1] for the RyRs with one open state, a closed state, an inactivated state, and a resting state (see Figure 4A(i)). The kinetic scheme of the RyRs is controversially discussed and there are many different models. We tested the performance of the 4-state model developed by Stern et al. (1999) [1], a 2-state model (Figure 4A(ii)) developed by Cannell et al. (2013) [2], and another 2-state model (see Figure 4A(iii)) developed by Walker et al. (2014) [3]. For details about the RyR models see Chapter 2.4.

3.3 Simulation results

We used the parameters as specified in the Tables A.1 to A.5 (Column "Chapter 3"). We investigated three RyR models: Stern RyR model [1], Cannell RyR model [2], and Walker RyR model [3]. We tested whether they were able to reproduce physiological $[Ca^{2+}]_i$ transients. The RyR model which reproduced the most realistic transients in our whole cell model without deficiencies was characterized further and we investigated the restitution properties of this model. Finally, we ran the fully coupled simulation tool to represent almost one third of a cardiac myocyte.

3.3.1 RyR models

The three RyR Markov chain models all produce realistic APs (Figure 6) in simulations with a basic cycling length (BCL) of 350 ms. With the Stern RyR model [1] the peak $[Ca^{2+}]_i$ equalled 0.8 µM with a time-to-peak of 200 ms. With the Cannell model [2], dual peaks in $[Ca^{2+}]_i$ were observed with an early peak of $[Ca^{2+}]_i$ equals 0.6 µM with a time-to-peak of ∼10 ms, with the principal peak $[Ca^{2+}]_i$ transient of ∼0.8 µM and a time-to-peak of 100 ms. With the Walker model [3] the peak $[Ca^{2+}]_i$ was ∼1.0 µM and time-to-peak 130 ms.
The data in Figure 6 show that the $[Ca^{2+}]_i$ recorded in experiments via a fluorescent Ca^{2+} probe, such as Fluo-4 (denoted as $[Ca^{2+}]_i^{\text{exp}}$, as defined in Equation (25)), would smooth-out any early $[Ca^{2+}]_i$ peak, if this were a genuine experimental feature of cardiac myocyte CICR. In AP simulations with the 2-state RyR models, some local high Ca^{2+} transients at CRU-sites remained till into the diastolic period, associated with CRUs where some RyRs remained open. A similar phenomenon has been described in the setting of spontaneous Ca^{2+} sparks by Stern et al. [88], who used an RyR scheme similar to Walker [3] (a 2-state model, with modulation of the open probability by junctional RyR-lumenal $[Ca^{2+}]$ (c^i_{jsr})).

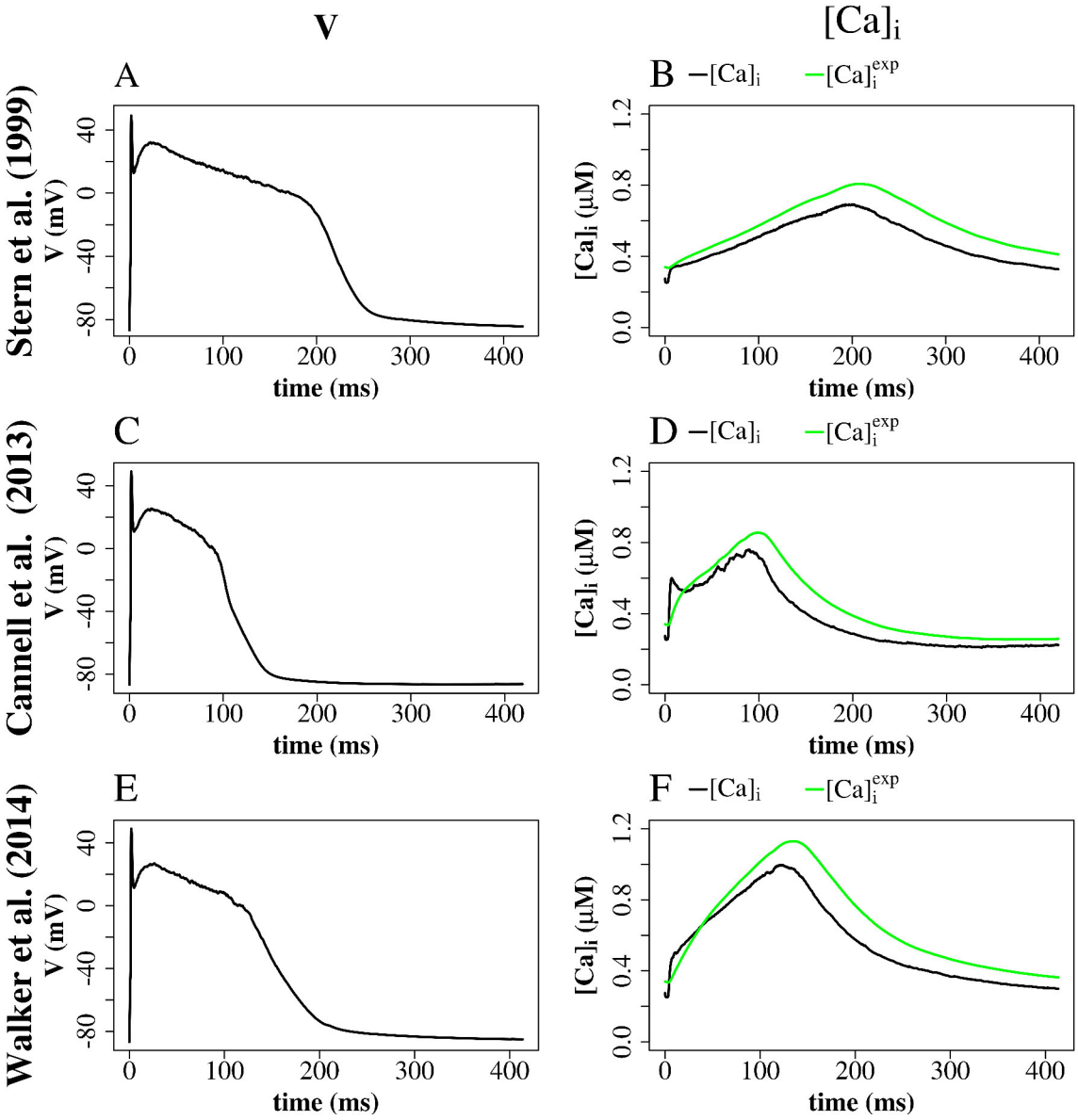

Figure 6: **Comparison of 4-state RyR model by Stern et al. (1999) [1] (top panels), 2-state RyR model by Cannell et al. (2013) [2] (middle panels), and 2-state RyR model by Walker et al. (2014) [3] (bottom panels): (A)** - Stern et al. (1999) [1] membrane potential. **(B)** - Stern et al. (1999) [1] average cytosolic $[Ca^{2+}]_i$ and $[Ca^{2+}]_i^{exp}$ (as defined in Equation (25)). **(C)** - Cannell et al. (2013) [2] membrane potential. **(D)** - Cannell et al. (2013) [2] average cytosolic $[Ca^{2+}]_i$ and $[Ca^{2+}]_i^{exp}$. **E** - Walker et al. (2014) [3] membrane potential. **F** - Walker et al. (2014) [3] average cytosolic $[Ca^{2+}]_i$ and $[Ca^{2+}]_i^{exp}$. Plots show the first AP from a simulation of a single z-disc.

When using the Stern model [1] there were slow kinetics of Ca^{2+} release and a low RyR maximum open percentage (2.7 %). Gain (the ratio of J_{rel} to J_{Ca}) was ∼4 during the first 50 ms of the AP and ∼3 for the remainder of the AP (BCL = 350 ms). With the Cannell model [2] many RyRs open and close (spark-like) within 20 ms of the start of the AP, and gain was high in this early phase of the AP (∼10) and moderate in the later AP (∼6) and there was a corresponding fast rise in the $[Ca^{2+}]_i$ with an early peak at ∼10 ms, followed by a reduction of the $[Ca^{2+}]_i$ and a second $[Ca^{2+}]_i$ rise and fall through the AP. With the Walker model [3] gain was ∼6 in the early AP, then ∼2 in the remainder of the AP, and there was a relatively high RyR maximum open percentage (32 %). The Walker [3] and Cannell [2] 2-state RyR schemes had markedly faster (and more physiological) kinetics of Ca^{2+} release than the Stern 4-state scheme [1]. With the Walker RyR scheme [3] our model displayed expected restitution properties with shorter AP duration at 90% repolarization (APD_{90}) and a corresponding longer diastolic interval (DI) (Figure 7D) and the $[Ca^{2+}]_i$ transient with shorter BCL (Figure 7A-C).

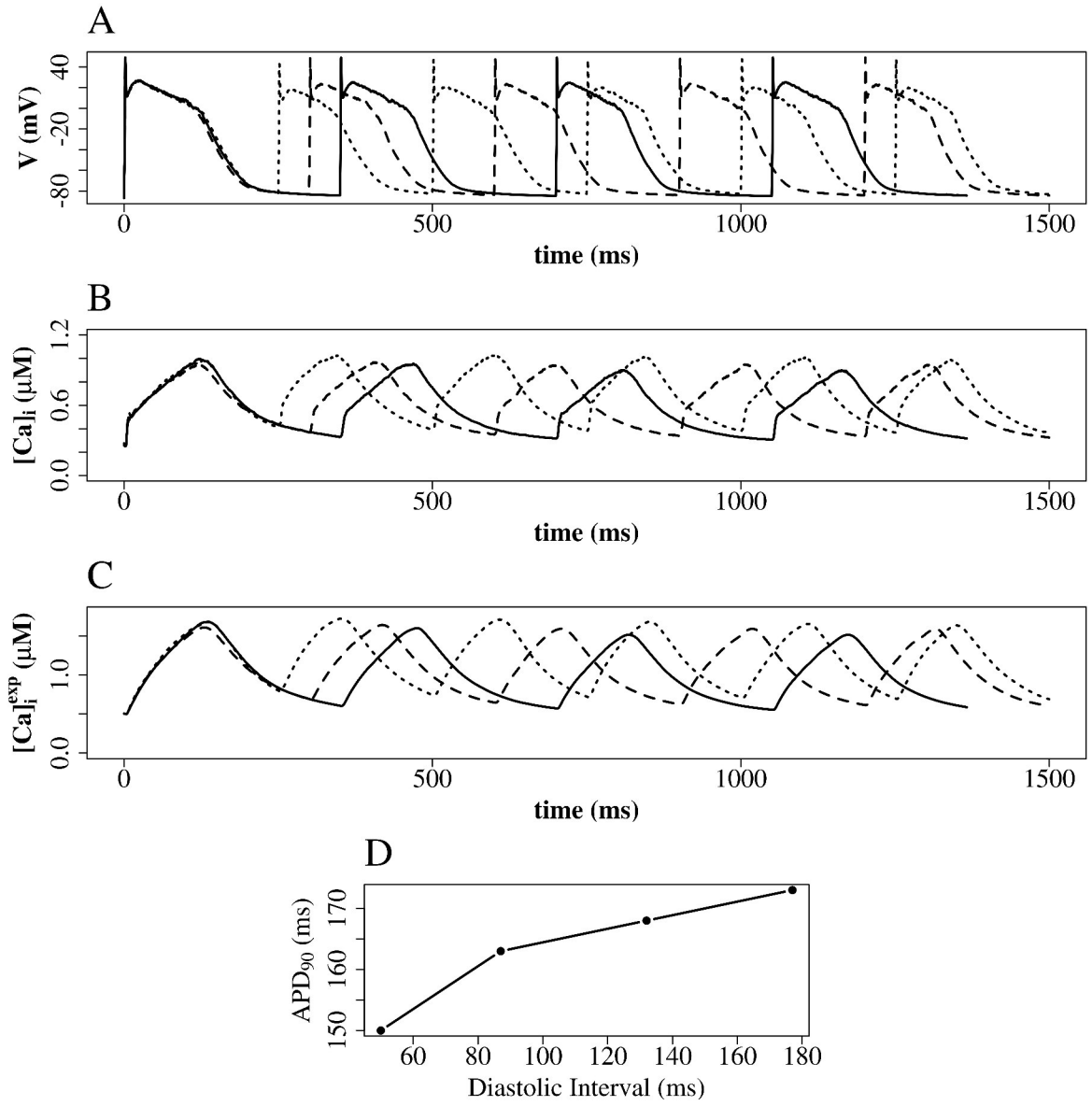

Figure 7: **Restitution properties with the Walker RyR model [3]: (A)** - Membrane potential. **(B)** - Average cytosolic $[Ca^{2+}]_i$. **(C)** - Average cytosolic $[Ca^{2+}]_i^{\text{exp}}$ as defined in Eq. (25). Solid line: BCL = 350 ms; dashed line: BCL = 300 ms; dotted line: BCL = 250 ms. At cycle length 350 ms the diastolic interval (DI) was 177 ms. At cycle length 300 ms the DI was 132 ms. At cycle length 225 ms the DI was 87 ms. **(D)** - Constant BCL Restitution Curve [117] using AP duration at 90 % repolarisation (APD_{90}). For clarity, the AP with the shortest DI in **D** is not shown in **A**, **B**, and **C**. These simulations have been carried out with a single z-disc.

3.3.2 Whole cell model

Our motivation was to be able to take into account individual stochastic channel state dynamics in each CRU and the concentration profile within CRUs while executing the simulation of (P)DEs for other state variables. Figure 8 shows such a concentration profile inside the dyadic cleft calculated with Equation (21) for a typical RyR current. Gradients are substantial such that distant RyRs and LCCs experience much smaller Ca^{2+} concentrations and Ca^{2+}-dependent transition rates than channels close to an open one.

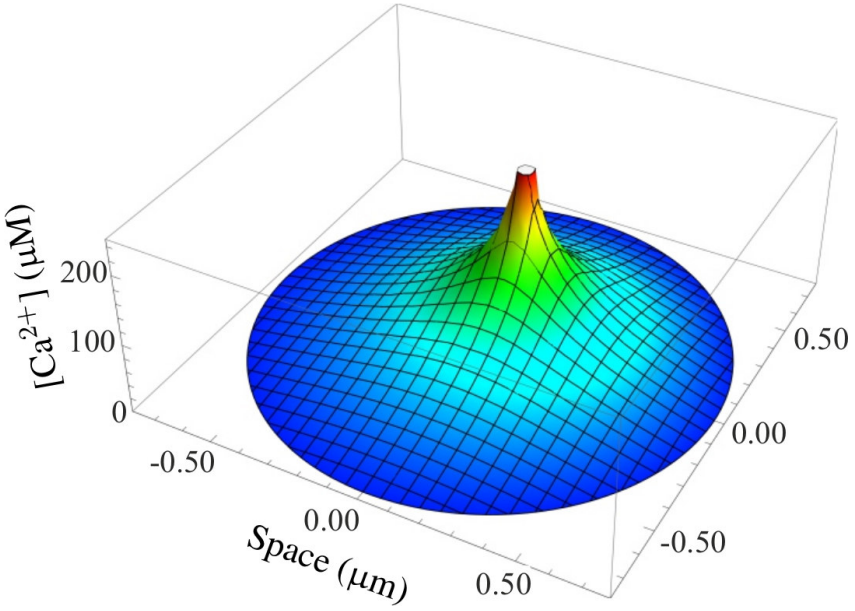

Figure 8: **Simulation of a typical Ca^{2+} gradient in a CRU:** The stationary dyadic $[Ca^{2+}]$ profile of a single open RyR is shown.

We simulated 16 z-discs, each with 320 CRUs, and the Ca^{2+} dynamics for this subcellular region (∼30 % of the cardiac myocyte) were coupled to the whole cell electrophysiology ODE model. It took 64.2 hours to solve a single AP on 848 Intel Xeon E5-2650 v2 2.60GHz CPUs. The $[Ca^{2+}]_i$ profile 70.0 ms after stimulus at a single z-disc is shown in Figure 9A and the corresponding nSR free $[Ca^{2+}]$ is shown in Figure 9B. The $[Ca^{2+}]_i$ of inactive CRUs remained low (Figure 9A, in blue) and in the center of active CRUs with many open RyRs locally high $[Ca^{2+}]_i$ of ∼6.0 μM were reached (in red). The Ca^{2+} of the nSR was depleted in the vicinity of CRUs (Figure 9B, in blue). The local Ca^{2+} dynamics are shown in Figure 10A as isosurfaces. The red isosurface indicated a $[Ca^{2+}]_i$ of 2.4 μM visible inside the CRUs. The nSR free $[Ca^{2+}]$ is visualized in Figure 10B with a yellow isoface indicating a nSR free $[Ca^{2+}]$ of 430 μM. Figure 11 shows the membrane potential (A), various ionic currents (B and C), the $[Ca^{2+}]_i$, and $[Ca^{2+}]_i^{\text{exp}}$ transient (D), Ca^{2+} fluxes (E), and buffer concentrations (F) using the RyR Markov chain model by Walker et al. (2014) [3].

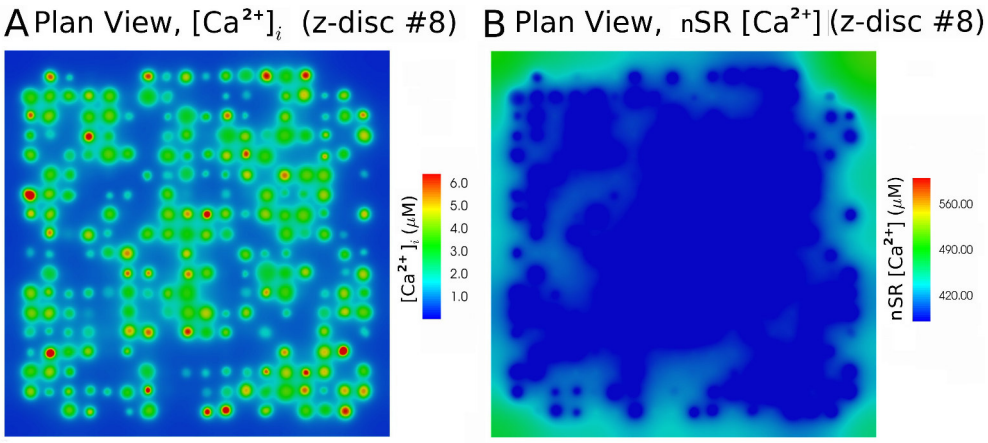

Figure 9: **Free $[Ca^{2+}]_i$ and nSR free $[Ca^{2+}]$ at 70.0 ms after activation, using the Walker RyR model [3]: (A)** - cytosolic $[Ca^{2+}]_i$. **(B)** - nSR free $[Ca^{2+}]$ for the 8th z-disc numbered from the bottom in Figure 10. The concentration is colour-coded according to the color scale shown. There are 320 CRU per z-disc, with an average of 50 RyRs and 12.5 LCCs per CRU.

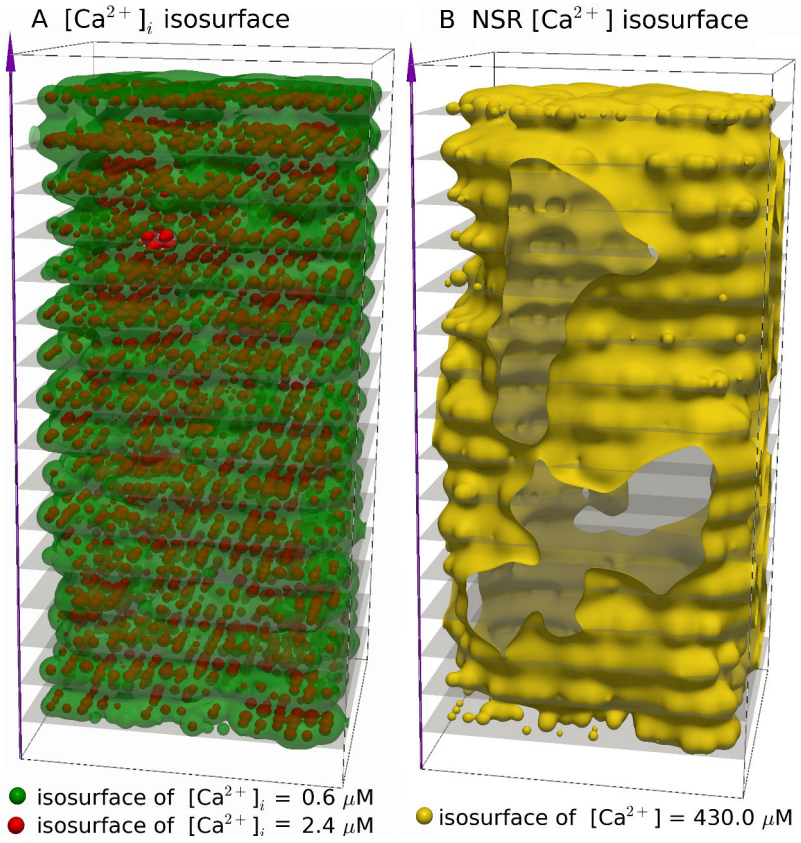

Figure 10: **Three dimensional visualisation of spatially resolved $[Ca^{2+}]$ at 70.0 ms after activation, using the Walker RyR model [3]: (A)** - Isosurfaces show $[Ca^{2+}]_i$ in green for $[Ca^{2+}]_i = 0.6$ μM and red for $[Ca^{2+}]_i = 2.4$ μM. **(B)** - The yellow isosurface shows nSR free $[Ca^{2+}] = 430$ μM. There are 320 CRU per z-disc, amounting to 5160 CRUs in total, with an average of 50 RyRs and 12.5 LCCs per CRU.

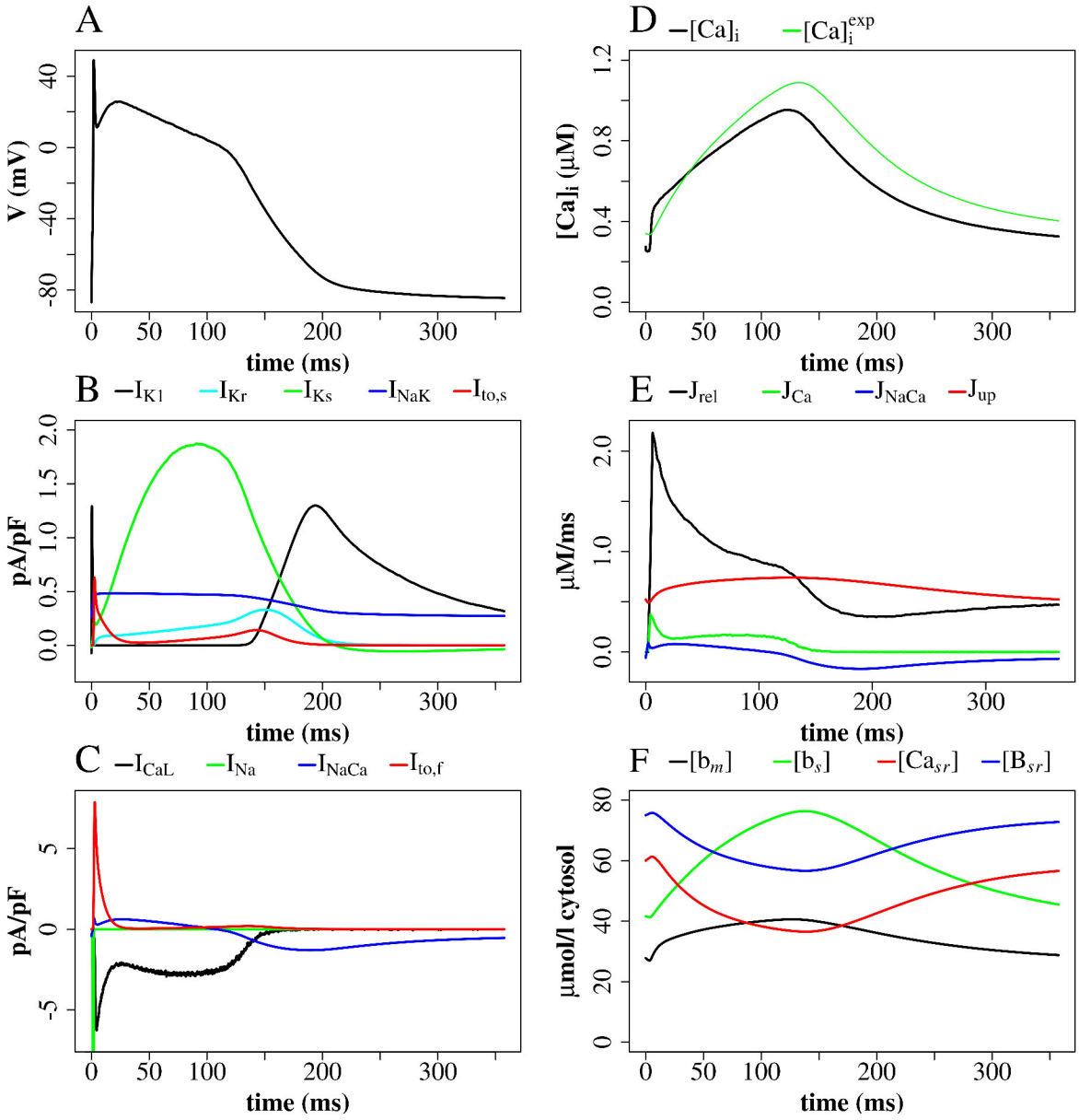

Figure 11: **Membrane potential, ionic currents, and concentrations after a stimulus of 40 mV for 1 ms: (A)** - Membrane potential. **(B)** - Currents I_{K1}, I_{Kr}, I_{Ks}, I_{NaK}, and $I_{to,s}$. **(C)** - LCC current (I_{CaL}), NCX current (I_{NaCa}), $I_{to,f}$, and I_{Na} (truncated). **(D)** - Average cytosolic $[Ca^{2+}]_i$. **(E)** - Ca^{2+} -fluxes: J_{rel}, J_{Ca}, J_{NaCa}, J_{up}. **(F)** - Buffer-bound $[Ca^{2+}]$ ($[b_m]$, $[b_s]$, $[B_{sr}]$,) and nSR free $[Ca^{2+}]$ ($[Ca_{sr}]$) are plotted. Note: $[b_m]$ and $[b_s]$ are conventional concentrations in units of µM whereas $[Ca_{sr}]$ and $[B_{sr}]$ are expressed for simplicity in units of $\mu M \nu_{sr}/\nu_{cyt}$ (µmol/l cytosol). Plots show the first AP of a simulation with 16 z-discs.

3.4 RyR model choice and multi-scale simulation

We explored the use of three RyR Markov chain models: the 4-state model of Stern et al. (1999) [1], the 2-state induction decay model of Cannell et al. (2013) [2], and the 2-state model of Walker et al. (2014) [3]. The Walker model is identical to the Cannell model except with the addition of modulation of the RyR open probability by junctional RyR-lumenal $[Ca^{2+}]$ (c^i_{jsr}). With the Stern RyR model the $[Ca^{2+}]_i$ peaked at 0.8 μM with time-to-peak of 200 ms. With the Cannell model, dual peaks in $[Ca^{2+}]_i$ were observed with an early peak of $[Ca^{2+}]_i$ equals 0.6 μM at time-to-peak ∼10 ms, with the principal peak $[Ca^{2+}]_i$ transient of ∼0.8 μM and time-to-peak 100 ms. With the Walker model the peak $[Ca^{2+}]_i$ was ∼1.0 μM and time-to-peak 130 ms. The time-to-peak of $[Ca^{2+}]_i$ for both the 2-state models is comparable to that reported for the rabbit by Weber et al. (2002) [118] of 81 ms. The early $[Ca^{2+}]_i$ local maximum with the Cannell model may be explained from the origins of the Cannell model [2]. The model was fitted to experimental data from Ca^{2+} sparks and has never been previously used in a model of prolonged CICR resulting from an AP. Indeed the authors of this model state that the model equations are not designed to capture behaviour at resting $[Ca^{2+}]_i$ with fully loaded SR. The RyR dynamics of this model with its current parameters are therefore reproducing spark-like behaviour in an AP. We had to introduce strong buffering (buffer factor β) inside the dyadic cleft and jSR-depletion in order to reach closing rates sufficiently fast for termination of release at the end of an AP. However, this proof of concept investigation does not provide evidence that induction decay alone is an insufficient mechanism to cause the termination of CICR in an AP. Rather, the model provides a platform for investigating AP CICR. Careful, experimentally led tuning of the 2-state model parameters alongside Ca^{2+}-buffering parameters and the jSR refill flux will allow assessment of the feasibility of induction decay as the sole CICR termination mechanism in an AP. A second explanation for the early local maximum in the $[Ca^{2+}]_i$ is that in our model we do not explicitly represent the $[Ca^{2+}]_i$ uptake and release by the mitochondria. Although, the mitochondrial $[Ca^{2+}]_i$ uptake and release is controversial on such fast time scales [119], there is evidence that fast early mitochondrial $[Ca^{2+}]_i$ uptake can act like a fast stationary buffer [120]. Moreover, the inhibition of fast uptake through a specific inhibitor of the mitochondrial Ca^{2+} uniporter (MCU) can result in an early local maximum of the $[Ca^{2+}]_i$ transient [120].

The simulation with 16 z-discs and the Walker RyR model [3] shows that we can reproduce the whole sequence of Ca^{2+} transients from the initial concentration profile in the dyadic cleft via sparks to the whole cell transient. The cytoplasmic $[Ca^{2+}]$ is rather heterogeneous due to randomness of release events as well as variations in CRU size. The concentration of 0.6 μM is reached in almost the whole volume, but a concentration of 2.4 μM is only reached in the proximity of the z-discs.

This proof of concept study demonstrates a new multi-scale model of CICR linking three spatial scales: (1) detailed molecular stochastic modelling of the CRU at a continuous spatial scale, (2) a whole cell ODE electrophysiology model, which describes the potassium channels, the voltage gated sodium channels, the sodium-potassium pump, and integrates all membrane fluxes to derive the total membrane current and voltage, and (3) a PDE finite element method Ca^{2+} diffusion model representing cytoplasmic and nSR free Ca^{2+} diffusion between CRUs and between z-discs. One rationale for this approach is that it allows the removal of the artificial compartment for the submembrane space, and hence, provides a more quantitative modelling of diffusion processes and gradients.

Taking gradients in the dyadic cleft into account in a simulation with thousands of CRUs would be impossible without the use of the stationary Green function. An estimate of the advantage of the quasistatic approximation with respect to computational speed can be obtained from estimating the number of operations per CRU. Our approach requires to solve a linear system of equations whenever channels open or close, or the boundary condition or the jSR concentration have changed significantly, which means $(N_{\mathrm{RyR}} + N_{\mathrm{LCC}})^2$ operations each. Simulating the concentrations inside the cleft would require about 1000 grid points and a time step in the microsecond range (see [121]). Consequently, the simulation would be about few hundred times slower without the use of the stationary Green function. Applying the dynamic Green function would entail similar computational efforts, since it converges extremely slowly [122].

To our knowledge, our model is the only whole cell AP model which includes CRUs clustered around the z-discs (a proxy for explicit t-tubules) and spatial resolution of intra-CRU $[Ca^{2+}]$ with realistic steep $[Ca^{2+}]$ gradients. Other approaches include the multi-scale model of Restrepo et al. (2009) [84] which simulates ∼20,000 CRUs with Markov chain models for individual LCCs and RyRs in a three-dimensional grid interacting with a membrane voltage ODE-model [6]. This was developed further by Nivala et al. (2012) [17] and was modified to a bi-domain approach with finite elements belonging to cytoplasm or SR. A related model of Williams et al. (2011) [85] incorporates energetic coupling of the RyRs, and non-junctional RyRs, but is used only for the analysis of the diastolic RyR dynamics without an ODE electrophysiology model. Walker et al. (2014) [3], based on Williams et al. (2011) [85], developed a finite volume model of a single CRU which includes modelling of intra-CRU Ca^{2+} concentration differences, diffusion of Ca^{2+} and mobile buffers, t-tubules, Markov chain models for the channels, and excitation contraction coupling gain. Cannell et al. (2013) [2] investigated spark dynamics and termination using a 2-state RyR model with modelling of intra-CRU Ca^{2+} concentration differences, but until our current study the Cannell model [2] had not been coupled to a whole cell geometry or to an AP model. Torres et al. (2014) [123] modelled a modified local control mechanism to simulate confocal image data and to explore the relationship between Ca^{2+} transients and the activation of non-junctional RyR clusters of myocytes with sparse t-tubule systems. A finite element model has been implemented by Hatano et al. (2011) [80] which incorporates subcellular structures including the t-tubule system, SR, myofibrils, and mitochondria, where electrophysiology and local Ca^{2+} dynamics are coupled to a local myofibril contraction model to simulate local and global contraction. They model the spatial detail of CICR release and local contraction for three myofibrils of one sarcomere length but do not model the $[Ca^{2+}]$ of the dyadic cleft in spatially resolved detail. They used this model to investigate the importance of the t-tubule system for the maintenance of the ECC [82]. A multi-scale model considering physiologically detailed description of the stochastic Ca^{2+} channels in a network of ∼20,000 CRUs was developed by Restrepo and colleagues [83, 84, 20] in which each CRU contains five subvolumes. However, the CRU is considered as a common-pool for Ca^{2+} gradients [23]. Sato et al. (2016) [92] improved this model, for example by adding Ca^{2+} diffusion, and they investigated how the spark duration depends on the number of RyRs per CRU. Rajagopol et al. (2015) [93] modelled the spatial distribution of RyR clusters, myofibrils, and mitochondria based on three-dimensional electron microscopy data.

3.5 Conclusions

The 2-state RyR Markov chain models by Walker et al. (2014) [3] and by Cannell et al. (2013) [2] showed more realistic physiological kinetics in our whole cell model than the model by Stern et al. (1999) [1] did. The model by Walker [3] includes the jSR Ca^{2+} dependency mechanism and is therefore favoured by us. It can be easily switched to the Cannell RyR model [2] by turning of the jSR Ca^{2+} dependency mechanism. The Walker model [3] showed expected restitution properties.

We showed on a proof-of-concept level that multi-scale modelling of cardiac myocyte ECC from subdyadic scales to many z-discs using full PDEs is possible. We demonstrated that the model produces realistic physiology on these scales and has the potential to provide new insight into subcellular mechanisms and structures. Maybe the most severe limitation of this modelling approach is the requirement for high performance computing to run it. Some improvement of simulation efficiency is possible by more specifically tailored numerical methods, however, the requirement for high performance computing remains. The use of the Green function inside the dyadic cleft requires linearity of the reaction diffusion equations. That excludes non-linear buffering terms and allows for linear buffering only. Another issue are CRUs where some RyRs remained open in diastole using the 2-state Markov chain models. A similar phenomenon has been described in the setting of spontaneous Ca^{2+}-sparks by Stern et al. (2013) [88], who used an RyR scheme similar to Walker et al. (2014) [3]. The Walker model is a 2-state model, with modulation of the open probability by junctional RyR-lumenal $[Ca^{2+}]$ (c^j_{jsr}). Moreover, all RyRs and LCCs are in the same closed state at the beginning of a simulation and we used a too high buffer factor of 6.

The discrepancies between our simulations and the ODE-Mahajan model with respect to NCX currents illustrate the value of spatially resolved modelling in exploring detailed properties of Ca^{2+} dynamics. Using the same NCX model as Mahajan et al. (2008) [6], we were not yet able to reproduce the same time course of the total NCX current. In both models the current has the same general profile, with a short period in reverse mode (positive current) in the first phase of an AP, followed by forward mode (negative current) during the membrane potential plateau and decline. However, in our approach the I_{NaCa} current turns negative much later during the plateau than in the ODE model. NCX depends on the $[Ca^{2+}]$ in submembrane space in the ODE model and on the cytoplasmic concentration c in our simulations, including the regions with high c-values at and close to CRUs. The main reason for the differences is that the submembrane $[Ca^{2+}]$ in the ODE model exhibits a sharp rise and decline while the average cytoplasmic concentration shows slower dynamics. We have experimented with localising the NCX molecule density in proximity to the CRUs to reflect the observed higher abundance of NCX near the CRU ([124], [125], [126], [127]). However, this has not yet fully resolved the discrepancies with respect to the ODE results. We expect to gain detailed insights into the factors shaping the NCX current by investigating of these problems in Chapter 5.

Some of the limitations of our model arise from its early state of development and will be removed with inclusion of more detail and more parameter fitting. We used modular programming as far as possible to ease the exploration of a variety of ion channel models and other species specific membrane potential dynamics.

4 Parametrization of the sarcoplasmic reticulum (SR)

4.1 Introduction

We demonstrated that our multi-scale model of a cardiac mocyte produces physiologically realistic results with some limitations, which we mentioned in Chapter 3. We addressed these limitations by parameter fitting of the channels and buffers. We increased the average number of the RyRs per CRUs from 50 to 63 [100] and set a minimum of 10 RyRs per CRU. Each channel's state was chosen randomly according to the steady state distribution for the initial values. We also changed the total concentration of some buffers (see Table A.1, Column "Chapter 4") and set the buffer factor β to 1. LCC and RyR parameters, the SR volume/cell volume ratio, and the external [Ca^{2+}] have been changed (see Table A.4, Column "Chapter 4" and Table A.3, Column "Chapter 4 & 5 & 6"). Previously, we have assigned a single value to the f_{NCX}^{surf} for each surface element. Now we assign to each surface element the same f_{NCX} value corresponding to its volume finite element (for details see Chapter 5.2.2) and we changed the values for the f_{NCX}^{high} and f_{NCX}^{low} (see Table A.2). In the subsequent simulations and analyses we used the Walker RyR model [3] and one quarter of a z-disc with 77 CRUs was simulated to reduce running time (see Table A.3, Column "Chapter 4 & 5 & 6", and Table A.4, Column "Chapter 4 & 5 & 6"). These parameter changes marginally improved the simulated physiology and facilitate further analyses. In this chapter the aim is to investigate the parameters of the SR and its components to produce improved physiological behaviour of a cardiac myocyte.

4.1.1 Sarcoplasmic reticulum

The sarcoplasmic reticulum (SR) is an intracellular membrane network with tubules and cisternae [128] occupying < 10 % of the cell volume in cardiac myocytes [129]. The SR serves as a Ca^{2+} store [130] and provides the majority of the Ca^{2+} for the systolic transient of an AP [131], which is released by the RyRs. The amount of free Ca^{2+} depends on the SR Ca^{2+} load and defines the extent of muscle contraction and force development [130]. The SR has received much attention because of its crucial role in Ca^{2+} homoeostasis, restoration of [Ca^{2+}] and relaxation, contraction and response to agonist stimulation, and modulating membrane excitability in health and disease [130].
The SR [Ca^{2+}] is determined by the activity of the SR calcium ATPase (SERCA), the binding dynamics to the main SR Ca^{2+}-buffer calsequestrin, the refill flux of the Ca^{2+} from the nSR to the jSR and the opening behaviour of the RyRs. Each of these components were investigated in this chapter except for the RyRs, which were analysed in Chapter 3.

4.1.2 SERCA

The sarcoplasmic/endoplasmatic reticulum calcium ATPase (SERCA) is a bi-directional pump of the SR membrane [132]. There are three paralogs of SERCA (SERCA1 - 3) and ten post-translational isoforms [133]. SERCA2a is the predominant isoform in the adult mammalian heart and the most abundant protein of the SR membrane [130]. SERCA transports Ca^{2+} from the cytosol against the concentration gradient to the lumen of the SR using ATP as energy source [131]. The stoichiometry is two Ca^{2+} ions per one hydrolysed ATP [132]. After the motor protein myosin, SERCA is the second largest consumer of ATP, and therefore, its activity is affected by the mitochondrial ATP supply [130].

SERCA also transports two H^+ ions per cycle and is therefore pH-dependent [132]. The Ca^{2+} is removed from the cytosol by SERCA, NCX, and plasma membrane Ca^{2+}-ATPase (PMCA) [134]. The latter, however, contributes only an insignificantly small part to this removal [134]. Ca^{2+} removal from the cytosol enables muscle relaxation. Thus, SERCA regulates the cytosolic [Ca^{2+}], SR Ca^{2+} load, and the rate of contraction and relaxation of the cardiac myocyte [130]. Its expression and activity are critical for SR Ca^{2+} uptake functions and cardiac dysfunctions [130]. Studies have shown that the SERCA activity is reduced in failing hearts [135, 136, 137]. However, the importance of SERCA varies between species. Species with a high resting heart rate of ∼300 bpm - 600 bpm, such as mice and rats, have shorter APs than species with a short resting heart of ∼60 bpm - 350 bpm rate, such as guinea-pigs and humans [40]. In species with short APs, there is a greater release of Ca^{2+} from the intracellular storage and relatively less Ca^{2+} influx via the sarcolemma. Therefore, the re-uptake via SERCA is more important in species with short APs to compensate for the greater Ca^{2+} release through the RyRs [11, 66]. Transgenic animal models with short APs overexpressing SERCA2a or SERCA1a show an increased SR Ca^{2+} transport, increased rates of cardiac contraction and relaxation [130, 131]. These changes are well tolerated [130]. However, a decrease in SERCA expression by gene knockout of both alleles in mice is lethal [130]. Heterozygous mice maintain Ca^{2+} homoeostasis, but are more prone to heart failure under stress conditions compared to wild type mice [130].
The two main regulators of SERCA are phospholamban (PLB) and sarcolipin (SLN), both low molecular weight proteins [130]. Phospholamban is an endogenous inhibitor of SERCA during β-adrenergic receptor stimulation [131]. Hormones, such as thyroid hormone (T4) in hyperthyroidism, can up-regulate the SERCA2a expression and increase the velocity of Ca^{2+} uptake [130].
Direct measurements of the SERCA flux *in vivo* are not possible and it can only be indirectly measured, for example, through measurements of SR Ca^{2+} content, the total amount of Ca^{2+} increase and the sarcolemmal NCX flux [132]. Experimental data of SERCA activity include possible errors and experimental variation [132]. Hence, the SERCA function is always the result of derivation and assumption based calculations. Modelling SERCA is therefore a useful tool to close gaps in knowledge of SERCA mechanisms. Many models of SERCA have been developed ranging from simple fundamental models to complex models which include Ca^{2+}-buffering, reversibility, and regulation [132].

4.1.3 Calsequestrin and refill flux

Calsequestrin is the most abundant Ca^{2+}-binding protein in the cardiac myocyte [138]. There are two isoforms, one for the fast-twitch skeletal muscle and one for the cardiac and slow-twitch skeletal muscle [138]. Calsequestrin is highly acidic, has a high-capacity, but low-affinity for Ca^{2+}-binding with almost 50 binding sites and a mass of ∼40 kDa [138]. Calsequestrin undergoes conformational changes when it binds to Ca^{2+} [139] and it interacts either directly with RyRs [140] or via triadin1 and junctin [141]. It is localized in the jSR and is not present in the nSR [142]. Besides its function as Ca^{2+}-buffer, it also regulates RyR activity [138]. The Ca^{2+} depletion of the jSR via the RyRs is compensated by the Ca^{2+} flux from the nSR known as refill flux.

4.1.4 Aims

The complex structure and its location inside the cell make direct measurements of the Ca^{2+} dynamics of the SR difficult. Many attempts have been made to measure SR Ca^{2+} dynamics, but these have been dependent on complicated assumptions and derivations based on Ca^{2+}-buffering capacity, SR volume, SERCA activity, and RyR dynamics [41]. Even direct measurements of the SR free $[Ca^{2+}]$ with fluorescent Ca^{2+} indicators are not sufficiently accurate as calibration was not achieved in experiments of Kasai et al. (2004) [41]. The SR release depends on the buffering capacity (calsequestrin) and on the SR content, which in itself is only marginally dependent on the SERCA activity [143, 131]. Spontaneous spark frequency depends strongly on the SR free $[Ca^{2+}]$, which causes instability in the release flux termination [144, 145]. The refilling time of Ca^{2+} from the nSR to the jSR is not crucial for Ca^{2+} alternans at high pacing rates [146]. Such dependencies have been thoroughly investigated by experimental and modelling studies, but the values of Ca^{2+} concentrations, buffer capacities, and fluxes have only been extrapolated, not directly determined. As a result, we have to find appropriate values for the parameters describing the Ca^{2+}-binding and flux kinetics.
The aim of this investigation is to analyse and improve the model of the SR to achieve physiological behaviour of the Ca^{2+} dynamics, which form the basis for model improvement and model extension. The investigation has been carried out changing key parameters of the SR model. The sensitivity of the system, and thereby the importance of the individual parameters, varies. We focus on key output values including APD_{90}, the amplitude of the Ca^{2+} transient, the nSR free $[Ca^{2+}]$ and its depletion, and the RyR flux to replicate known Ca^{2+} dynamics. We aim for an APD_{90} of $\sim$185 ms [147, 148], a peak $[Ca^{2+}]_i$ of $\sim$1.1 µM [118, 6, 11, 149], but a high depletion of nSR free Ca^{2+} of $\sim$50 % [150] or at least in the range of 20 % - 60 % [151], a nSR free $[Ca^{2+}]$ of $\sim$80 µmol/l cytosol, a calsequestrin concentration $[B_{sr}]$ of < 2.9 mM SR [145], and the delay parameter τ_d of $\sim$4 ms [6]. All these target values are listed in Table A.6.

4.2 Modelling of SR

The implementation of the SR, the calculation of the nSR free $[Ca^{2+}]$ and the jSR Ca^{2+} dynamics are described in the Chapters 2.2 and 2.4.5.

4.2.1 SERCA

In the first generation of cardiac myocyte models SERCA was treated as a simple unidirectional pump model, and thus, it was modelled with first-order enzyme kinetics through the Michaelis-Menten equation, which is equivalent to a Hill kinetic with a Hill coefficient of 1 [58]. Later a Hill coefficient of 2 was used according to experiments [60, 64] (see Equation 7).
The use of a simple uniporter model of SERCA is common and often appropriate because thermodynamic limits are not achieved during normal cycling operation and the transport of H^+ can be neglected [132]. However, this simple model shows a Ca^{2+} transport into SR, if the $[Ca^{2+}]_i$ is very low contradicting experimental results [152, 145, 153]. A second model considers not only the Ca^{2+} of the cytosol, but also introduces the SR free $[Ca^{2+}]$ (S) as feedback inhibitor [154]. If S is too high, the Ca^{2+} uptake is reduced. Sneyd

et al. (2003) [154] used a logistic equation for SERCA:

$$J_{\text{pump}} = \frac{V_P^{\max} c}{K_P + c} \frac{1}{S}. \tag{43}$$

In this model, the pump flux is zero only under non-physiological conditions [132]. More complex models have been developed in which buffering of Ca^{2+} and reversibility accounting for separate forward and reverse modes are included (for example [132, 155]). Such models may be useful to investigate conditions where the ECC process is disturbed. However, we focus on the simulation and physiology of a healthy cardiac myocyte.

4.2.2 Calsequestrin and refill flux

In our whole cell model calsequestrin is the only SR Ca^{2+}-buffer. The binding of a buffer B to Ca^{2+} can be described by the following equation [60]:

$$B + Ca^{2+} \rightleftharpoons BCa^{2+}. \tag{44}$$

A differential equation based on such reaction kinetics is solved to model calsequestrin B_{sr} (Equation (10)).
The jSR $[Ca^{2+}]$ decreases during the systole as a result of Ca^{2+} release via the RyRs. The individual junctional sarcoplasmic reticulae are refilled by the Ca^{2+} refill flux, J_{refill} (Equation (11)), from their adjacent nSR.

4.3 Parametrization results

First, we investigated how two SERCA models and their parameters affect key output variables. After selecting appropriate parameter values, we changed the localization of calsequestrin in our model and we investigated how the delay parameter of the refilling flux influences the key output variables.

4.3.1 SERCA

The uptake flux by SERCA is defined by the strength of uptake ($V_P^{\max}$) and the uptake threshold (K_P) (see Equation (43)). The $[Ca^{2+}]_i$ was calculated at each time step. We varied $V_P^{\max}$ from 0.1 µM/ms - 1.1 µM/ms in six simulations with a BCL of 350 ms. For each $V_P^{\max}$ value, a simulation with 10 APs has been run and we calculated the average of the key output variables of the last three APs. The following key output variables were used to investigate the effect of the parameter change: (1) APD_{90}, (2) minimum (resting) and maximum (peak) $[Ca^{2+}]_i$, (3) maximum RyR flux, (4) minimum and maximum nSR free $[Ca^{2+}]$, and (5) the depletion of the nSR free $[Ca^{2+}]$.
Figure 12 shows these key output variables with K_P set to 0.4 µM. APD_{90} decreased with increasing $V_P^{\max}$ (Figure 12A). Since APD_{90} was 420.6 ms with $V_P^{\max}$ set to 0.1 µM/ms, it was longer than the cycling length of 350 ms. APD_{90} decreased slowly with $V_P^{\max}$ values higher than 0.5 µM/ms. The resting and the peak $[Ca^{2+}]_i$ were marginally affected by the change of $V_P^{\max}$ (Figure 12B, in green and red, respectively,). The peak $[Ca^{2+}]_i$ was ∼2 µM and decreased marginally with increasing $V_P^{\max}$. The minimum nSR free $[Ca^{2+}]$ increased from 55.8 µmol/l cytosol to 109.9 µmol/l cytosol (Figure 12C, in green) and the maximum nSR free $[Ca^{2+}]$ increased from 60.1 µM/l cyotsol to 118.6 µM/l cyotsol (Figure 12C, in red). Figure 12D shows that the maximum depletion of nSR free

$[Ca^{2+}]$ was 11.5 % with a V_P^{max} of 0.5 µM/ms. The maximum RyR flux increased from 0.38 µM/ms to a maximal value of 3.14 µM/ms (Figure 12E). Despite the impression given by Figure 12E, RyR flux did not saturate at V_P^{max} of 0.9 µM/m, but increased further with $V_P^{max} > 1.1$ µM/m and reached a physiologically unrealistic high RyR flux (data therefore not shown).
The same simulations and analyses were executed for K_P set to 0.1 µM/ms, 0.3 µM and 0.6 µM (data not shown). The overall behaviour of the key output variables was similar to the results of Figure 12 in that with increasing V_P^{max} APD_{90} and RyR flux decreased, the peak $[Ca^{2+}]_i$ first decreased and with V_P^{max} greater than 0.5 µM/ms increased, and nSR free $[Ca^{2+}]$ increased with increasing V_P^{max}.

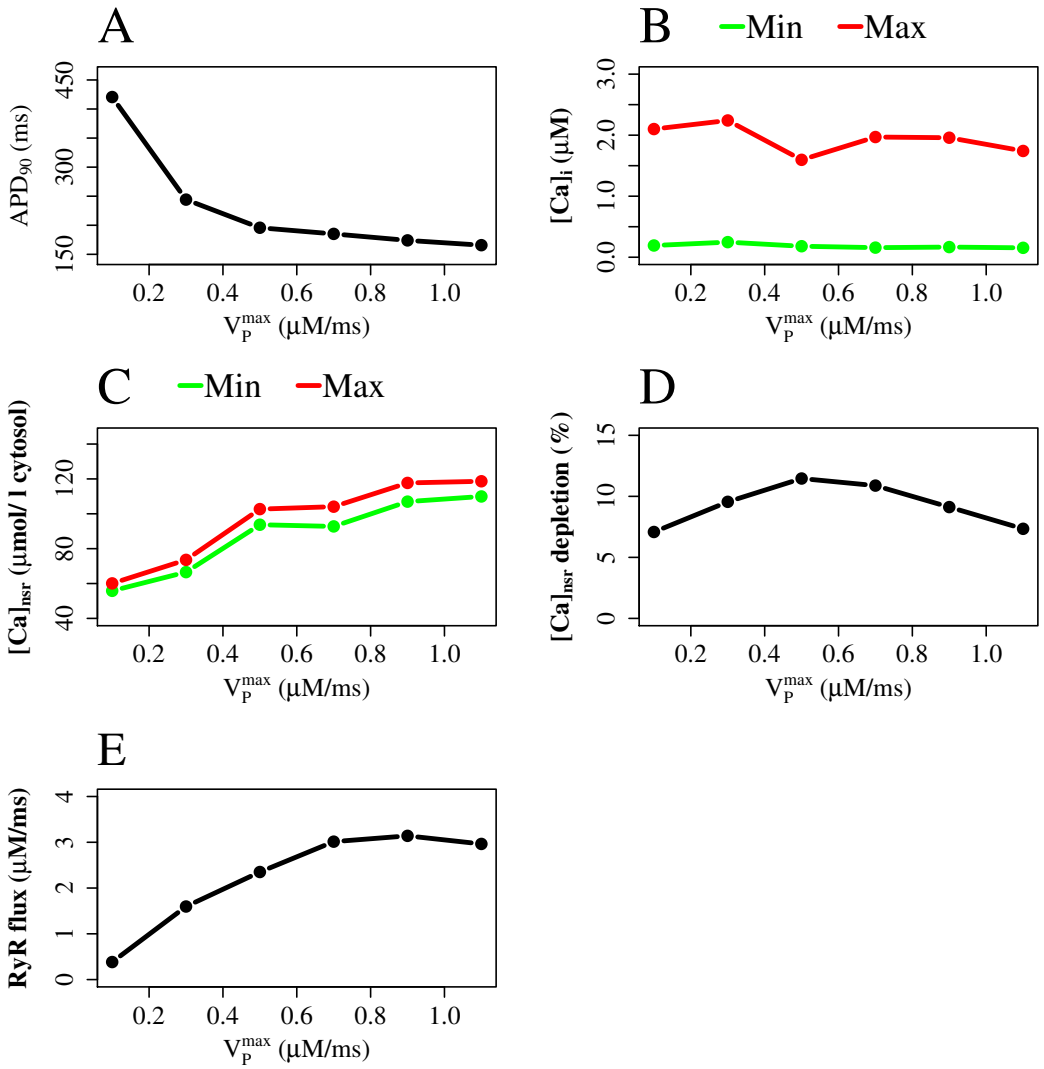

Figure 12: **Varying V_P^{max} with K_P equal to 0.4 µM: (A)** - APD_{90}, **(B)** - Peak and resting $[Ca^{2+}]_i$ (in red and green, respectively), **(C)** - Maximal and minimal nSR free $[Ca^{2+}]$ (in red and green, respectively), **(D)** - Depletion of nSR free $[Ca^{2+}]$ and **(E)** - Maximal RyR flux.

So far we used a simple SERCA model (Equation (7)), but, as discussed in Chapter 4.2, this model shows Ca^{2+} transport into the SR even if the $[Ca^{2+}]_i$ is very low during diastole. This would not occur *in vivo*, because the concentration gradient across the membrane of the SR is too large [132]. The SERCA model of Sneyd et al. [154] has the advantage of SERCA Ca^{2+} uptake inhibition by high nSR free $[Ca^{2+}]$ load (see Equation (43)). We explored the use of this SERCA model (Equation (43)) by replacing the former simple SERCA model. We ran two simulations with the same parameter set and with the different SERCA models, respectively. The results of the first model (Equation (7)) are shown in Figure 13 and the results of the Sneyd model (Equation (43)) are shown in Figure 14. The J_{up} of the Sneyd model (Figure 14E) reached a higher maximum value of 5.2 µM/ms compared to 3.9 µM/ms of the simple model. The nSR free $[Ca^{2+}]$ of the Sneyd model reached a higher maximum value after the second AP compared to the simple model. The $[Ca^{2+}]_i$ was too high with a peak value of 3.0 µM for the first AP and there were more RyR openings during diastole in the Sneyd model than in the simple model during diastole (compare J_{rel} in Figure 13E and 14E). The I_{Ks} had a higher maximum value in the Sneyd model (Figure 14E). Other key features of the simulation results, such as the shape of the AP voltage plot, were unaffected by the different SERCA models.

The openings of few RyRs during diastole using the Sneyd SERCA model was appreciated as it simulates stochastic RyR openings, which cause spontaneous Ca^{2+} sparks. Such spontaneous Ca^{2+} sparks were observed in experiments under resting conditions [21]. The advantages of the Sneyd model outweighed the disadvantages, so it was therefore used in the subsequent simulations. However, the peak $[Ca^{2+}]_i$ was too high compared to the target value of ∼1.1 µM [118, 6, 11, 149]. Next, we aimed to reduce the $[Ca^{2+}]_i$ by changing calsequestrin concentration and the refill flux.

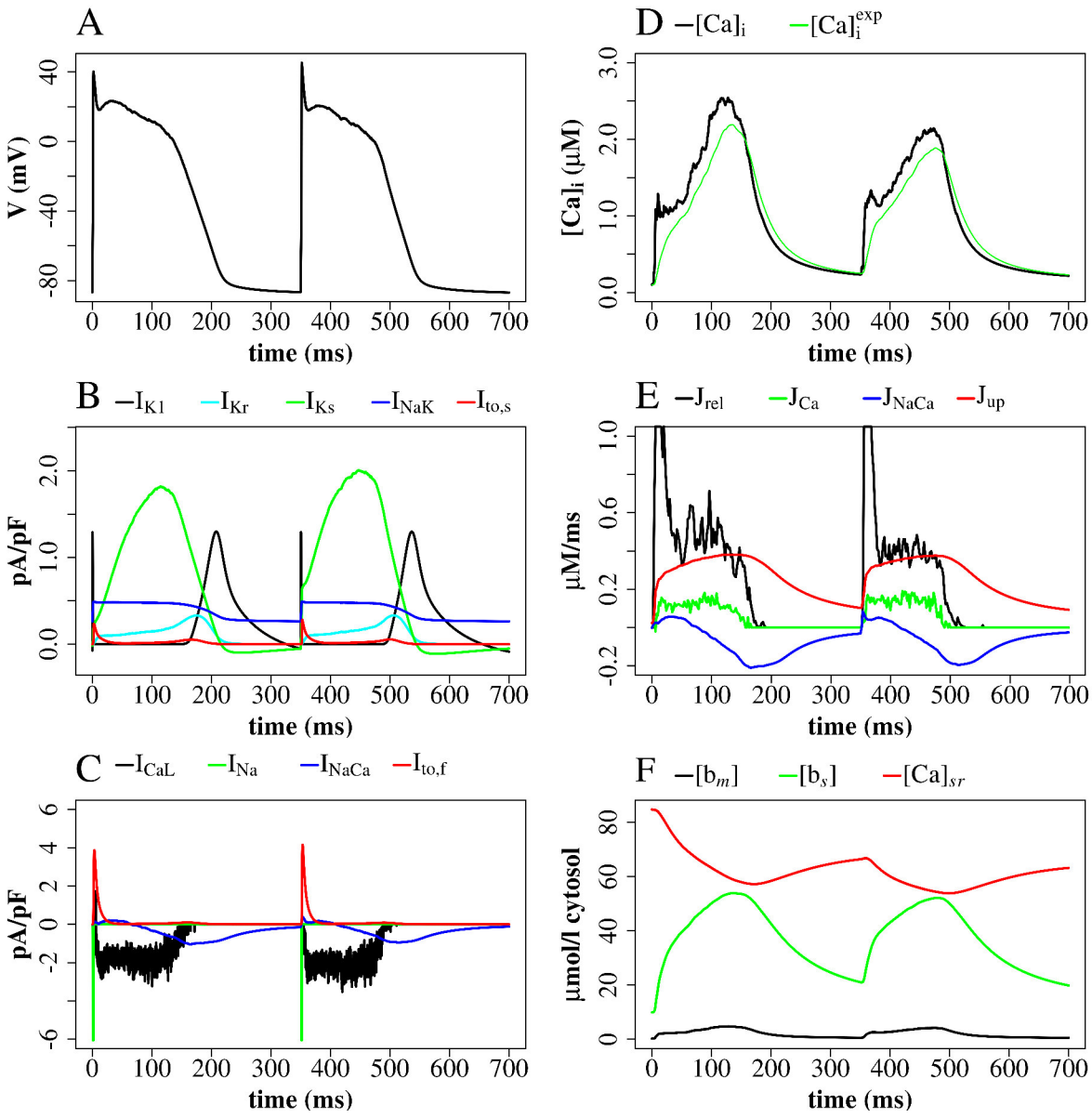

Figure 13: **Simulation with the simple SERCA model (Equation** (7)**):** Membrane potential, ionic currents, and concentrations, a stimulus every 350th ms **(A)** - Membrane potential. **(B)** - Currents I_{K1}, I_{Kr}, I_{NaK}, and $I_{to,s}$. **(C)** - LCC current (I_{CaL}), Na^+/Ca^{2+}-exchanger current (I_{NaCa}), $I_{to,f}$, and I_{Na} (truncated). **(D)** - Average cytosolic $[Ca^{2+}]_i$ and $[Ca^{2+}]_i^{exp}$ as defined in Equation (25). **(E)** - Ca^{2+} -fluxes: J_{rel} (truncated), J_{Ca}, J_{NaCa}, J_{up}. **(F)** - Buffer-bound $[Ca^{2+}]_i$ ($[b_m]$, $[b_s]$) and nSR free $[Ca^{2+}]$ ($[Ca_{sr}]$) are plotted. $[b_m]$ and $[b_s]$ are in conventional concentrations in units of μM whereas $[Ca_{sr}]$ is expressed for simplicity in units of μM ν_{sr}/ν_{cyt} (μmol/l cytosol). Plots show the first two APs of a simulation with a quarter of a z-disc.

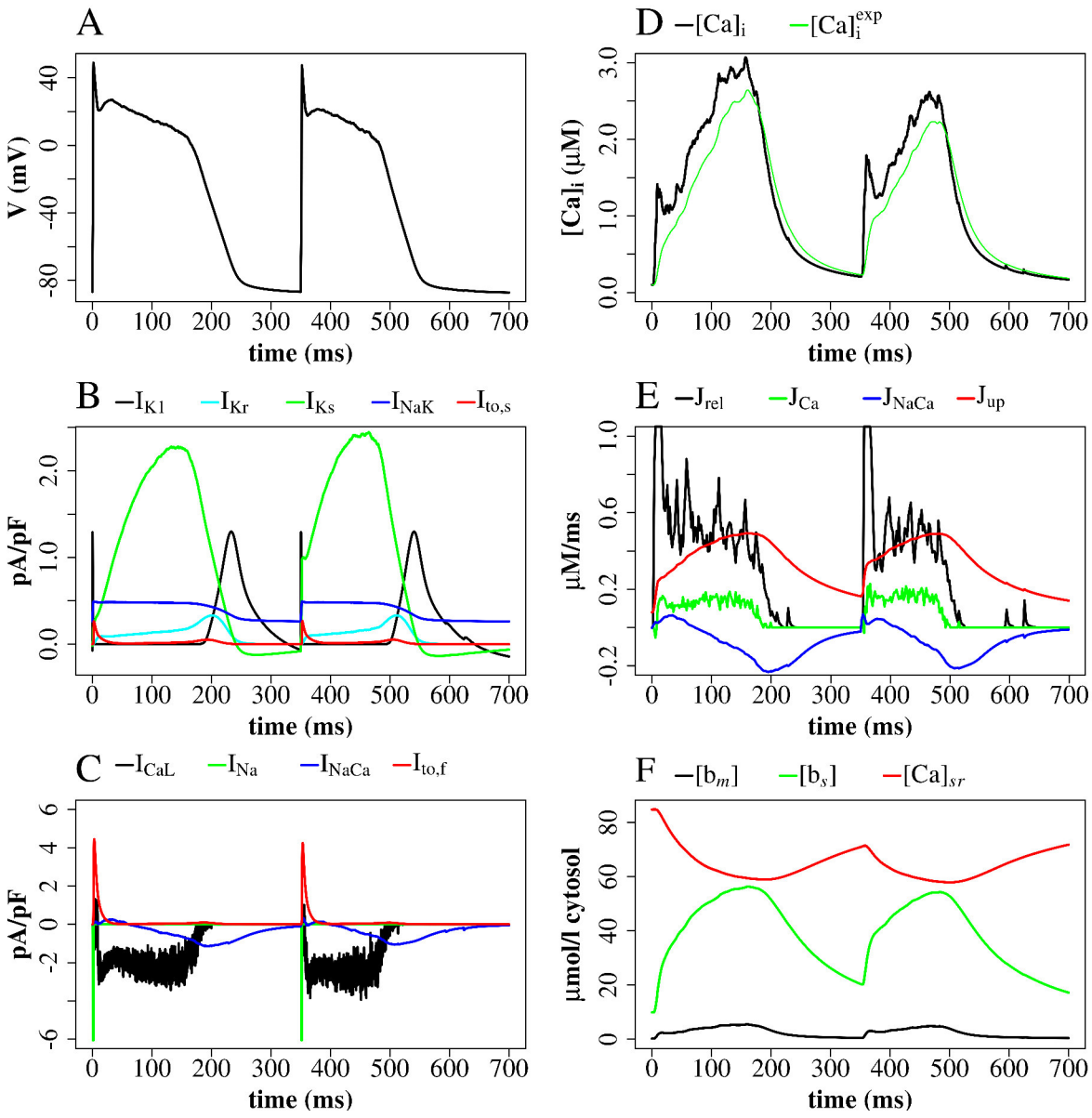

Figure 14: **Simulation with the Sneyd SERCA model (Equation** (43)**):** Membrane potential, ionic currents, and concentrations, a stimulus every 350th ms **(A)** - Membrane potential. **(B)** - Currents I_{K1}, I_{Kr}, I_{NaK}, and $I_{to,s}$. **(C)** - LCC current (I_{CaL}), Na^+/Ca^{2+}-exchanger current (I_{NaCa}), $I_{to,f}$, and I_{Na} (truncated). **(D)** - Average cytosolic $[Ca^{2+}]_i$ and $[Ca^{2+}]_i^{exp}$ as defined in Equation (25). **(E)** - Ca^{2+} -fluxes: J_{rel} (truncated), J_{Ca}, J_{NaCa}, J_{up}. **(F)** - Buffer-bound $[Ca^{2+}]_i$ ($[b_m]$, $[b_s]$) and nSR free $[Ca^{2+}]$ ($[Ca_{sr}]$) are plotted. $[b_m]$ and $[b_s]$ are in conventional concentrations in units of µM whereas $[Ca_{sr}]$ is expressed for simplicity in units of µM ν_{sr}/ν_{cyt} (µmol/l cytosol). Plots show the first two APs of a simulation with a quarter of a z-disc.

4.3.2 Calsequestrin and refill flux

In accordance with the results of Chapter 4.3.1, we used the parameter K_p of 0.4 µM and the Sneyd model for the subsequent analyses. Again we varied V_P^{max} from 0.1 µM/ms to 1.1 µM/ms. The results are shown in Figure 15. APD_{90} decreased with increasing V_P^{max}, but only slowly with V_P^{max} values higher than 0.7 µM/ms (Figure 15A). The peak $[Ca^{2+}]_i$ increased from 1.61 µM to 2.95 µM with increasing V_P^{max} from 0.3 µM/ms to 1.1 µM/ms (Figure 15B, in red). The $[Ca^{2+}]_i$ was more affected by V_P^{max} for this parameter set than in the initial parameter set (Figure 12) as it marginally increased with increasing V_P^{max}. The maximal nSR free $[Ca^{2+}]$ increased from 64.4 µmol/l cyotsol to 139.68 µmol/l cyotsol (Figure 12C, in red) with increasing V_P^{max}, but the Ca^{2+} depletion was lower compared to the simple SERCA model. The plot of the nSR free $[Ca^{2+}]$ depletion (Figure 12D) shows a decrease from 5.8 % to 2.7 % with increasing V_P^{max}. The maximum RyR flux increased from 0.552 µM/ms to 4.71 µM/ms with the increase of V_P^{max} from 0.1 µM/ms to 1.1 µM/ms (Figure 15E).

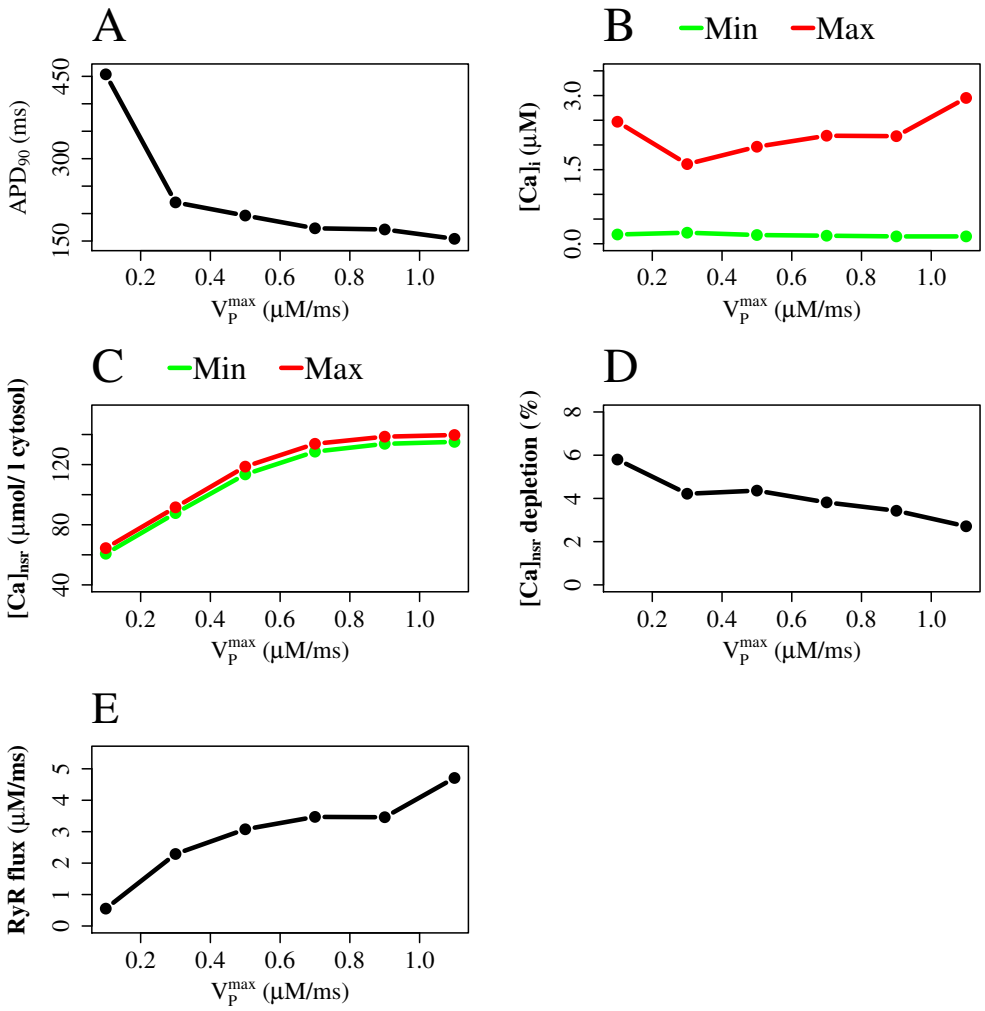

Figure 15: **Varying V_P^{max} with Sneyd model: (A)** - APD_{90}. **(B)** - Peak and resting $[Ca^{2+}]_i$ (in red and green, respectively). **(C)** - Maximal and minimal nSR free $[Ca^{2+}]$ (in red and green, respectively). **(D)** - Depletion of nSR free $[Ca^{2+}]$. **(E)** - Maximal RyR flux. K_P equal to 0.4 µM.

The basis of our model is the ODE-Mahajan model in which calsequestrin is assumed to be located in the whole SR. However, Terentyev et al. (2008) [156] demonstrated that calsequestrin is localized almost exclusively in the jSR in skeletal and cardiac muscle. This was already suggested by Meissner (1975) [157] and supported by Jorgensen et al. (1979) [158]. Based on these observations and literature research, calsequestrin was removed from the nSR in our model. The V_P^{max} analysis shown in Figure 16 revealed that the key output variables were almost unaffected by the removal of calsequestrin in the nSR indicated by the same behaviour. The nSR free $[Ca^{2+}]$ was overall marginally higher (Figure 16C) and its depletion was minimally affected by increasing V_P^{max} in contrast to the previous simulation (compare Figures 16C-D and Figures 15C-D). A V_P^{max} of 0.4 µM/ms seemed to be the best choice, because otherwise the $[Ca^{2+}]_i$ reached higher values than 2.0 µM and the nSR free $[Ca^{2+}]$ was higher than 120 µmol/l cyotsol with higher V_P^{max} values. The depletion of the nSR free $[Ca^{2+}]$ was too low with ∼2 % using a V_P^{max} of 0.3 µM/ms and ADP_{90} was too long with V_P^{max} values below 0.4 µM/ms.

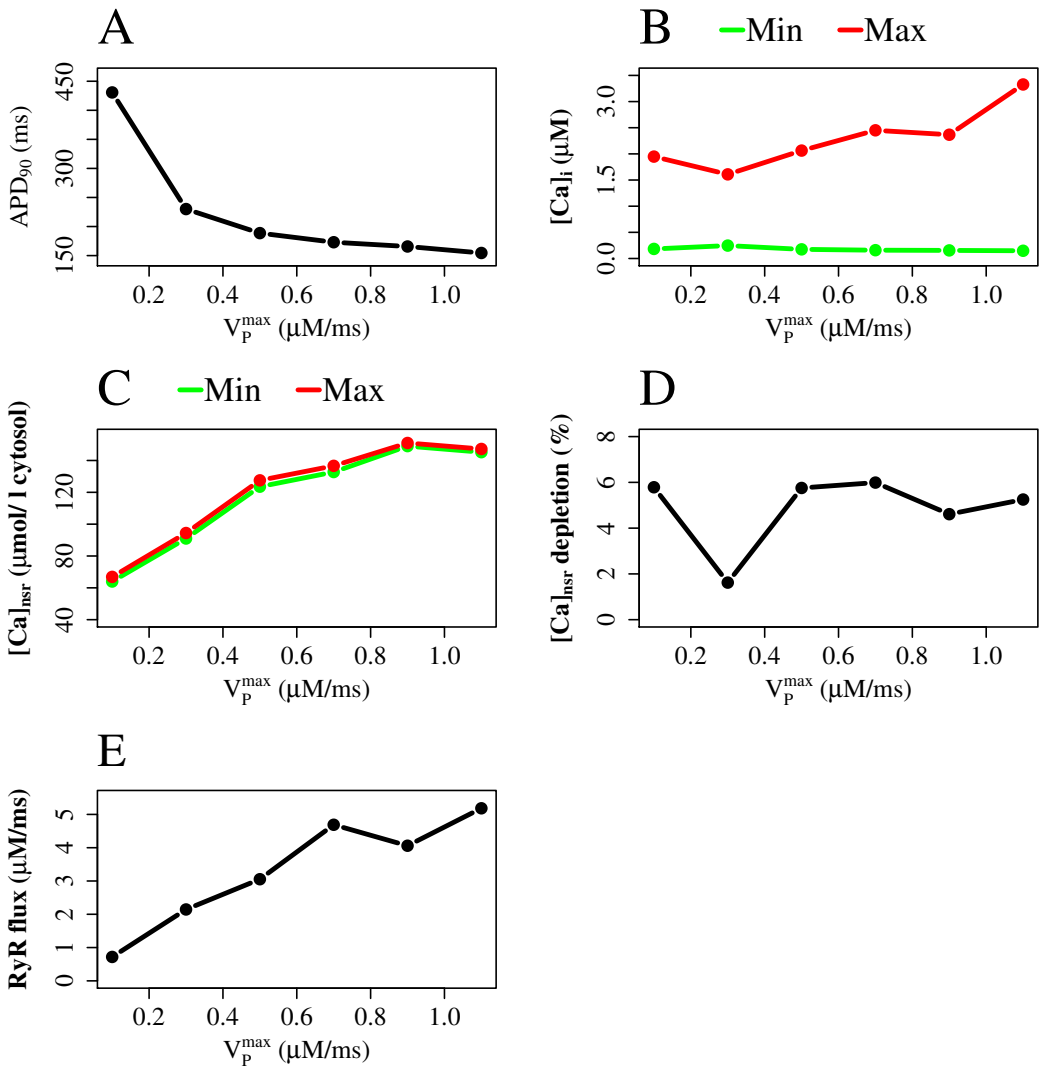

Figure 16: **Varying V_P^{max} without calsequestrin in the nSR: (A)** - APD_{90}. **(B)** - Peak and resting $[Ca^{2+}]_i$ (in red and green, respectively). **(C)** - Maximal and minimal nSR free $[Ca^{2+}]$ (in red and green, respectively). **(D)** - Depletion of nSR free $[Ca^{2+}]$. **(E)** - Maximal RyR flux. K_P equal to 0.4 µM.

The concentration of calsequestrin ($[B_{sr}]$) was varied between 0 µM and 2000 µM in 11 simulations with a BCL of 350 ms. The key output variables were again: (1) APD_{90}, (2) minimum (resting) and maximum (peak) $[Ca^{2+}]_i$, (3) maximum RyR flux, (4) minimum and maximum nSR free $[Ca^{2+}]$, and (5) the depletion of the nSR free $[Ca^{2+}]$. The average values of three consecutive APs were calculated and are plotted in Figure 17. The APD_{90} varied between 157.2 ms and 178.3 ms with increasing $[B_{sr}]$ (Figure 17A). The peak $[Ca^{2+}]_i$ also varied, but it increased with increasing $[B_{sr}]$ (Figure 17B). In contrast, the nSR free $[Ca^{2+}]$ marginally decreased with increasing $[B_{sr}]$ and likewise the depletion of nSR free $[Ca^{2+}]$ was clearly reduced (Figure 17C and 17D). The RyR flux considerably increased with increasing $[B_{sr}]$ (Figure 17E). $[B_{sr}]$ primarily increased the RyR flux and decreased the depletion of nSR free $[Ca^{2+}]$. A value of 800 µM for $[B_{sr}]$ was the best trade-off between our aims for a short APD_{90}, a low peak $[Ca^{2+}]_i$ of ∼1.1 µM, but a high depletion of nSR free $[Ca^{2+}]$ and a nSR free $[Ca^{2+}]$ of ∼80 µmol/l cytosol.

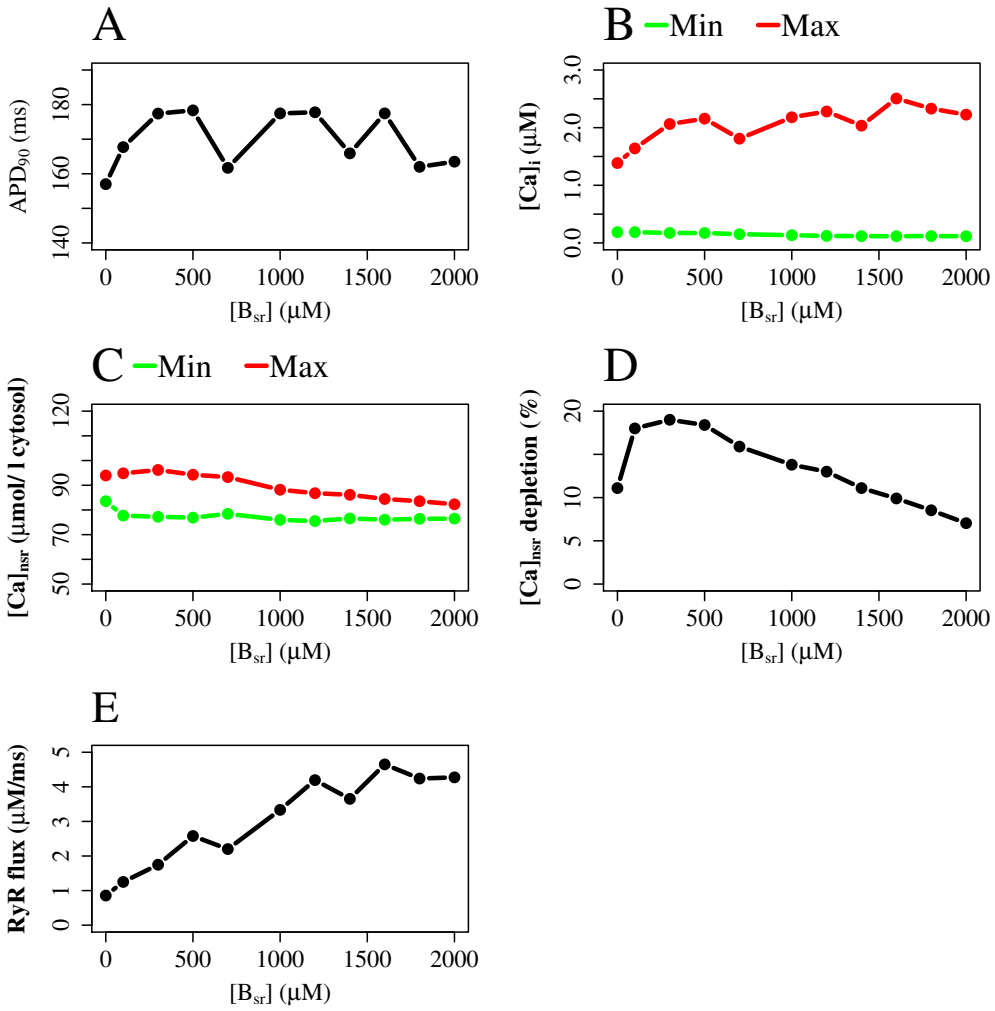

Figure 17: **Varying calsequestrin concentration in the jSR: (A)** - APD_{90}. **(B)** - Peak and resting $[Ca^{2+}]_i$ (in red and green, respectively). **(C)** - Maximal and minimal nSR free $[Ca^{2+}]$ (in red and green, respectively). **(D)** - Depletion of nSR free $[Ca^{2+}]$. **(E)** - Maximal RyR flux. K_P equals 0.4 µM, V_P^{max} equals 0.4 µM/ms and no nSR Ca^{2+}-buffer.

A key parameter for the refill flux of the jSR is the delay constant τ_d (see Equation (11)). The delay constant τ_d was varied from 2 ms to 7 ms in Figure 18 using a value of 800 µM for $[B_{sr}]$ as determined previously. The key output variables were again: (1) APD_{90}, (2) minimum (resting) and maximum (peak) $[Ca^{2+}]_i$, (3) maximum RyR flux, (4) minimum and maximum nSR free $[Ca^{2+}]$, and (5) the depletion of the nSR free $[Ca^{2+}]$. A τ_d lower than 2 ms showed no characteristic overshoot at the beginning of the AP to positive membrane potential values. APD_{90} and nSR free $[Ca^{2+}]$ increased with increasing τ_d (Figure 18A and 18C), but the depletion of nSR free $[Ca^{2+}]$ decreased (Figure 18D). The $[Ca^{2+}]_i$ and the RyR flux were almost unaffected by changing τ_d (Figure 18B and 18E). The highest and therefore most desirable depletion of nSR free $[Ca^{2+}]$ with ∼35 % was achieved with τ_d equalled to 2 ms, but then nSR free $[Ca^{2+}]$ was too low with a value of ∼64 µmol/l cytosol. Using a τ_d of 4 ms showed a reasonable APD_{90} of ∼190 ms and nSR free $[Ca^{2+}]$ of ∼72 µmol/l cytosol, but the peak $[Ca^{2+}]_i$ was still too high with ∼2.4 µM.

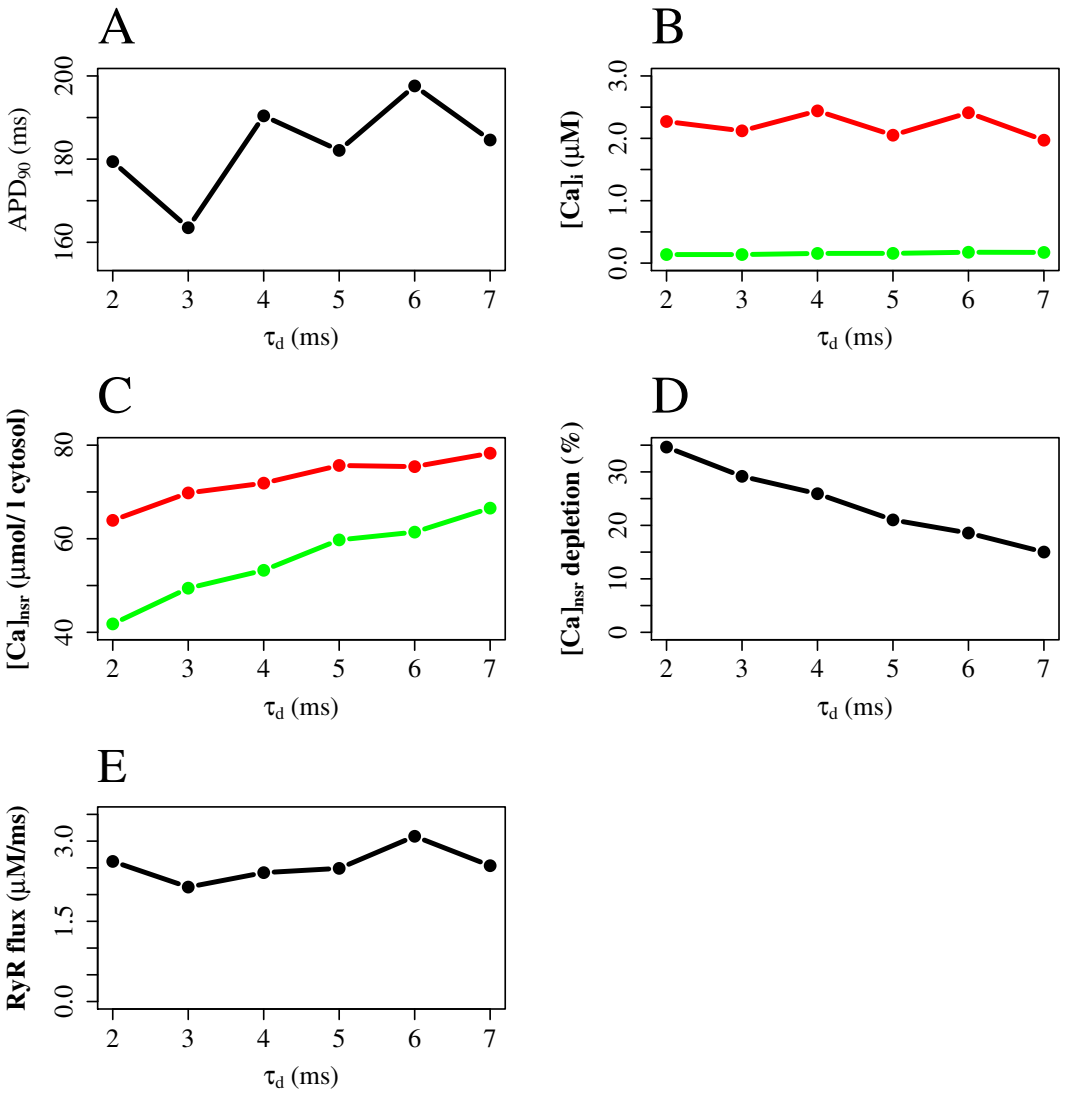

Figure 18: **Varying τ_d of the refill flux: (A)** - APD_{90}. **(B)** - Peak and resting $[Ca^{2+}]_i$ (in red and green, respectively). **(C)** - Maximal and minimal nSR free $[Ca^{2+}]$ (in red and green, respectively). **(D)** - Depletion of nSR free $[Ca^{2+}]$. **(E)** - Maximal RyR flux.

The simulation results with the improved SR parameters is shown in Figure 19 for three APs using a τ_d of 4 ms. The third AP was quite similar to the second one, which indicated that the Ca^{2+} dynamics were not far from the steady state. The currents still reproduced basic features of the ODE-Mahajan model [6] and experimental plots of rabbit Ca^{2+} currents [118], but the peak $[Ca^{2+}]_i$ was higher with a value of ∼2.0 µM for the third AP.

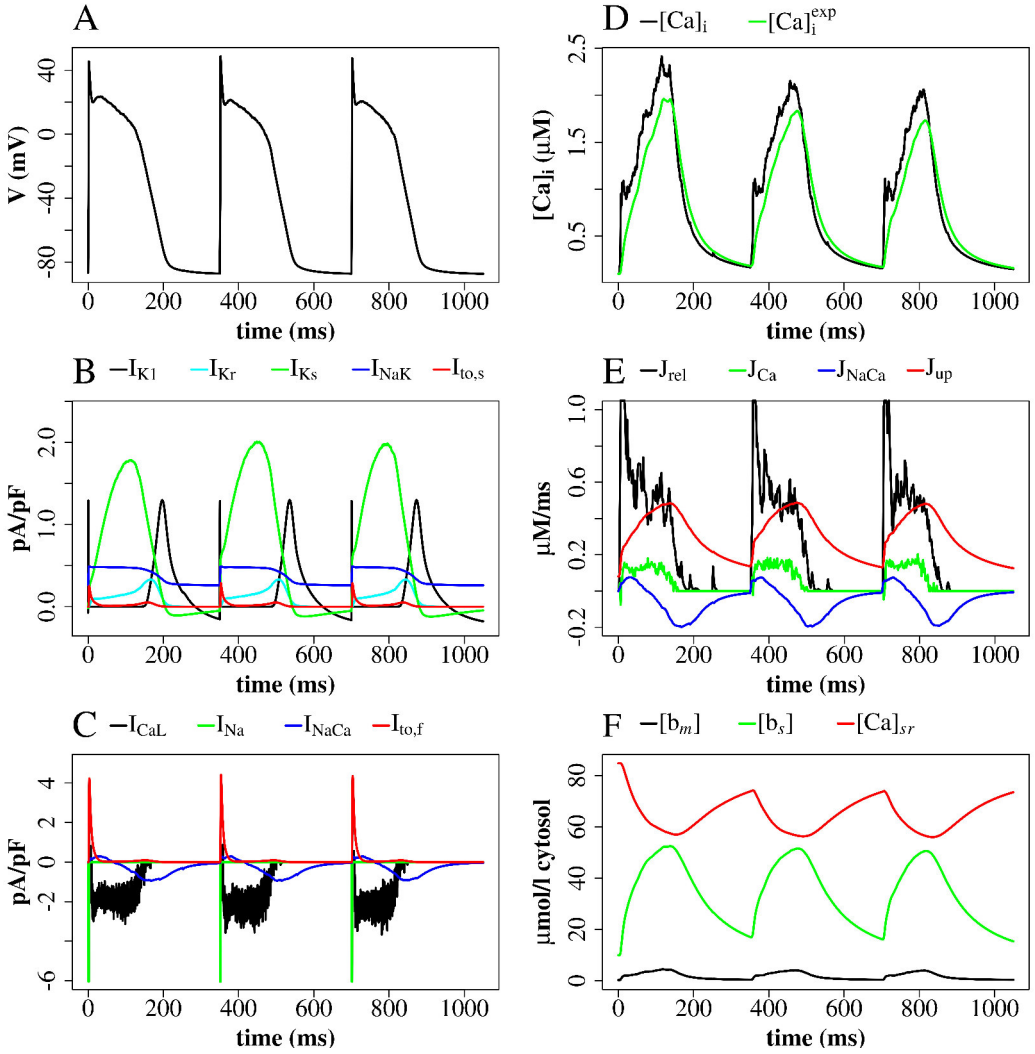

Figure 19: **Improved SR parameter set:** Membrane potential, ionic currents, and concentrations, a stimulus every 350th ms **(A)** - Membrane potential. **(B)** - Currents I_{K1}, I_{Kr}, I_{NaK}, I_{NaK} and $I_{to,s}$. **(C)** - LCC current (I_{CaL}), Na^+/Ca^{2+}-exchanger current (I_{NaCa}), $I_{to,f}$, and I_{Na} (truncated). **(D)** - Average cytosolic $[Ca^{2+}]_i$ and $[Ca^{2+}]_i^{exp}$ as defined in Equation (25). **(E)** - Ca^{2+} -fluxes: J_{rel} (truncated), J_{Ca}, J_{NaCa}, J_{up}. **(F)** - Buffer-bound $[Ca^{2+}]_i$ ($[b_m]$, $[b_s]$) and nSR free $[Ca^{2+}]$ ($[Ca_{sr}]$) are plotted. $[b_m]$ and $[b_s]$ are in conventional concentrations in units of µM, whereas $[Ca_{sr}]$ is expressed for simplicity in units of µM ν_{sr}/ν_{cyt} (µmol/l cytosol). Plots show the first three APs of a simulation with a quarter of a z-disc.

4.4 Improved SR parameter set

The analysis of the SR parameters has provided an improved model parameter set. The explored parameters were varied within their possible physiological ranges according to the literature. The best values for the SERCA parameters were determined to be K_P set to 0.4 µM and V_P^{max} set to 0.4 µM/ms. Using K_P values lower than 0.4 µM resulted in APD_{90} values becoming too long for the tested V_P^{max} range. APD_{90} should be ∼185 ms at a BCL of 350 ms [147, 148]. With $K_P = 0.4$ µM and $V_P^{max} = 0.5$ µM/ms the APD_{90} was 195.7 ms, which was marginally to high. Hence, V_P^{max} of 0.4 µM/ms was a better choice. The simple SERCA model was replaced by the Sneyd model [154] because of its advantage that the SR $[Ca^{2+}]$ works as feedback inhibitor. However, the peak $[Ca^{2+}]_i$ of the second AP was too high with a value of ∼2.5 µM. Further parameter fitting was necessary after the SERCA substitution. Our cell model is based on the ODE-Mahajan model, in which calsequestrin is localized in the whole SR. However, according to the literature, calsequestrin is localized only in the jSR [156] and calsequestrin was removed from the nSR in our model. The effect was minor, so that a direct analysis of the influence of the calsequestrin concentration was performed. The target value for the peak $[Ca^{2+}]_i$ was ∼1.1 µM [118, 6, 11, 149] with at the same time high depletion of nSR free $[Ca^{2+}]$ [151]. The most appropriate value for the calsequestrin concentration ($[B_{sr}]$) was 800 µM, because the ADP_{90} was of appropriate duration and the peak $[Ca^{2+}]_i$ was not too high. However, the depletion of the nSR free $[Ca^{2+}]$ was marginally too low with ∼15 %, but at the same time a target maximal nSR free $[Ca^{2+}]$ of 80 µmol/l cytosol was achieved. Choosing τ_d of 4 ms [6] resulted in a higher depletion of 20 %, but the maximal nSR free $[Ca^{2+}]$ was then moderately too low at ∼70 µmol/l cytosol. We aimed for a depletion of nSR free $[Ca^{2+}]$ of ∼50 % [150] or at least in the range of 20 % - 60 % [151].

4.5 Conclusions

The aim of this analysis was to provide an improved model parameter set with respect to SR Ca^{2+} dynamics. We successfully adjusted the parameters to improve specific key features of the model, such as APD_{90}, Ca^{2+} transient shape, RyR flux and the behaviour of nSR free $[Ca^{2+}]$, which were important for the subsequent chapters in terms of the role of NCX, spark behaviour, and the extension of our model through the addition of mitochondria. The induction decay mechanism mainly caused the CICR termination after we adjusted the buffer parameters, calsequestrin localization, and the refill flux. A strong buffering (buffer factor β) was no longer necessary. We approximated sufficiently our target values for the key output variables except for peak $[Ca^{2+}]_i$, which was still too high with ∼2 µM during the third AP. We did not optimize other features, for example potassium currents, because we do not consider them to have a dramatic effect on the overall objectives of our subsequent analyses. We explored the parameters within their physiological range of experimental uncertainty and chose the values which gave the physiologically most realistic Ca^{2+} dynamics. It was challenging to validate the chosen parameter values with respect to the literature because of high variability in literature reports, limited studies in rabbits and possible differences between rabbits and other species. In some cases there is very limited experimental information on parameter values, for example τ_d. A systematic analysis of the components of the SR has been performed and we selected the parameters such that the target values were sufficiently approximated. This fine-tuning of parameters is a major part of modelling and provides the basis for further analyses, improvements, and extensions of the model.

5 Modelling and investigation of the sodium-calcium exchanger (NCX)

5.1 Introduction

We investigated the influence of different SR parameters on key output variables, such as APD_{90}, $[Ca^{2+}]_i$, RyR flux, and nSR free $[Ca^{2+}]$. The parameter changes conducted in the previous Chapter 4 are listed in the Tables A.1 and A.2 in the Column "Chapter 5 & 6", respectively. These parameter changes are the basis for the investigation of our Na^+/Ca^{2+}-exchanger implementation and the physiological role of the Na^+/Ca^{2+}-exchanger for the Ca^{2+} dynamics carried out in this chapter.

5.1.1 Sodium-calcium exchanger

The sodium-calcium exchanger (NCX) is an ion transport protein located in the plasma membrane of most cells [42]. NCX is a bi-directional exchanger which extrudes Ca^{2+} from the cell in exchange for sodium ions or extrudes sodium ions in exchange for Ca^{2+}. As a secondary active transporter the net direction of the Ca^{2+} transport depends on the membrane potential, as well as on the $[Na^+]$ and $[Ca^{2+}]$ inside and outside the cell [42]. The two important modes of NCX are called forward mode and reverse mode. The forward mode is a Ca^{2+} efflux and the reverse mode is a Ca^{2+} influx [159]. NCX has been observed to also mediate Ca^{2+}/Ca^{2+} exchange and Na^+/Na^+ exchange in different tissues, but these modes might not be important for net ion translocation [159]. The coupling ratio is 3 Na^+ : 1 Ca^{2+} [159, 160] and this exchange involves a net movement of one positive charge in the direction of the sodium ions [42]. Considering all reported transport modes, the actual exchange ratio was calculated to be 3.2 : 1 [161].

5.1.2 Structure and regulation

The NCX protein is 938 amino acids long and contains 10 transmembrane segments [42, 162]. The NCX family contains eight members including the mammalian exchangers NCX1, NCX2, and NCX3 [42]. These genes are expressed differently in tissue. The NCX1 is mostly found in heart, kidney, and brain. NCX2 is predominatly expressed in brain and NCX3 is found mainly in brain and skeletal muscle [163].
NCX is dynamically regulated by factors such as $[Na^+]$, $[Ca^{2+}]$, intracellular pH, ATP, phosphatidyl-inositol-4,5-biphosphate (PIP_2), phosphorylation, and others [160]. Ca^{2+} activates the exchanger by binding to a high-affinity binding site of the intracellular loop [42, 164]. In contrast, Na^+ inhibits the outward Na^+/Ca^{2+} exchange by binding to transport sites of NCX [42, 164]. This allosteric regulation is observed at high $[Na^+]_i$ above 20 mM [165]. NCX currents are stimulated by the addition of ATP in experiments, which induces the production of PIP_2 [42]. In some tissues phosphorylation seems to stimulate the NCX activity by increasing the affinity for Ca_i^{2+} and Na_o^+ [42].
Many synthetic inhibitors have been developed becoming increasingly potent and selective. The prototype benzyloxyphenyl NCX inhibitor KB-R7943 has been developed in 1996 [166], but it still has the disadvantage of inhibiting other currents as well [167, 168]. Since then, more selective inhibitors have been studied: SEA0400, SN-6, and YM-244769 [166]. But these benzyloxyphenyl inhibitors are mostly active during reverse mode and under high $[Na^+]_i$ [166]. Some ion channel blockers show inhibitory effects on NCX, for example amiodarone, dronedarone, bepridil, aprindine, and cibenzoline [166]. SEA0400

is a more selective inhibitor and has a ten-fold higher potency than KB-R7943 [167]. However, because of the NCX blockers still being poorly selective, a NCX knockout is the better choice for experimental studies to clearly demonstrate the role of NCX [169]. As long as there are no highly specific drugs for manipulating NCX, a complete understanding of its roles remains illusive [170].

5.1.3 Physiological relevance of the NCX flux

The main role of NCX is the extrusion of Ca^{2+} to maintain a low $[Ca^{2+}]_i$. The external $[Ca^{2+}]$ is ∼2.0 mM and much higher than the free $[Ca^{2+}]_i$ of cardiac myocytes (0.1 µM during diastole) [159]. $[Na^+]$ has a much smaller concentration gradient across the membrane. $[Na^+]_i$ is ∼10 mM and $[Na^+]_o$ is 120 mM - 145 mM [159]. The resulting inwardly directed electrochemical gradient for Ca^{2+} and Na^+ enables a huge ion influx at the beginning of an AP, which is amplified by the initially negative membrane potential [159]. In the AP there is a massive Na^+ influx via the opening Na^+ channels, which is followed by Ca^{2+} influx via the voltage-dependent LCCs. NCX is responsible for Na^+ removal during the first milliseconds of an AP and later for Ca^{2+} removal. The relative abundance of NCX in cardiac muscle indicates its importance. It is considered to be particularly relevant in Ca^{2+} homoeostasis [42].
Similar to the contribution of SERCA for Ca^{2+} removal (see Chapter 4.1.2), the contribution of NCX to the Ca^{2+} extrusion varies between species [40]. Since NCX has to counteract the relatively high Ca^{2+} influx by the LCCs during long APs, it is more important in species with a short heart rate and a long AP, such as guinea-pigs and humans, than in species with short APs, such as mice and rats [132]. In rabbits the NCX is responsible for 28 % of the Ca^{2+} removal, whereas in rats it contributes only 7 % to the Ca^{2+} removal [171]. In a mouse a global knockout of NCX leads to its death, whereas a knockout only in ventricular cardiac myocytes is not lethal [172]. The cardiac myocytes can compensate for the loss by limiting the Ca^{2+} influx and reducing the transsarcolemmal Ca^{2+} fluxes [172]. Under pathological conditions an increased Ca^{2+} influx via NCX causes a Ca^{2+} accumulation, which can lead to myocardial necrosis, contractile failure and arrhythmias [170]. An altered NCX expression level is observed in heart failure [170]. Thereby, NCX modulation has even been suggested as therapeutic approach in arrhythmia and heart failure [173, 174, 175].

5.1.4 Controversies in NCX cardiac physiology

NCX has been studied for many decades, but its function, physiological role, and pathological role remain issues for discussions. The development of potent and specific inhibitors is an ongoing project. The survival of mice with a cardiac myocyte-specific NCX knockout raises questions about how crucial is its role in CICR.

Microdomains An important role in electrophysiology might play microdomains. Such functionally restricted intracellular spaces have also been named “fuzzy spaces” and were already postulated by Lederer at al. (1990) [176]. If NCX is located near the sodium channels, then it could be regulated by a locally high $[Na^+]_i$, which exceeds the global average $[Na^+]_i$ [176]. Generally, the influence of Na^+ on the NCX is less well studied than the effects of Ca^{2+} [170]. NCX may be regulated by these Ca^{2+} microdomains, where local $[Ca^{2+}]$ increases faster reaching a higher value than the $[Ca^{2+}]_i$. In some models a restricted subspace or a submembrane $[Ca^{2+}]$ has been introduced (for example

[6, 60, 61]), but its actual values and dynamics can only be assumed. J_{NaCa} is the second main contributor after J_{pump} for Ca^{2+} extrusion and for this reason it has to be in forward mode most of the time during one Ca^{2+} cycle. The forward mode can only be achieved with high $[Ca^{2+}]_i$ and/or low $[Na^+]_i$ during the plateau phase of an AP. The NCX regulation by Ca^{2+} and Na^+ is still not fully understood, because it is not well studied and the separation of the effect of Ca^{2+} on the transport or on the regulatory sites is challenging [170].

Distribution In the light of the hypotheses of the existence of microdomains, the cellular distribution of NCX is crucially important to any model of CICR. Experimental approaches have been used to map and visualize NCX location, but the results between these studies have often been inconsistent. It was initially claimed by Scriven et al. (2000) [125] that there are no NCX in the dyadic clefts, but the evidence showing that NCX is distributed throughout the membrane, including the CRUs, is growing [124, 127, 177, 178]. There is even some evidence that NCX could be accumulated at the CRU [124, 179, 180]. The widespread distribution of NCX on the sarcolemma may indicate its possible multiple roles in CICR and it is therefore important to determine the distribution of NCX and its consequences [170].

Triggering If NCX is located mostly inside the CRU and is regulated by a locally high $[Ca^{2+}]_i$ and $[Na^+]_i$, it may play a role in triggering the CICR. The local $[Na^+]_i$ could be high enough to reverse NCX such that Ca^{2+} enters the dyadic cleft via NCX in early stages of the AP, thus potentially activating RyRs [181, 182, 183, 184, 185, 186]. This way of RyR activation is less effective than the activation by the LCC openings, but could be an alternative or backup system [187]. The Ca^{2+} influx through the NCX could precede and prime the dyadic cleft with Ca^{2+} [42, 188]. Hence, the RyRs can then be activated more easily by the LCCs [42]. This idea is supported by Larbig et al. (2010) [183] and Torres et al. (2010) [189] who claim that neuronal Na^+ channels are also located in the dyadic cleft. Hence, NCX would be regulated by a locally high $[Na^+]_i$. However, the Ca^{2+} flux of NCX is much smaller than Ca^{2+} flux of the LCCs and some authors argued that the Ca^{2+} flux of NCX is not strong enough to trigger RyRs [190, 191, 192]. Notably, the NCX Ca^{2+} transient is not believed to be strong enough to directly activate myofilaments, and hence, it does not effect the muscle contraction directly [185]. However, J_{Ca} and J_{NaCa} might have a synergistic effect [189].

Sparks Other important roles of NCX could be the reduction of spark frequency, coupling fidelity, and diastolic $[Ca^{2+}]_i$ during diastole or at rest without influencing the spark amplitude and duration [193, 194, 134, 43]. A single, random RyR opening during diastole, an event known as quark, can enhance the opening of further RyRs in its neighbourhood, known as spark [19]. The probability that a single open RyR activates any other RyR in the CRU is called the coupling fidelity [195]. The Ca^{2+} efflux via such sparks may activate further RyRs and lead to a massive Ca^{2+} release, which then could generate a complete AP. A co-localization of RyR and NCX may enable the NCX to quickly extrude the Ca^{2+} released by a spark. The local $[Ca^{2+}]$ increase would be reduced by NCX [43]. Hence, NCX inside and near CRUs may prevent spontaneous sparks and waves during diastole [194].

The mentioned possible roles of NCX to contribute to triggering RyRs during systole and to prevent regenerative Ca^{2+} sparks during diastole were combined by Chu et al. (2016) [43] by their "dual-role hypothesis".
We still aimed for the target values defined in the previous Chapter 4 and listed in Table A.6, especially a APD_{90} of ∼185 ms, a peak $[Ca^{2+}]_i$ of ∼1.1 µM and a high depletion of nSR free Ca^{2+}.

5.2 Modelling of NCX

The calculation and the implementation of the NCX flux (J_{NaCa}) are described in Chapter 2.3.

5.2.1 Submembrane calcium concentration

We used the formulation of the NCX flux by Mahajan et al. (2008) [6], which is based on the equation by Luo and Rudy (1994) [58] and was modified by Hund and Rudy (2004) [196] :

$$J_{\mathrm{NaCa}} = g_{\mathrm{naca}} K_a \frac{\mathrm{e}^{\xi a}[Na^+]_i^3[Ca^{2+}]_o - \mathrm{e}^{(\xi-1)a}[Na^+]_o^3[Ca^{2+}]_s}{(1 + k_{\mathrm{sat}}\mathrm{e}^{(\xi-1)a})H}, \tag{45}$$

where

$$\begin{aligned} H =& K_{\mathrm{m,Cao}}[Na+]_i^3 + K_{\mathrm{m,Nao}}^3[Ca^{2+}]_s + K_{\mathrm{m,Nai}}^3[Ca^{2+}]_o\left(1 + \frac{[Ca^{2+}]_s}{K_{\mathrm{m,Cai}}}\right) \\ &+ K_{\mathrm{m,Cai}}[Na^+]_o^3\left(1 + \frac{[Na^+]_i^3}{K_{\mathrm{m,Nai}}^3}\right) + [Na^+]_i^3[Ca^{2+}]_o + [Na^+]_o^3[Ca^{2+}]_s, \end{aligned} \tag{46}$$

and where

$$K_a = \frac{1}{1 + (c_{\mathrm{naca}}/[Ca^{2+}]_s)^3}. \tag{47}$$

The parameters are listed in Table A.2. In this model NCX is regulated by the submembrane Ca^{2+} concentration ($[Ca^{2+}]_s$), which reaches an almost five times higher peak $[Ca^{2+}]$ than the bulk Ca^{2+} concentration ($[Ca^{2+}]_i$) and it peaks earlier. Both $[Ca^{2+}]$ transients during one AP are shown in Figure 20. In this approach Mahajan et al. (2008) [6] give consideration to the microdomains of the cell with higher local $[Ca^{2+}]$. However, they make the assumption of homogeneous $[Ca^{2+}]_s$ and do not consider local concentration gradients.
The actual $[Ca^{2+}]$ which regulates NCX is controversial in experiments as it can not be directly measured and computer models were used to estimate it [159, 197]. The assumption is that the $[Ca^{2+}]_s$ reaches higher values and peaks earlier than the average $[Ca^{2+}]_i$. Many attempts have been made to model such a $[Ca^{2+}]_s$. Trafford et al. (1995) [198] and ten Tusscher et al. (2004) [199] introduced a factor to estimate $[Ca^{2+}]_s$ from the $[Ca^{2+}]_i$. Weber et al. (2002) [118] extended this approach using exponential decay.
In our model the flux of NCX is linked with the reaction-diffusion model, which calculates $[Ca^{2+}]$ for each finite element. The NCX flux of each finite element is calculated using the local $[Ca^{2+}]$ (see Equation (14)). In contrast to the ODE-Mahajan model there is no explicit submembrane $[Ca^{2+}]$ in our model, because $[Ca^{2+}]$ is spatially resolved. The advantage of our modelling approach is that NCX is regulated by rapid, local events.

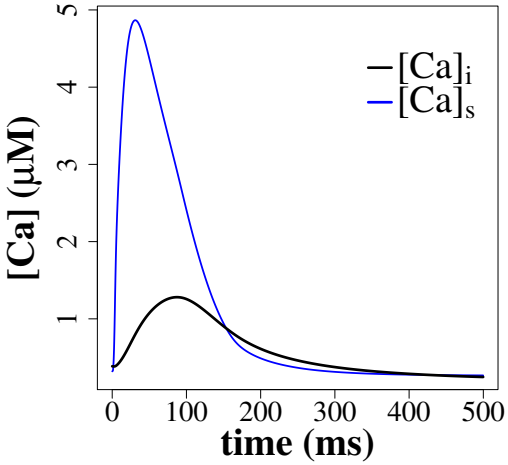

Figure 20: **The transient of $[Ca^{2+}]_i$ (in black) and submembrane Ca^{2+} concentration ($[Ca^{2+}]_s$) (in blue) during an AP using the ODE-Mahajan model [6].**

5.2.2 Spatial distribution of NCX in the dyadic cleft

In vivo NCX is located in the sarcolemma with its t-tubule system. In our model the z-discs are a representation of t-tubules where the CRUs are located. We places z-discs in distances of 2 µm. Experimental approaches revealed that NCX is not homogeneously distributed in the sarcolemma [159], but accumulated in the t-tubules (for example [178, 200]). The majority of the literature suggest a co-localization of NCX and RyRs [125, 124, 201, 180]. However, these results were based on experimental studies with rats and mice. Only Dash et al. 2007 [177] reported such a distribution for rabbits, but without concrete figures.
Jayasinghe et al. (2009) [124] investigated the distribution of NCX and RyRs for rats using confocal and total internal reflection fluorescence microscopy. They determined the distances between the centers of NCX punctae and RyR clusters. Jayasinghe et al. (2009) provided the percentages of punctate NCX at different distances to the nearest RyR cluster (see figure 4C of [124]).
We wanted to introduce a pre-factor, denoted as f_{NCX}, into our model so that NCX represents a spatial heterogeneous distribution according to the results of Jayasinghe et al. (2009) [124]. These results showed the highest NCX concentration towards the center of the CRUs and ∼25 % of the NCX label were within 150 nm of a CRU [124]. Hence, we assumed a maximum flux of NCX in the center of 100 %. Initially, we set the pre-factor f_{NaCa} to 1 at the center of each CRU to guarantee 100 % flux there. According to experimental results [124] the concentration of NCX decreases with increasing distance from the CRU center, and therefore our f_{NCX} was implemented to decrease likewise.
The histogram by Jayasinghe et al. (2009) (figure 4C of [124]) shows the distance of NCX to the nearest RyR cluster and the corresponding percentage of punctate NCX. We wanted to use this histogram to derive an equation to estimate f_{NCX} depending on its distance to the nearest RyR center. This histogram of distances between centers of NCX punctae and RyR clusters was generated from 3D data, which means that each bar of the histogram represented the percentage of NCX in a sphere with the radius being equal to the distance to the nearest RyR cluster center. Hence, we had to normalize the NCX percentages to the volumes of the corresponding spheres. The smallest distance of the

histogram was 0.5 µm, which was equivalent to the radius of the sphere representing the closest NCX. The percentage of NCX belonging to this distance with a value of 5.2 % was used as a reference for the other distances. The next distance of the histogram with a value of 1 µm corresponded to a spherical shell, because we had to subtract the volume of the inner sphere with a radius of 0.5 µm. The volumes of the spherical shells with the different distances or radii (0.1 µm - 0.55 µm) were used to normalize the percentages of the histogram to the first inner sphere (see Table A.7, Column "Volume factor").

$$Percentage = \frac{\%\text{ of punctuate NCX} \times 5.2}{\text{Volume factor}} \tag{48}$$

The percentages of NCX distribution for each spherical shell are listed in Table A.7 and have been plotted against the distances and fitted to an exponential function (using the R function *lm*). The fitted function was:

$$f^i_{\text{NCX}} = 0.008943\, e^{-15.7098 d_i}, \tag{49}$$

with d_i being the distance of the center of the ith element to the center of the nearest CRU. Jayasinghe et al. (2009) [124] considered NCX and RyRs to be co-localized, if the distance of NCX to a RyR cluster center is < 150 nm. In our model the CRU size varied highly. Therefore, we had to normalize the distance d_i to 0.15 µm to represent a co-localization of NCX and RyR in the whole CRU independent of its size.
For each finite element (i) the distance of its center to its nearest CRU (d_i) was determined and the corresponding f^i_{NCX} was calculated using Equation (49). Initially, we defined a single value for all surface finite elements ($f^{\text{surf}}_{\text{NCX}}$), but since Chapter 4 each surface finite element was assigned to the f_{NCX} of its corresponding volume finite element.

5.2.3 Spatial distribution of NCX in the whole cell

The assigned f_{NCX} represented the higher distribution of the NCX inside and near the CRUs as revealed in experimental approaches (for example [200, 124, 180]), but then the total NCX flux was much lower than in the ODE-Mahajan model. Simulations showed that a threshold for the lowest values ($f^{\text{low}}_{\text{NCX}}$) was necessary, otherwise large areas of the cell had no NCX flux even though t-tubules are known to extend through the whole cell. The maximum value ($f^{\text{high}}_{\text{NCX}}$) at the center of each CRU also had to be determined. One way to verify an appropriate parameter choice is the ratio of surface NCX flux ("Surface") to the NCX flux of the t-tubules ("Bulk") estimated in experimental approaches. We aimed for a maximum and minimum value for f_{NCX} such that the total NCX flux and the ratio of surface and bulk NCX flux were similar to literature values, which showed that at least 63 % of the I_{NCX} occurred in the t-tubules of rats [178]. NCX was found in 3.0 - 3.5 fold higher concentrations in the t-tubules [178]. An experiment on rabbit ventricular myocytes suggested that 67.2 % ± 2.7 % of the NCX is located in the interior of the cell [177]. Our simulations reflected such a distribution, if for $f^{\text{low}}_{\text{NCX}}$ set to 0.66 and $f^{\text{high}}_{\text{NCX}}$ set to 72.0. At the same time the total NCX flux at rest was the same as with the homogeneous NCX distribution. Surface, bulk, and total NCX fluxes for these parameters are shown in Figure 21.

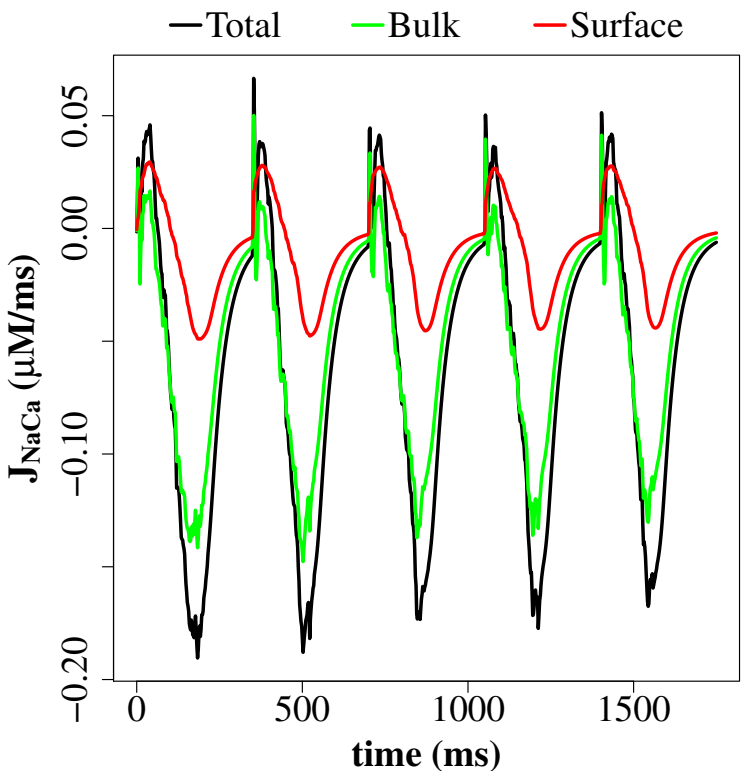

Figure 21: **NCX flux for five APs:** The total NXC flux (in black), the bulk NCX flux (in green) and the surface NCX flux (in red) are plotted with f_{NCX}^{low} set to 0.66 and f_{NCX}^{high} set to 72.0. The plot shows five APs with a simulation with a quarter of a z-disc.

5.2.4 Visualization of the NCX factor

The spatial distribution of the NCX factor (f_{NCX}) is shown in Figures 22 and 23 for a small and a large CRU, respectively, at the x-y plane. The center of the CRU and the boundary of the sphere are highlighted in white. Each square represents one finite element. The different colours of the elements represent the NCX flux J_{NCX} at resting state. The $[Ca^{2+}]_i$ was the same for all finite elements. Hence, the colour differences were generated only by the NCX factor. The highest J_{NCX} was visible at the center of a CRU (in blue) and it decreased towards the boundary of the CRU (in red). In the example with the large CRU (Figure 23), the center of this CRU lay almost at the center of an element, hence f_{NCX} was high for this element. In the case of the small CRU (Figure 22), the center was between two elements and their corresponding f_{NCX} was lower compared to the value at the center of the large CRU. Effectively, there were only four different values for f_{NCX} in the small CRU. Hence, the drop-off in a small CRU took place in large steps. In the large CRU the decay of the NCX factor was smoother. A higher grid resolution, and hence, smaller elements would allow a better resolution of the NCX distribution, but the computation time would increase significantly. Neighbouring CRUs are visible by the colour change in Figure 23.

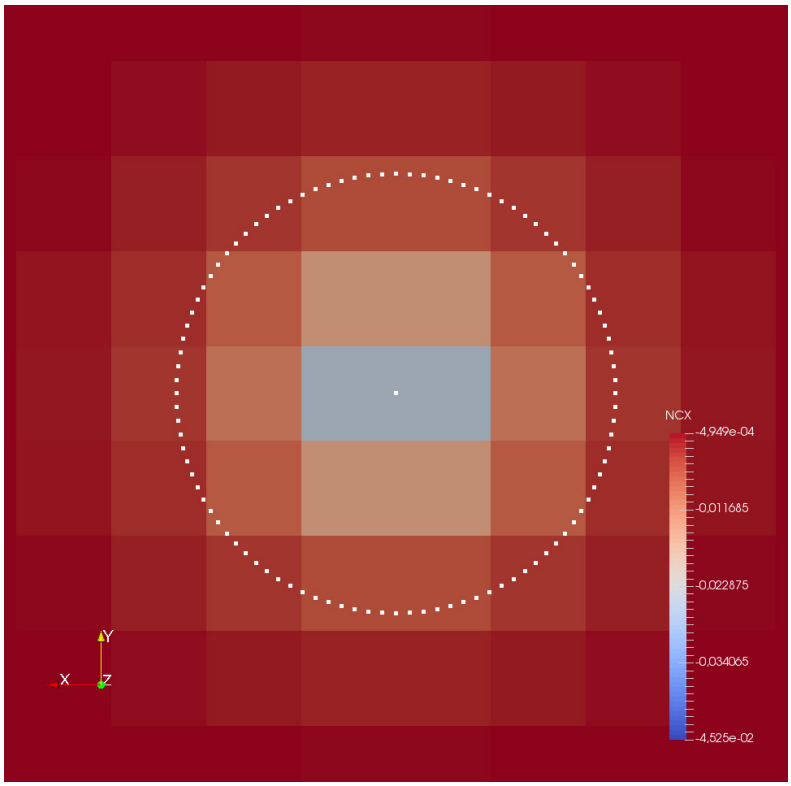

Figure 22: **Visualization of the NCX factor:** Small CRU with a radius of ∼0.114 µm.

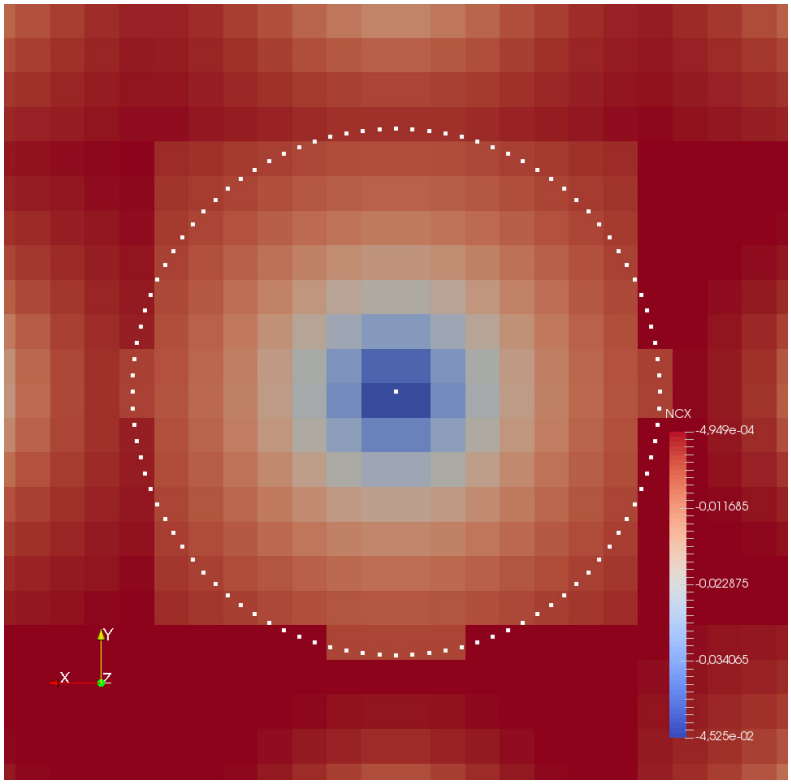

Figure 23: **Visualization of the NCX factor:** Large CRU with a radius of ∼0.379 µm.

5.3 Simulation results

We used the ODE of J_{NaCa} (Equation (45)) to become familiar with the behaviour of the NCX flux with different $[Na^+]_i$ and $[Ca^{2+}]_i$. Afterwards, we investigated the behaviour and the influence of NCX in our whole cell model. For this purpose, we ran simulations under three conditions: (1) the complete inhibition of NCX, (2) the original implementation with a homogeneous distribution of NCX, and (3) the new implementation with a heterogeneous distribution of NCX.

5.3.1 NCX flux

We calculated J_{NaCa} using $[Ca^{2+}]_i$, $[Na^+]_i$ and voltage membrane (V) as input parameters to investigate how much the NCX flux is dependent on these parameters and at which concentrations NCX switches from forward to reverse mode. We varied the membrane potential between -80 mV and +40 mV, which is the usual range of membrane potential values during an AP, with a $[Na^+]_i$ of 14.0 mM (value used by [6]) and calculated the corresponding J_{NaCa} (Figure 24). The $[Ca^{2+}]_i$ has been varied from 0.0 µM to 5.0 µM with 0.5 µM steps. The red line indicates the trace of J_{NaCa} during one AP using the original ODE-Mahajan model. Generally, the negative J_{NaCa} (forward mode) decreased with increasing membrane potential and then switched to reverse mode. The precise value of the membrane potential for the switch depended on the $[Ca^{2+}]_i$. With increasing $[Ca^{2+}]_i$ the switching point occurred later and NCX stayed in the forward mode despite positive membrane potential.

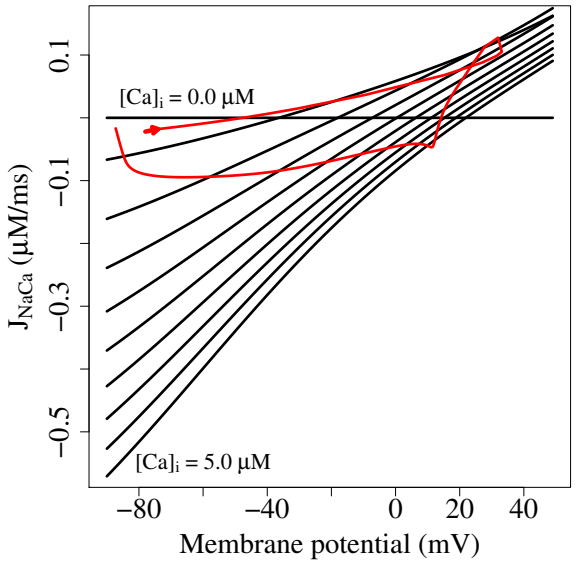

Figure 24: **NCX flux dependency on membrane potential (V):** Increasing $[Ca^{2+}]_i$ (black lines) over the usual range of membrane potential values and the trace of J_{NaCa} during one AP (red line) using the ODE-Mahajan model [6].

Next, we set the $[Ca^{2+}]_i$ to 0.5 µM in Figure 25 and to 5.0 µM in Figure 26. The J_{NaCa} was negative (forward mode) with a $[Ca^{2+}]_i$ of 0.5 µM, a low $[Na^+]_i$ between 2 mM and 8 mM, and negative membrane potential. With increasing $[Na^+]_i$ and membrane potential the negative J_{NaCa} decreased and then switched to the reverse mode. A similar behaviour

was observed with a $[Ca^{2+}]_i$ of 5.0 μM, which regulates NCX in the ODE-Mahajan model. NCX was in forward mode (Ca^{2+} outward flux) at -80 mV and was almost six-fold higher with a $[Ca^{2+}]_i$ of 5.0 μM than with a $[Ca^{2+}]_i$ of 0.5 μM. The NCX flux was positive only with very high $[Na^+]_i$ and positive membrane potential using a $[Ca^{2+}]_i$ of 5.0 μM.

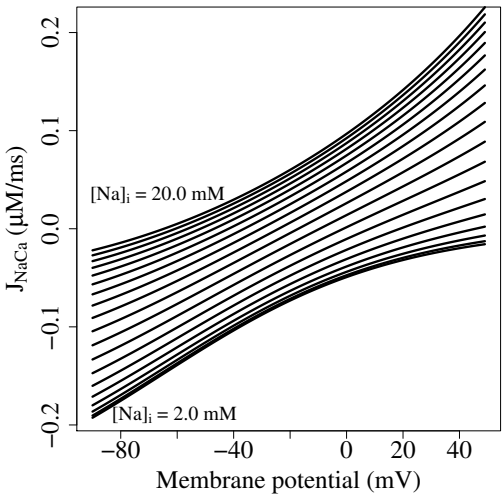

Figure 25: **NCX flux dependency on $[Na^+]_i$:** Increasing $[Na^+]_i$ (black lines) over the usual range of membrane potential values with $[Ca^{2+}]_i = 0.5$ μM.

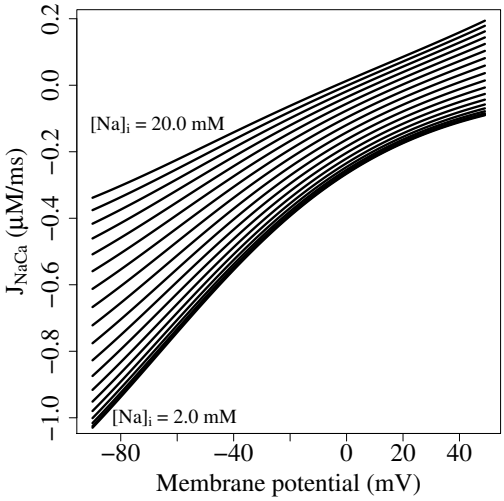

Figure 26: **NCX flux dependency on $[Na^+]_i$:** Increasing $[Na^+]_i$ (black lines) over the usual range of membrane potential values with $[Ca^{2+}]_i = 5.0$ μM.

5.3.2 Comparison of different NCX conditions

We ran simulations for five APs with a BCL of 350 ms and a quarter of a z-disc with 77 CRUs. In total, we simulated a time span of 1750 ms. The last three APs were used to determine the average of the key output variables: (1) APD_{90}, (2) minimum (resting) and maximum (peak) $[Ca^{2+}]_i$, (3) maximum RyR flux, (4) minimum and maximum nSR free $[Ca^{2+}]$, and (5) the depletion of the nSR free $[Ca^{2+}]$. We compared three NCX conditions: (1) the complete NCX inhibition, (2) the original NCX flux with a homogeneous distribution and (3) the NCX flux with the f_{NCX}^{low} set to 0.66 and f_{NCX}^{high} set to 72.0 were used (called heterogeneous NCX).
First, we ran a simulation with the complete NCX inhibition (Figure 27). The results of the key output variables are listed in Table A.8. The peak $[Ca^{2+}]_i$ of the second AP was higher than the peak $[Ca^{2+}]_i$ of the first AP and many RyRs opened during the diastole. This behaviour intensified with the subsequent APs. At the fifth AP the $[Ca^{2+}]_i$ reached physiologically unrealistic high values of $\sim$30 μM. There was a massive Ca^{2+} accumulation as NCX did not extrude any Ca^{2+} from the cell. Eventually, the nSR free $[Ca^{2+}]$ remained low, because most nSR Ca^{2+} was bound to buffers.
The following two simulations showed the results with homogeneous NCX and with heterogeneous NCX (Figures 28 and 29, respectively). The results of the key output variables are listed in Table A.8. The APD_{90} of both simulations were similar with a value of 192.4 ms and 192.6 ms, respectively. The nSR free $[Ca^{2+}]$, and hence, the depletion of nSR free $[Ca^{2+}]$ were almost unaffected using these two different NCX models. The peak $[Ca^{2+}]_i$ was considerably lower using the heterogeneous NCX model with a value of 1.84 μM compared to 2.48 μM. The time-to-peak of the $[Ca^{2+}]_i$ with heterogeneous NCX was lower with a value of 101.5 ms compared to 112.8 ms. The peak RyR flux was lower in the heterogeneous NCX model with a value of 2.16 μM/ms compared to 2.71 μM/ms. There were 0 sparks per diastole with the heterogeneous NCX distribution, but on average 1 spark per diastole with the homogeneous NCX distribution. The contribution of NCX to the overall Ca^{2+} removal was 24.2 % for the homogeneous NCX distribution and 21.2 % for the heterogeneous NCX distribution.

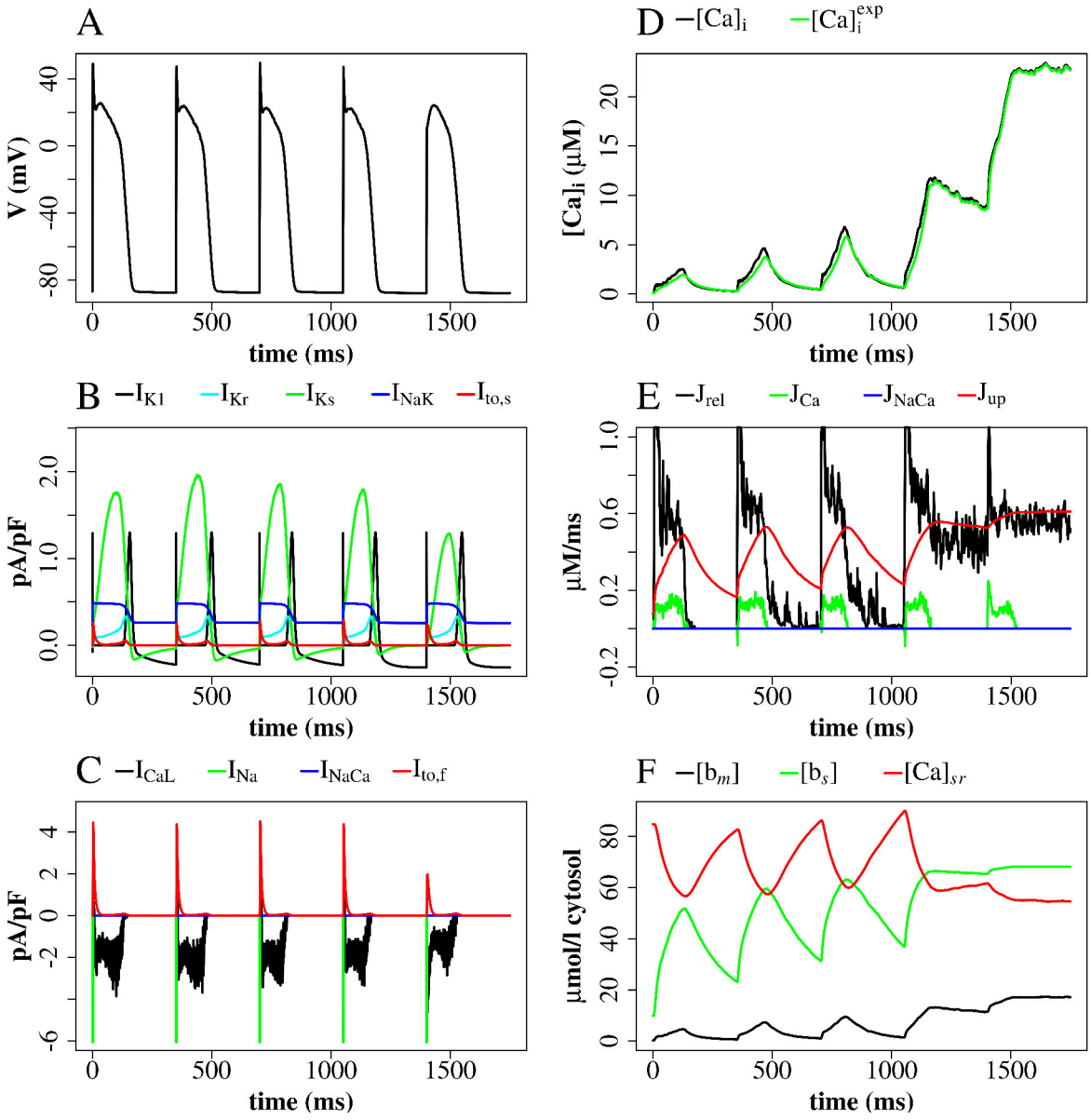

Figure 27: **Simulation with the complete NCX inhibition:** Membrane potential, ionic currents, and concentrations, a stimulus every 350th ms **(A)** - Membrane potential. **(B)** - Currents I_{K1}, I_{Kr}, I_{NaK}, and $I_{to,s}$. **(C)** - LCC current (I_{CaL}), Na^+/Ca^{2+}-exchanger current (I_{NaCa}), $I_{to,f}$, and I_{Na} (truncated). **(D)** - Average cytosolic $[Ca^{2+}]_i$ and $[Ca^{2+}]_i^{exp}$ as defined in Equation (25). **(E)** - Ca^{2+}-fluxes: J_{rel} (truncated), J_{Ca}, J_{NaCa}, J_{up}. **(F)** - Buffer-bound $[Ca^{2+}]_i$ ($[b_m]$, $[b_s]$) and nSR free $[Ca^{2+}]$ ($[Ca_{sr}]$) are plotted. $[b_m]$ and $[b_s]$ are in conventional concentrations in units of µM, whereas $[Ca_{sr}]$ is expressed for simplicity in units of µM ν_{sr}/ν_{cyt} (µmol/l cytosol). Plots show the first five APs of a simulation with a quarter of a z-disc.

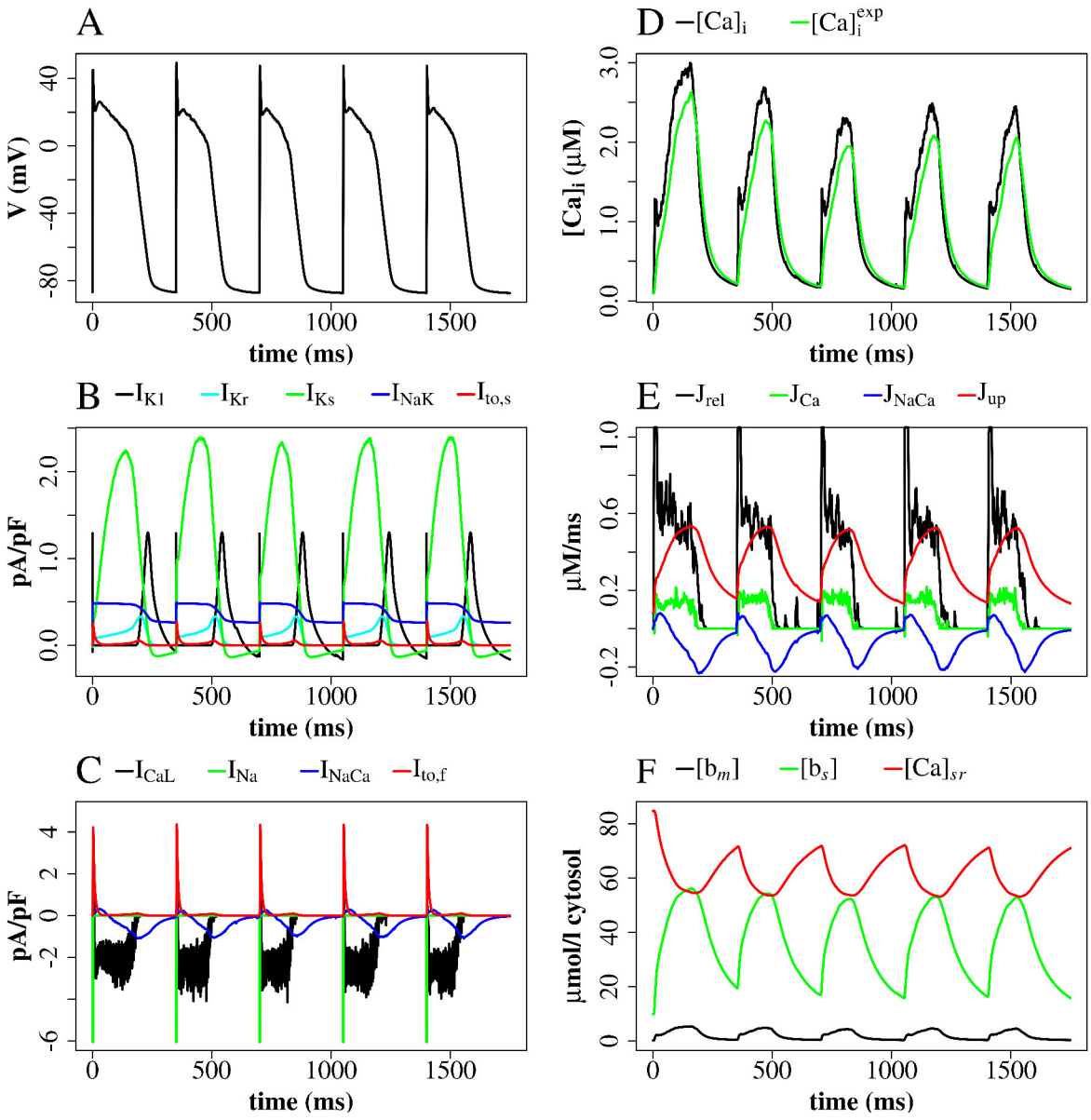

Figure 28: **Simulation with the homogeneous NCX distribution:** Membrane potential, ionic currents, and concentrations, a stimulus every 350th ms **(A)** - Membrane potential. **(B)** - Currents I_{K1}, I_{Kr}, I_{NaK}, I_{NaK}, and $I_{to,s}$. **(C)** - LCC current (I_{CaL}), Na^+/Ca^{2+}-exchanger current (I_{NaCa}), $I_{to,f}$, and I_{Na} (truncated). **(D)** - Average cytosolic $[Ca^{2+}]_i$ and $[Ca^{2+}]_i^{exp}$ as defined in Equation (25). **(E)** - Ca^{2+}-fluxes: J_{rel} (truncated), J_{Ca}, J_{NaCa}, J_{up}. **(F)** - Buffer-bound $[Ca^{2+}]_i$ ($[b_m]$, $[b_s]$) and nSR free $[Ca^{2+}]$ ($[Ca_{sr}]$) are plotted. $[b_m]$ and $[b_s]$ are in conventional concentrations in units of µM, whereas $[Ca_{sr}]$ is expressed for simplicity in units of µM ν_{sr}/ν_{cyt} (µmol/l cytosol). Plots show the first five APs of a simulation with a quarter of a z-disc.

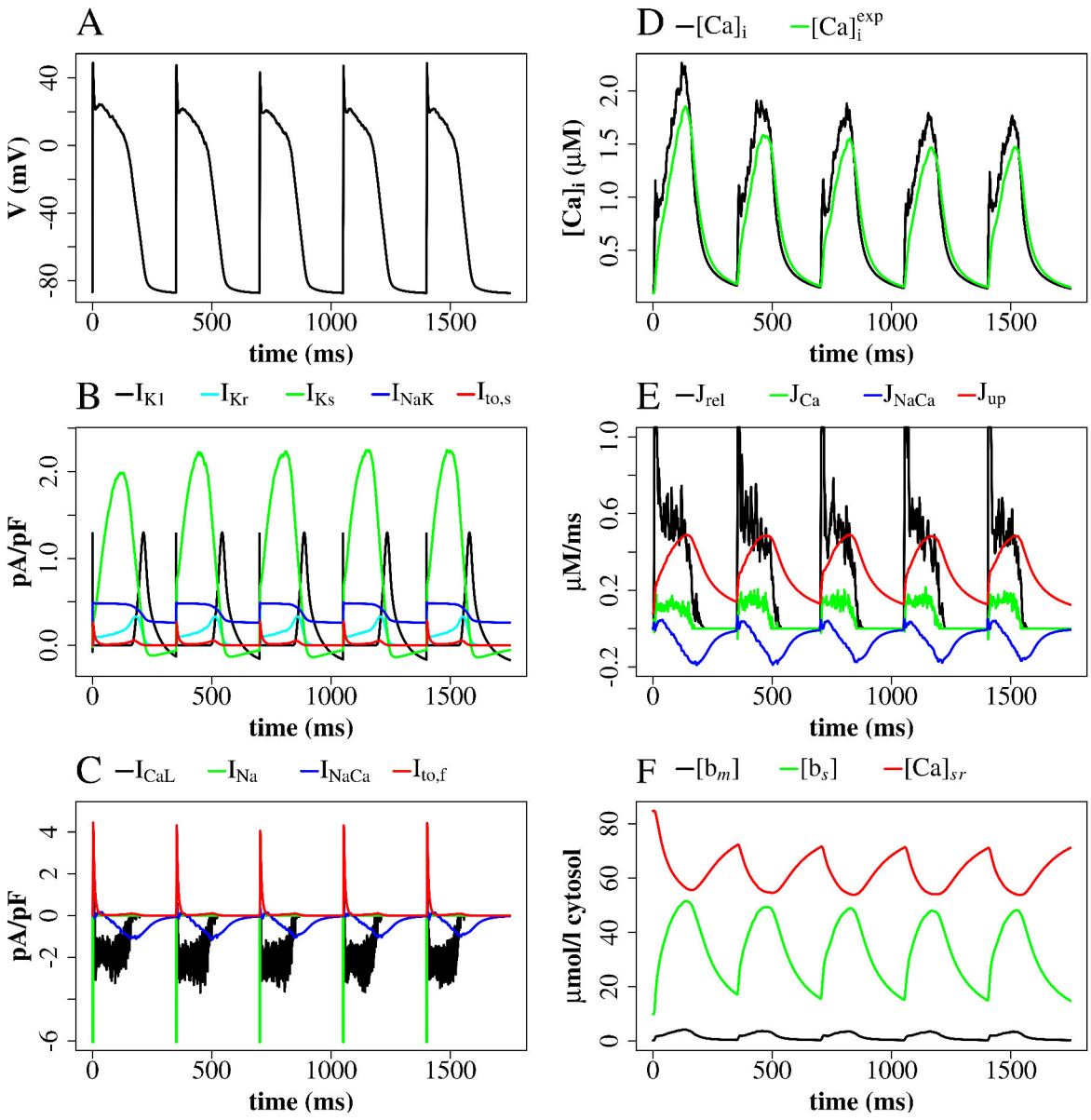

Figure 29: **Simulation with the heterogeneous NCX distribution:** Membrane potential, ionic currents, and concentrations, a stimulus every 350th ms **(A)** - Membrane potential. **(B)** - Currents I_{K1}, I_{Kr}, I_{NaK}, I_{NaK}, and $I_{to,s}$. **(C)** - LCC current (I_{CaL}), Na^+/Ca^{2+}-exchanger current (I_{NaCa}), $I_{to,f}$, and I_{Na} (truncated). **(D)** - Average cytosolic $[Ca^{2+}]_i$ and $[Ca^{2+}]_i^{exp}$ as defined in Equation (25). **(E)** - Ca^{2+}-fluxes: J_{rel} (truncated), J_{Ca}, J_{NaCa}, J_{up}. **(F)** - Buffer-bound $[Ca^{2+}]_i$ ($[b_m]$, $[b_s]$) and nSR free $[Ca^{2+}]$ ($[Ca_{sr}]$) are plotted. $[b_m]$ and $[b_s]$ are in conventional concentrations in units of µM, whereas $[Ca_{sr}]$ is expressed for simplicity in units of µM ν_{sr}/ν_{cyt} (µmol/l cytosol). Plots show the first five APs of a simulation with a quarter of a z-disc.

We reduced the LCC activity to 50 % to investigate the potential triggering role of NCX. The results are summarized in Table A.9. If NCX was completely inhibited, the $[Ca^{2+}]_i$ increased during five APs, but the Ca^{2+} cycling remained during these five APs with an APD_{90} of 115.3 ms. The peak $[Ca^{2+}]_i$ was 2.2 µM and the time-to-peak of $[Ca^{2+}]_i$ was 65.7 ms. The RyR flux had a peak value of 2.35 µM/ms and on average 4.75 sparks per diastole were observed. The Ca^{2+} depletion of the nSR was 15.9 %. APD_{90} with homogeneous NCX was reduced by ∼36.7 % from 192.4 ms to 121.8 ms. The peak $[Ca^{2+}]_i$ was considerably reduced by ∼60.1 % from 2.48 µM to 0.99 µM. Dual peaks in the $[Ca^{2+}]_i$ were observed. The time-to-peak of the principal peak was reduced by ∼50.8 % from 112.5 ms to 55.3 ms. The RyR flux had a lower peak value of 2.05 µM/ms compared to 2.71 µM/ms resulting in a reduction of ∼24.4 %. The average number of sparks per diastole was increased from 1.0 to 1.5. The Ca^{2+} depletion of the nSR was reduced from 14.6 % to 11.9 %.
Using heterogeneous NCX APD_{90} was reduced by ∼27.0 % from 192.6 ms to 140.6 ms compared to the normal LCC activity. The peak $[Ca^{2+}]_i$ was reduced by ∼44.6 % from 1.84 µM to 1.02 µM. The RyR flux had a lower peak value of 1.95 µM/ms compared to 2.16 µM/ms resulting in a reduction of ∼9.7 %. The average number of sparks per diastole was increased from 0 to 2.25. The Ca^{2+} depletion of the nSR was reduced from 21.3 % to 9.9 %.
Comparing both NCX models to the complete NCX inhibition under lower LCC activity condition showed that heterogeneous NCX had a longer APD_{90}, but $[Ca^{2+}]_i$, peak RyR flux, and the Ca^{2+} depletion of nSR were lower. The diastolic spark frequency was the lowest with 1.5 using homogeneous NCX.

5.3.3 Sodium concentration

In contrast to the $[Ca^{2+}]_i$, the $[Na^+]_i$ in our model is not spatially resolved, but represented by an ODE. The $[Na^+]_i$ was increased globally or locally to investigate its influence on NCX in our whole cell model using a quarter of a z-disc meaning 77 CRUs.
First, we increased the starting $[Na^+]_i$ from the original value of ∼10.42 mM to 15.42 mM and then to 20.42 mM (compare Table A.8 with Table A.10). The complete inhibition of NCX resulted in a quick accumulation of Ca^{2+} and after the third AP the $[Ca^{2+}]_i$ reached physiologically unrealistic high values. Eventually, nSR free $[Ca^{2+}]$ remained low, because most nSR Ca^{2+} was bound to buffers after the third AP.
For homogeneous NCX with a starting $[Na^+]_i$ of 15.42 mM, APD_{90} was reduced from 192.4 ms to 169.7 ms compared to the starting $[Na^+]_i$ of 10.42 mM. The peak $[Ca^{2+}]_i$ was increased with a value of 4.34 µM compared to 2.48 µM. The time-to-peak of the $[Ca^{2+}]_i$ was reduced from 112.5 ms to 97.04 ms. The RyR flux was marginally higher, but the spark frequency and the Ca^{2+} depletion of the nSR were increased. The $[Na^+]_i$ was reduced from 15.42 mM to ∼15.34 mM after four APs.
Increasing further the starting $[Na^+]_i$ from 15.42 mM to 20.42 mM with homogeneous NCX, APD_{90} and the time-to-peak of the $[Ca^{2+}]_i$ were slightly decreased. The peak $[Ca^{2+}]_i$ was considerably increased from 4.34 µM to 7.53 µM. The RyR flux was higher with a peak value of 3.37 µM/ms, but the spark frequency was reduced to 2.5 sparks per diastole. The Ca^{2+} depletion of the nSR was increased from 15.7 % to 18.0 %. The $[Na^+]_i$ was reduced from 20.42 mM to ∼20.27 mM after four APs.
Using heterogeneous NCX and increasing the starting $[Na^+]_i$ from 10.42 mM to 15.42 mM reduced APD_{90} from 192.6 ms to 180.2 ms. The peak $[Ca^{2+}]_i$ was increased from

1.84 μM to 3.83 μM. The time-to-peak of the $[Ca^{2+}]_i$ was almost unaffected. The RyR flux and the Ca^{2+} depletion of the nSR were marginally increased. The spark frequency was increased to 2.25 sparks per diastole. The $[Na^+]_i$ was decreased from 15.42 mM to ∼15.37 mM after four APs.
Increasing the starting $[Na^+]_i$ from 10.42 mM to 20.42 mM with heterogeneous NCX, reduced further APD_{90} to 161.6 ms. The peak $[Ca^{2+}]_i$ was considerably increased from 3.83 μM to 6.26 μM. The time-to-peak of the $[Ca^{2+}]_i$ was reduced to 87.0 ms. The RyR flux was higher with a peak value of 3.61 μM/ms and the spark frequency was slightly increased to 2.75 sparks per diastole. The Ca^{2+} depletion of the nSR was considerably increased from 9.9 % to 17.2 %. The $[Na^+]_i$ was decreased from 20.42 mM to ∼20.29 mM after four APs.
Increasing the local $[Na^+]_i$, which directly regulates homogeneous NCX, to 13.0 mM at the beginning of an AP reduced APD_{90} from 192.4 ms to 180.4 ms (compare Table A.8 with Table A.11). The peak $[Ca^{2+}]_i$ was considerably decreased from 2.48 μM to 1.03 μM. The time-to-peak of the $[Ca^{2+}]_i$ was increased from 112.5 ms to 136.6 ms. The RyR flux and the number of sparks per diastole were reduced. The Ca^{2+} depletion of the nSR was decreased from 14.6 % to 12.6 %. The $[Na^+]_i$ increased from 10.42 mM to ∼10.47 mM after four APs.
Increasing the local $[Na^+]_i$, which directly regulates heterogeneous NCX, to 13.0 mM at the beginning of an AP decreased APD_{90} from 192.6 ms to 183.6 ms. The peak $[Ca^{2+}]_i$ was decreased substantially from 1.84 μM to 0.72 μM. Dual peaks in the $[Ca^{2+}]_i$ were observed. The time-to-peak of the principal peak was 115.5 ms. The RyR flux and the number of sparks per diastole were considerably reduced. The Ca^{2+} depletion of the nSR was decreased from 14.0 % to 11.8 %. The $[Na^+]_i$ increased from 10.42 mM to ∼10.54 mM after four APs. Increasing the local $[Na^+]_i$ not only for NCX, but also for the Na^+/K^+ pump did not change the key output variables.
Increasing the local $[Na^+]_i$, which directly regulates homogeneous NCX, from 13.0 mM to 15.0 mM at the beginning of an AP marginally reduced APD_{90} and the peak $[Ca^{2+}]_i$. The RyR flux was reduced with a peak value of 0.75 μM/ms and 0.5 sparks per diastole were observed. The Ca^{2+} depletion of the nSR was almost unaffected. The $[Na^+]_i$ increased from 10.42 mM to ∼10.56 mM after four APs. Additionally, increasing the local $[Na^+]_i$ for the Na^+/K^+ pump did not change the output values noticeably.
Increasing the local $[Na^+]_i$, which directly regulates heterogeneous NCX, from 13.0 mM to 15.0 mM at the beginning of an AP increased APD_{90} from 183.6 ms to 209.88 ms. The peak $[Ca^{2+}]_i$ was marginally increased and dual peaks in the $[Ca^{2+}]_i$ were observed. The time-to-peak for the principal $[Ca^{2+}]_i$ peak was 128.8 ms. The RyR flux was marginally increased and 2.75 sparks per diastole were observed. The Ca^{2+} depletion of the nSR was almost unaffected. The $[Na^+]_i$ increased from 10.42 mM to ∼10.56 mM after four APs.
Running three simulations without APs for 10 s and with 320 CRUs, using complete NCX inhibition and with an increased starting $[Na^+]_i$ of 20.42 mM showed 17, 21, and 17 sparks with one long lasting spark known as metastable spark, respectively. Using homogeneous NCX there were 16, 26, and 28 sparks, respectively, and using the heterogeneous NCX condition, there were 17, 18, and 19 sparks, respectively. Complete inhibition of NCX reduced the $[Na^+]_i$ from 20.42 mM to ∼19.2 mM, but the $[Ca^{2+}]_i$ stayed constant. The $[Na^+]_i$ was reduced similarly with homogeneous and heterogeneous NCX conditions, whereas the $[Ca^{2+}]_i$ increased to 0.116 μM. The peak RyR flux was marginally reduced using heterogeneous NCX compared to the homogeneous NCX distribution and the complete NCX inhibition.

5.3.4 Spark analysis

The opening of a single RyR is called a quark [19], which can initiate further RyR openings resulting in a spark. It is not clearly defined how many RyRs must open for an event to be defined as a spark [19], but we consider an event as a spark if at least two RyRs open in one CRU. Simulations of 20 s (split into five individual simulations) without any stimulus were performed to study the influence of the NCX distribution on the spark behaviour. We simulated 320 CRUs of one z-disc, which represents 1.8 % of the cell assuming 17,600 CRUs in a whole cell [11, 17, 18, 19, 20]. The number of RyRs per cleft was set to a fixed value of 63 (which corresponds to the mean value in previous simulations). A fixed number of RyRs per CRU was used in these simulations to reduce CRU size bias, because the number of sparks depends strongly on the CRU size, for example simulations with only 10 RyRs/CRU showed no sparks at all during 3 s.
With the 63 RyRs/CRU setup we observed 33 sparks and four quarks during 20 s using the complete NCX inhibition. This is equivalent to 1.65 sparks/s for the cellular subvolume simulated and ∼93 sparks/s for the whole cardiac myocyte. One of these events was caused by a spontaneous LCC opening. Hence, there were 32 sparks out of 36 single RyR openings, which resulted in a coupling fidelity of 88.9 %. The simulations with homogeneous NCX showed 27 sparks and three quarks during 20 s. Hence, there were 1.35 sparks/s for the cellular subvolume simulated and 75 sparks/s for the whole cardiac myocyte. None of these events were caused by a LCC opening. There were 27 sparks out of 30 single RyR openings, which resulted in a coupling fidelity of 90.0 %. The simulations with heterogeneous NCX showed 38 sparks and six quarks during 20 s. There were 1.9 sparks/s for the cellular subvolume simulated and ∼106 sparks/s for the whole cardiac myocyte. One of the sparks was caused by a LCC opening. Hence, we had 37 sparks out of 43 single RyR openings and a coupling fidelity of 86.1 %.
We investigated 10 sparks for each NCX condition and determined the mean and the standard deviation (SD) of (1) the full duration at half maximum amplitude (FDHM), (2) the full width at half maximum amplitude (FWHM), and (3) the peak [Ca^{2+}] of the sparks. Note that we measured the peak Ca^{2+} in a CRU sphere, which is not directly comparable with the high c_{di} values given by Equation (21) for a plane. Quarks were not measured in our simulations as these are not measured in standard spark quantification confocal microscopy studies. The FDHM of the complete NCX inhibition was 1.57 ms (SD = 0.12 ms), the FWHM was 0.42 µm (SD = 0.01 µm), and peak [Ca^{2+}] was 35.14 µM (SD = 1.34 µM). The FDHM of homogeneous NCX was 1.54 ms (SD = 0.15 ms), the FWHM was 0.42µm (SD = 0.01 µm), and the peak $[Ca^{2+}]_i$ was 35.0 µM (SD = 1.7 µM). The FDHM of heterogeneous NCX was 1.46 ms (SD = 1.14 ms), the FWHM was 0.43 µm (SD = 0.0 µm), and the peak $[Ca^{2+}]_i$ was 33.23 µM (SD = 1.16 µM). The results of the FDHM, FWHM, and the peak $[Ca^{2+}]_i$ are shown in boxplots (Figures 30, 31, 32, respectively). The average values of homogeneous NCX ("Homogenous") for FDHM, FWHM, and peak [Ca^{2+}] were similar to the average values of the complete NCX inhibition ("No"), but the range of the FDHM and the peak [Ca^{2+}] values differed. However, the average FDHM and the peak [Ca^{2+}] of heterogeneous NCX were lower and the average FWHM was higher compared to the two other NCX conditions. A case study using a later version of our model (including parameter changes) showed the same trends (data not shown).

Figure 30: **Spark duration as FDHM:** Boxplots for complete NCX inhibition ("No", grey), for the homogeneous NCX distribution (in blue), and for the heterogeneous NCX distribution (in green).

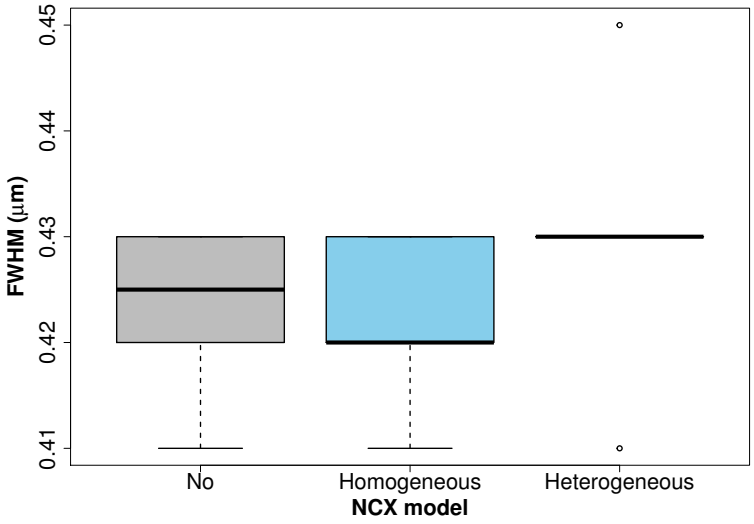

Figure 31: **Spark width as FWHM:** Boxplots for complete NCX inhibition ("No", in grey), for the homogeneous NCX distribution (in blue), and the heterogeneous NCX distribution (in green).

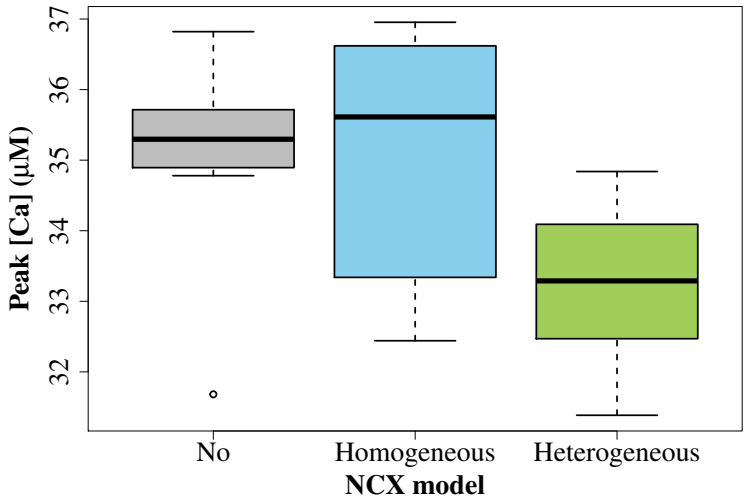

Figure 32: **Peak [Ca^{2+}] of the sparks:** Boxplots for complete NCX inhibition ("No", in grey), for the homogeneous NCX distribution (in blue), and the heterogeneous NCX distribution (in green).

5.4 The role of NCX

NCX is necessary for the rabbit ventricular myocyte to maintain physiological Ca^{2+} cycling according to our model. Using the complete NCX inhibition, the $[Ca^{2+}]_i$ increased to physiologically unrealistic high values and the nSR free $[Ca^{2+}]$ remained low, and hence, the depletion of nSR free Ca^{2+} was also low. NCX is responsible for 28 % of the Ca^{2+} removal in rabbits [171]. In our model NCX contributed with 21.2 % to the Ca^{2+} removal using heterogeneous NCX with f_{NCX}^{low} set to 0.66 and f_{NCX}^{high} set to 72.0. This value was lower than the literature value, but still much higher than a value of 7 % stated for rats [171]. Homogeneous NCX showed a higher contribution of 24.2 % to Ca^{2+} removal which was closer to the literature value.
Mice with a NCX knockout of 80 % - 90 % of the cells in the ventricle are able to survive due to physiological adaptations [202, 203]. Their LCC current was reduced and PMCA was mostly responsible for Ca^{2+} extrusion [203]. Reducing the LCC activity by 50 % in our simulation with complete NCX inhibition showed that the Ca^{2+} cycling was intact for five APs. Hence, reduced LCC activity stabilized the $[Ca^{2+}]_i$ during the complete NCX inhibition. However, the contribution of NCX to Ca^{2+} removal is lower in mice than in rabbits [171]. Our model suggests that a functional NCX is necessary for the rabbit ventricular myocyte to maintain Ca^{2+} cycling, otherwise too much Ca^{2+} is accumulated. This process could not yet been verified in experimental approaches because a complete inhibition of NCX has not yet been achieved due to the lack of potent and highly specific inhibitors [170]. However, we did not model neither a PMCA current nor a background Ca^{2+} current, which could extrude more Ca^{2+}, nor did we model the mitochondria. All three of them might have reduced the Ca^{2+} accumulation.

Microdomains We investigated the influence of the parameters $[Ca^{2+}]_i$, $[Na^+]_i$ and membrane potential (V) using Equation (45) for J_{NaCa}. J_{NaCa} increased almost linearly

with increasing membrane potential. J_{NaCa} was zero, when the $[Ca^{2+}]_i$ was zero. With increasing $[Ca^{2+}]_i$, J_{NaCa} became more negative. Hence, J_{NaCa} depends strongly on local $[Ca^{2+}]_i$ and $[Na^+]_i$. The ionic concentrations determine the turning point of the mode switch and the strength of J_{NaCa}. However, in experimental approaches it was not yet possible to measure the actual $[Ca^{2+}]$ and $[Na^+]$ which regulate NCX *in vivo*. The effective ionic concentrations could be much higher as their known average values in cardiac myocytes. We demonstrated with our whole cell model that inside the CRUs there are steep Ca^{2+} gradients with high local $[Ca^{2+}]$ (see Chapter 3.3.2). These high $[Ca^{2+}]$ are reached in single CRUs before the total $[Ca^{2+}]_i$ reaches its maximum value. The same behaviour was assumed for the local $[Na^+]_i$, but, in contrast to Ca^{2+}, Na^+ in our model was not spatially resolved. It is difficult to compare the behaviour of our NCX flux to the one in the ODE-Mahajan model, because many parameters differ in addition to the feature of our model that NCX is regulated by the local $[Ca^{2+}]_i$. The J_{NaCa} from our model switched later to forward mode during AP, which was unexpected because of the higher local $[Ca^{2+}]_i$. Weber et al. (2002) [118] estimated the submembrane $[Ca^{2+}]$ to peak within 32 ms.
Increasing the starting $[Na^+]_i$ to 15.42 mM or even 20.42 mM using homogeneous NCX had dramatic effects as it increased the $[Ca^{2+}]_i$ to physiologically unrealistic high values and reduced APD_{90} to 169.7 ms, which was too low. APD_{90} is ∼185 ms at a BCL of 350 ms for rabbits [147, 148]. The $[Ca^{2+}]_i$ was considerably reduced by introducing a locally higher $[Na^+]_i$ for heterogeneous NCX at the beginning of an AP. However, it caused dual peaks in $[Ca^{2+}]_i$, which has not been observed in experimental approaches and was therefore not anticipated in our simulation results. This effect was less pronounced with homogeneous NCX. Using only marginally higher local $[Na^+]_i$ of 13.0 mM with heterogeneous NCX still showed dual peaks in $[Ca^{2+}]_i$. However, a higher $[Na^+]$ for NCX at the beginning of an AP helped to reduce the peak $[Ca^{2+}]_i$ to a physiologically more realistic value.
J_{NaCa} has to be in forward mode to extrude Ca^{2+}, which can only be achieved with low $[Ca^{2+}]_i$ and/or high $[Na^+]_i$ during AP upstroke. Overall, we support the hypothesis of locally high $[Ca^{2+}]_i$ domains, but we could not show that a higher $[Na^+]_i$, either locally or globally, increased the Ca^{2+} efflux by NCX without undesirable side effects, such as considerable reduction of APD_{90} and Ca^{2+} accumulation. Further parameter fitting or inclusion of the PMCA current and/or a background Ca^{2+} current could prevent the Ca^{2+} accumulation.

Distribution In our model NCX is regulated by the local $[Ca^{2+}]_i$, which is already an improvement to the submembrane $[Ca^{2+}]$ of the ODE-Mahajan model. Nevertheless, we aimed to improve the model further by changing its distribution according to experiments. The main source were the results by Jayasinghe et al.[124], which are unfortunately for rat and the periphery of the cell, but other experiments also supported the hypothesis of a higher NCX concentration in the t-tubules [178, 200] and an accumulation in the CRUs [179, 180, 43]. We therefore introduced the heterogeneous NCX modelling approach representing a higher NCX distribution inside and near the CRUs. The heterogeneous NCX implementation showed marginally better results as the peak $[Ca^{2+}]_i$ was lower and therefore closer to the literature value. Moreover, the number of sparks per diastole was as low as anticipated and the time-to-peak of the $[Ca^{2+}]_i$ was lower compared to homogeneous NCX, and hence, closer to physiologically realistic values of ∼50 ms [204] or of 81 ms [118]. At the same time key feature, such as APD_{90} and SR Ca^{2+} dynamics,

were almost unaffected by the heterogeneous NCX implementation. The contribution to Ca^{2+} removal was marginally too low. The improved results by heterogeneous NCX supports the idea of a higher NCX density inside the CRUs and co-localization with RyRs.

Triggering We reduced the LCC activity to 50 % to examine a potential role of NCX as a backup way for Ca^{2+} influx at the beginning of an AP. The overall effect of reducing the LCC activity was a reduction of APD_{90}, the peak $[Ca^{2+}]_i$, the time-to-peak of the $[Ca^{2+}]_i$, the peak RyR flux, and the Ca^{2+} depletion of the nSR, which were expected as less Ca^{2+} entered the cell, whereas the spark frequency was increased. Theses reductions were smaller for heterogeneous NCX compared to homogeneous NCX indicating that heterogeneous NCX with a higher density at the center of the CRUs brought in more Ca^{2+} to balance out the reduced Ca^{2+} influx by the LCCs. However, the values of the key output variables of homogeneous and heterogeneous NCX were similar and the triggering effect of NCX was only visible by the prolonged APD_{90} of heterogeneous NCX and by the less reduction of the output variables compared to the 100 % LCC activity. Hence, our model showed that NCX works as an alternative or backup way for Ca^{2+} influx by triggering RyRs, if the LCCs fail. Other distributions of NCX are possible and were tested by Chu et al. (2016) [43] who used different ratios of NCX inside the dyadic cleft and in the CRU periphery. They showed also that NCX contributed to trigger the RyRs [43].

Sparks The simulation with the complete NCX inhibition for five APs showed 0 sparks during the first diastole, but then an increasing number of sparks per diastole and eventually the RyR openings were not terminated. This behaviour was caused by a massive increase of the $[Ca^{2+}]_i$. Using homogeneous NCX there were on average 1 spark per diastole, which was too high for a setup of 77 CRUs. Simulations with heterogeneous NCX showed 0 sparks per diastole, which was anticipated for such a small CRU setup. We demonstrated that the NCX activity is necessary to prevent too many sparks per diastole and an accumulation of the $[Ca^{2+}]_i$ during pacing, which might lead to spontaneous APs and disrupt the physiological Ca^{2+} cycling.
Running simulations without stimuli and with 320 CRU assuming to represent 1.8 % of a whole cell should show $\sim$2.0 sparks/s considering the literature value for spontaneous spark rate of 100 sparks/s for a whole cardiac myocyte with assumed 10,000 RyRs [19]. The spark frequencies were too low with complete NCX inhibition and homogeneous NCX with values of 1.65 sparks/s and 1.35 sparks/s, respectively. The spark frequency was the closest to the literature value using heterogeneous NCX with a value of 1.9 sparks/s. Experimental [205, 180, 193, 134] and modelling approaches [43] demonstrated that NCX-mediated Ca^{2+} extrusion lowers the spark frequency, the spark duration, the spark amplitude, and the coupling fidelity. We therefore expected heterogeneous NCX to reduce the spark frequency compared to the complete NCX inhibition and the homogeneous NCX, yet the opposite was true. Moreover, homogeneous NCX showed too many sparks during pacing and too few sparks without pacing, which was unexpected. The coupling fidelity was in the range of the literature value of 82 % - 96 % [195] for all three NCX conditions. The coupling fidelity, the spark amplitude (measured as the peak $[Ca^{2+}]_i$ of a spark), and the spark duration (FDHM) were marginally lower with heterogeneous NCX, which was in accordance with the results of another modelling approach [43]. The spark width (FWHM) was marginally higher with heterogeneous NCX.

5.5 Conclusions

We conclude that NCX is necessary for the rabbit ventricular myocyte to maintain physiological Ca^{2+} cycling according to our whole cell model. The strong dependency of NCX on the $[Ca^{2+}]_i$ and the $[Na^+]_i$ supported the idea that NCX might be regulated by locally high ion concentrations. In our model NCX is regulated by spatially resolved, and hence, locally high $[Ca^{2+}]_i$, which is an improvement to many other models that have only an average $[Ca^{2+}]_i$ or submembrane $[Ca^{2+}]$. However, increasing the local $[Na^+]_i$, which directly regulates NCX, caused undesired side effects. Including a PMCA current, a background Ca^{2+} current, a spatially resolved $[Na^+]_i$, and/or fitting the kinetic parameters of NCX may attenuate these side effects. The available system resource only allowed simulations of three NCX conditions for a total of 20 s, respectively. We cannot exclude the possibility that another distribution of NCX might have produced physiologically more realistic results. Chu et al. (2016) [43] propose a NCX distribution of a ratio of about 1:2 of dyad-to-periphery which reproduced spark behaviour reported by experimental approaches. It is challenging to cross-compare models with each other and with experiments, and to decide if Ca^{2+} cycling properties are superior or inferior. Each model has its own NCX implementation using different assumptions, experimental designs vary between studies, and Ca^{2+} cycling properties are species-dependent. Nevertheless, the heterogeneous NCX distribution showed more physiological Ca^{2+} cycling than the homogeneous NCX distribution in that it produced a physiologically more realistic peak $[Ca^{2+}]_i$, spark frequency and time-to-peak of a spark. The J_{NaCa} of heterogeneous NCX turned to negative earlier compared to homogeneous NCX, but still too late compared to the profile of the J_{NaCa} by Mahajan et al. (2008) [6]. Moreover, we showed that NCX contributes to trigger RyRs, but this effect was minor, which is supported by experimental evidence [190, 191, 192, 185]. Notably, NCX in our model is not part of the CRU model. Hence, in our model NCX is not directly regulated by a $[Ca^{2+}]$ of few hundreds of µM, but only by the $[Ca^{2+}]$ increase in the modelled sphere of a CRU with $[Ca^{2+}]$ of ∼30 µM - 40 µM. We cannot rule out that the triggering effect would be even stronger with NCX incorporated within each CRU model. Additionally, modelling NCX as individual stochastically gated channels (in the manner of LCCs and RyRs) might reveal further details about its kinetics. Overall, heterogeneous NCX marginally reduced the spark duration, the coupling fidelity, and the peak $[Ca^{2+}]$ of the sparks without influencing the spark width. These results were in accordance with the modelling results by Chu et al. (2016) [43]. Moreover, their proposed "dual-role hypothesis" was supported by our simulation results to such a degree as NCX contributed to trigger RyRs during systole and reduced the number of sparks during diastole, which prevents regenerative Ca^{2+} release events. The detailed examination of the performance of the three NCX conditions was limited by the long running time of the current version of our model and not enough simulation time was available in all cases for a thorough statistical analysis. Note that the spark durations with this version of our model were too short. An experimentally measured spark lasts ∼20 ms - 30 ms with an upstroke time of 10 ms [19, 206, 207, 208], whereas our simulated sparks peaked within 1 ms and lasted 12 ms - 18 ms, which were only partly dependent on CRU size. We used the $[Ca^{2+}]_i$ instead of the $[Ca^{2+}]$ determined by the Fluo-4 ($[Ca^{2+}]_i^{exp}$) for our analyses and we did not use a point-spread function to simulate the optical error of confocal microscopy measurements. A process of further parametrization may result in spark durations closer to experimental properties, particularly focussing on the RyR and buffer parameters.

6 Modelling and investigation of mitochondria

6.1 Introduction

In our whole cell model we set the height of RyRs to 6.0 nm representing the assumed location of the Ca^{2+} binding sites. We improved the calculation of the bulk $[Ca^{2+}]$ (c_{bulk}) as described in Chapter 2.4.4 and we altered the calculation of the jSR volumes for each corresponding CRU depending on its size as described in Chapter 2.4.5. The stochastic time stepping scheme was replaced by a deterministic time stepping scheme as mentioned in Chapter 2.7 for speedup.
In this chapter we want to incorporate a whole compartment to our model: the mitochondrion. The mitochondria are a Ca^{2+}-buffer space and might influence the CICR. Moreover, it supplies the ATP for the cell. We therefore combine an existing mitochondria model with the ODE-Mahajan model and investigate the Ca^{2+} channels of the mitochondria. The aim is to understand the influence of the mitochondria on Ca^{2+} dynamics using our whole cell approach.

6.1.1 Mitochondria

Mitochondria are double-membrane organelles, which can be found in almost all cell types of eukaryotic organisms [209]. They are between 0.5 µm and 1.5 µm in diameter in cardiac myocytes [210, 211], but they exhibit different sizes and structures. Initially, they were considered as spheres, but usually they form a highly ordered and dynamic network by fusion and fission [212, 213]. Cardiac mitochondria show spatially distinct subpopulations with different shapes: subsarcolemmal mitochondria, interfibrillar mitochondria, and perinuclear mitochondria [214]. Mitochondria have their own independent genome, the mitochondrial DNA [215]. Their main function is the production of adenosin triphosphate (ATP), and hence, the supply of chemical energy for the cell.

6.1.2 Structure and physiological relevance of mitochondria

Mitochondria are composed of five zones: (1) the outer mitochondrial membrane (OMM), (2) the intermembrane space (IMS), (3) the inner mitochondrial membrane (IMM) with many invaginations called (4) cristae, and (5) the matrix [215]. The OMM as outer barrier of the mitochondrion is freely permeable to molecules up to 5 kDa via the voltage-dependent anion channels (VDAC) [216], which switch from an anion-selective high-conductance state to a cation-selective low-conductance state dependent on voltage [217]. The concentrations of ions and small sugars of the IMS are similar to the cytosolic concentrations [215]. In contrast to the OMM, the IMM is highly impermeable and contains many membrane transporters and exchangers [215]. This selectivity for ions generates the mitochondrial outer membrane potential (OMP) and an inner membrane potential (IMP or $\Delta\Psi_m$). If IMP is -180 mV (negative with respect to the cytoplasm), the mitochondrion is called polarized [11], which drives ATP synthesis. If the mitochondrion is depolarized, meaning at 0 mV, it consumes ATP [11]. The location of ATP production and the tricarboxylic acid (TCA) cycle is the matrix, the inner compartment of the mitochondria [11].
The principal source for energy in form of ATP in some animal cells are the oxidative breakdown of carbohydrates and fatty acids [218]. Glucose is converted to pyruvate in the cyotsol and then transported to the mitochondria by IMM pyruvate carriers [219]. There

it is oxidized to acetyl coenzyme A and then to CO_2, which yields ATP via the TCA cycle. Fatty acids are oxidized in a similar manner. The oxidation of acetyl coenzyme A involves the reduction of nicotinamide adenine dinucleotide (NAD^+) to NADH and flavin adenine dinucleotide (FAD) to $FADH_2$. Their high-energy electrons are used in electron transfer reactions to drive ATP synthesis in the IMM. This process is called oxidative phosphorylation. The adenosin diphsophate (ADP) for the ATP synthesis is supplied by the adenine nucleotide translocator (ANT).
In cardiac cells, up to 95 % of the ATP formation is generated by the mitochondria [220]. The mitochondria, as the dominant ATP source, are essential for the function of the cardiac myocytes. Because of their high energy demand, cardiac myocytes have the highest mitochondria density of all cell types with up to 35 % and a number of 7000 [11, 221, 222]. The interfibrillar mitochondria are located along the sarcomeres between the z-discs [45]. They are rod-shaped and uniform in size [45]. The ends of interfibrillar mitochondria are near the dyadic clefts and therefore the Ca^{2+} channels of the mitochondria may be regulated by locally high $[Ca^{2+}]_i$ [45, 46]. Subsarcolemmal and perinuclear mitochondria are more diverse in shape and size [45]. Imaging techniques showed that smaller animals with higher heart rates, such as rats and mice, have more mitochondria between the z-lines than larger animals with lower heart rates, such as rabbits and humans [222].

6.1.3 Ca^{2+} cycling in mitochondria

Ca^{2+} uptake and release of the mitochondria is important for energy production [46] and can initiate cell death by activating the permeability transition pore [223]. Ca^{2+} addition activates the oxidative phosphorylation and provides NADH and ATP for contractile activation and ion transport, but a massive Ca^{2+} influx can lead to apoptotic cell death [223]. The main channels for the Ca^{2+} transport across the mitochondrion membrane are mitochondrial Na^+/Ca^{2+}-exchanger (effectively a $Na^+/Li^+/Ca^{2+}$-exchanger, and hence, abbreviated NCLX [224]), the mitochondrial calcium uniporter (MCU), and the voltage-dependent anion channel (VDAC).

Mitochondrial sodium-calcium exchanger (NCLX) NCLX has a similar structure as the other members of the Na^+/Ca^{2+}-exchanger superfamily: two transmembrane domains bind the ions and translocate them [225]. Hence, the mechanism of ion translocation is thought to be sequential and similar to the mechanism of the sarcolemmal NCX [225]. The K_m values for $[Na^+]_i$ and the $[Ca^{2+}]_i$ are $\sim$8 mM and $\sim$13 µM, respectively, but might be influenced by fluctuations in IMP [225]. The dependency on $[Na^+]_i$ and the stoichiometry of NCLX are not resolved [225]. Such unknown biophysical features of NCLX are due to its recent identification, the difference of ion selectivity and its difficult access in its native environment [225].

Mitochondrial uniporter (MCU) MCU is the pore-forming subunit of the uniporter holocomplex, which is a highly selective ion channel of the IMM [226]. The half-maximal activation (K_d) of MCU is in the upper micromolar or even millimolar range [227]. Hence, the Ca^{2+} influx is small under physiological conditions [46]. The EF-hand Ca^{2+}-binding proteins MICU1 and MICU2 are located in the intermembrane space of the MCU and are hypothesised to be regulated by the cytosolic $[Ca^{2+}]$ [226]. The architecture of MCU has been characterized recently, but details about Ca^{2+}-binding, transport, and exit are unknown [226].

Voltage-dependent anion channel (VDAC) The main channel of the OMM is VDAC. It regulates the influx of carbon substrates, phosphates, and cations [228], it adapts to changing conditions and is involved in apoptosis [216]. There are three isoforms (VDAC1 - 3) of which VDAC1 is the most highly expressed [228]. Its open and high conducting state is associated with enhanced influx of metabolites up to 5 kDa, for example ADP and ATP. The closed state involves a reduction in the conductivity by 50 % - 60 %. With its smaller channel pore it becomes a barrier for ADP and ATP, but this closed state favours cations, for example Ca^{2+} [216]. Cytosolic proteins, such as hexokinases and tubulin, can bind to VDAC, but little is known with respect to how VDAC is regulated or fulfils its functions [229]. Mitoplasts are treated mitochondria without OMM containing VDAC [230] and often used for patch-clamp studies. Hence, VDAC is often not investigated in experimental approaches [231].

6.1.4 Models of mitochondria

The central role of mitochondria as energy supplier and potential Ca^{2+}-buffer has led to the evolution of many diverse models with different foci. A coarse classification subdivides them into models of glycolysis (enzymatic models, lumped and kinetic models), models of the TCA cycle (flux balance and metabolic control models), hybrid models, models of oxidative phosphorylation and electron transport, models of F_1F_0-ATPase, and shuttle models (see review [232]). An example for a hybrid model is the work of Magnus and Keizer (1997) [106] modelling a mitochondrion of a pancreatic β-cell including Ca^{2+} dynamics, flux via the ANT, oxidative phosphorylation, and ATP production. A model of the outer membrane potential generation by VDAC was created by Lemeshko (2000) [233], but this model is not time-dependent. The model by Cortassa et al. (2003) [74] is an extension of the Magnus and Keizer model [106]. The model considers the energy metabolism (TCA cycle, oxidative phosphorylation) and Ca^{2+} dynamics (MCU, NCLX) of a cardiac mitochondrion and was later used by Hatano et al. (2011) [80] in a whole cell model. It reproduces NADH production of a rat heart trabulucae [74]. Beard (2005) [234] generated a model for the mitochondrial respiratory chain without the TCA cycle. A more detailed model was presented by Wu et al. (2007) [235] including the TCA cycle, but the Ca^{2+} dynamics were missing. The model by Yang et al. (2010) [236] focused on the depolarization of the mitochondrial membrane potential and the role of reactive oxygen species.

6.1.5 Controversies in mitochondria cardiac physiology

The role of mitochondria as a dynamic Ca^{2+}-buffer is controversial [237, 46, 225, 227] and its importance in this role depends on its actual capacity for Ca^{2+} influx. The Ca^{2+} influx into the mitochondria has to be high to work as an effective buffer over the time scale of a single heart beat. The mitochondria could also work as a long-term buffer over multiple beats, functioning to prevent Ca^{2+} accumulation in the cytosol. In either case, the mitochondria sense the rise and fall of the $[Ca^{2+}]_i$ with every heart beat [46], which is thought to be necessary for the mitochondria to match energy supply to varying energy demands, which are in turn influenced by Ca^{2+} [227]. Interfibrillar mitochondria are located near the CRUs with a distance of $\sim$50 µm - 100 µm, and hence, their Ca^{2+} channels might be regulated by a locally high, but brief $[Ca^{2+}]_i$ of 10 µM - 20 µM [45, 46]. Moreover, the mitochondria are close to the SR and are tethered to them [238]. Hence, they could create a microdomain with locally high $[Ca^{2+}]_i$ [227]. If MCU is regulated

by such locally high $[Ca^{2+}]$, a locally high Ca^{2+} influx is possible, even though the Ca^{2+} sensitivity of MCU is assumed to be low [37]. However, combining different experimental results, the total MCU flux seems to contribute only ∼1 % to the $[Ca^{2+}]_i$ removal systems (SERCA, NCX) [171, 46]. This holds for small as well as for large species [46]. The contribution of the mitochondria to the Ca^{2+} removal increases with increasing $[Ca^{2+}]_i$ up to ∼20 % at a $[Ca^{2+}]_i$ of 20 µM and the mitochondria might accumulate Ca^{2+} at higher heart rate [46].
If it is assumed that MCU is the only or the most important means of Ca^{2+} influx and NCLX the only means of Ca^{2+} efflux, then it follows that both must be equal under steady state conditions [225]. Relatively little is known about these two channels, but it is worthwhile to consider their dynamics in conjunction. Furthermore, VDAC is reported to have different subconductance states [239], but their role and importance in the Ca^{2+} dynamics is not yet clear. The aim is to investigate these three channels and to find channel models such that the mitochondria model fit into the ODE-Mahajan model and then into our whole cell model.

6.2 Modelling of mitochondria

We used the mitochondria ODE model of a pancreatic β-cell developed by Magnus and Keizer (1997) [106]. The main equations and the model description are given in Chapter 2.5. The corresponding parameters are listed in the Tables A.12 and A.13. The parameters of the whole cell model were not changed compared to the previous Chapter 5 and are listed in the Tables Tables A.1 to A.5.

6.2.1 Mitochondria model and ODE electrophysiology model

We implemented in C++ the full minimal model of a phosphorylating mitochondria by Magnus and Keizer (1997) and we combined it with the ODE-Mahajan model. The Ca^{2+} fluxes of the mitochondria depend on the $[Ca^{2+}]_i$ and the $[Na^+]_i$ of the ODE-Mahajan model, with Ca^{2+} extruded from the mitochondria adding to the $[Ca^{2+}]_i$. We converted the parameter values given in nmol mg^{-1} protein to mM using a conversion factor of 0.125 (for details see [74]). The mitochondrial volume (ν_{mito}) was set to 35 %. We investigated four different models for the NCLX: (1) the original model by Magnus and Keizer [106] ("Magnus"), (2) the model by Cortassa et al. (2006) [74] who introduced a dependency of $[Ca^{2+}]_i$ to the Magnus model ("Cortassa"), (3) the NCX model used by Mahajan et al. (2008) [6] adapted to mitochondria by us ("Mahajan"), and (4) the model by Dash and Beard (2008) [4] ("Dash"). We used the Dash NCLX model with a stoichiometry of 3:1, which was reported to show more physiologically behaviour than the 2:1 model [4]. Afterwards, we compared three MCU models: (1) the original model by Magnus and Keizer (1997) [106] ("Magnus"), (2) the model by Nguyen and Jafri (2007) [5] ("Nguyen"), and (3) the model by Dash and Beard (2008) [4] ("Dash"). The parameters for the Ca^{2+} channel models by Magnus and Keizer (1997) [106] are listed in Table A.13. The equations and parameters of the other models can be found in the corresponding studies. We changed the V_{max} values of the different NCLX and MCU models, respectively, till an equal steady state $[Ca^{2+}]_{mito}$ for all Ca^{2+} channel models was achieved to allow their comparison (Table A.14). We changed the parameters of the Mahajan NCX model to adjust for the $[Na^+]$ and the $[Ca^{2+}]$ of the mitochondria and the cytosol, respectively. The parameter $K_{m,Cao}$ was reduced from 1.3 mM to 0.72 mM,

$K_{m,Nao}$ was reduced from 87.5 mM to 5.14 mM, $K_{m,Nai}$ was reduced from 12.3 mM to 4.39 mM, and $K_{m,Cai}$ was reduced from 3.6 10^{-3} mM to 3.6 10^{-5} mM. The last two values are lower than suggested by Boyman et al. (2013) [225], but suit the literature values of ion concentrations in the mitochondria.

6.2.2 Mitochondria model in the whole cell model

The mitochondria model by Magnus and Keizer (1997) [106] with the MCU and NCLX model by Dash and Beard (2008) [4] was included in our whole cell model as described in Chapter 2.5. An overview of the spatial implementation of the x-y plane is shown in Figure 33. The mitochondria domain is indicated by red, the overlap region is indicated in white, and the blue area represents the cytosol. We simulated one z-disc with 120 half mitochondria each with a size of 0.65 × 0.65 × 0.65 µm including the overlap region. In total they occupied ∼24.8 % of the cell volume.

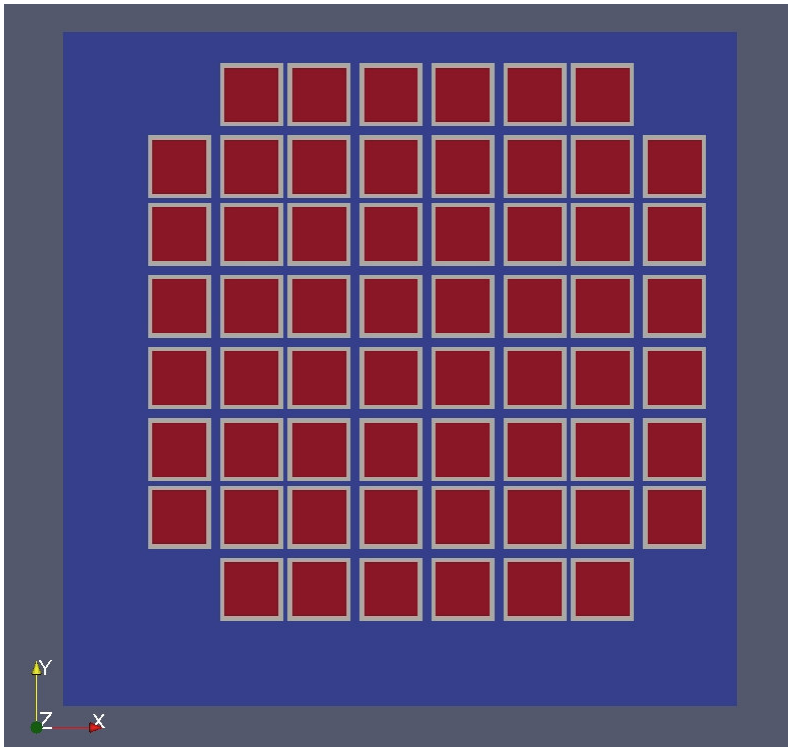

Figure 33: **An overview of mitochondria placement in our whole cell model:** A quarter of one z-disc with 60 visible half mitochondria (in red) and their overlap regions (in white) at the x-y plane with z = 0 µm.

6.3 Simulation results

We verified the correct implementation of the Magnus and Keizer model [106] by reproducing the figures of the corresponding study (data not shown). Then, we investigated the mitochondria model combined with the ODE-Mahajan model using the different NCLX and MCU models. Moreover, we investigated the influence of VDAC. Afterwards, we included the mitochondria model into our whole cell model.

6.3.1 Mitochondria model and ODE electrophysiology model

NCLX We ran one simulation for 525 s with a BCL of 350 ms for each NCLX model: (1) Magnus [106], (2) Cortassa [74], (3) Mahajan [6], and (4) Dash model [4]. The $[Ca^{2+}]_i$ transient during one AP for the Magnus, Cortassa, and the Mahajan NCLX model are shown in Figure 34. The $[Ca^{2+}]_i$ transient for the Dash NCLX model is not shown, because it was identical to the $[Ca^{2+}]_i$ transient of the Mahajan NCLX model except for a marginally higher peak $[Ca^{2+}]_i$. Reducing V_{max}^{NCLX} of the Cortassa model below 0.084 mM/ms caused Ca^{2+} alternans. The $[Ca^{2+}]_i$ and the $[Ca^{2+}]_{mito}$ dynamics were almost the same for the different NCLX models except for the Cortassa NCLX model. We preferred the Mahajan and the Dash model for subsequent analyses as will be discussed in Chapter 6.4.

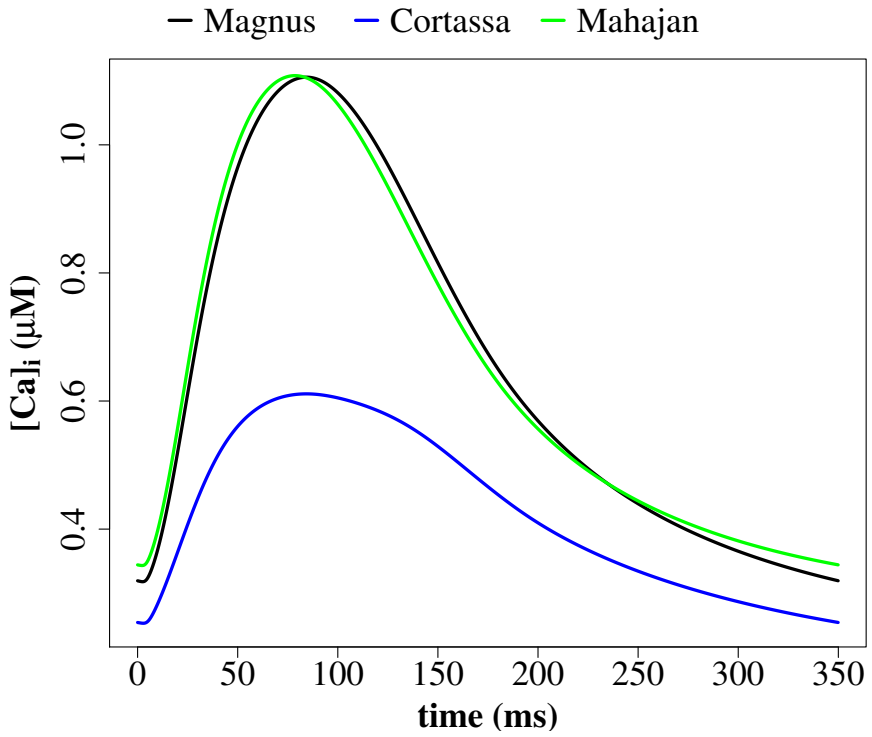

Figure 34: **The comparison of different NCLX models:** The $[Ca^{2+}]_i$ transients during one AP for (1) the original model by Magnus and Keizer [106] ("Magnus", in black), (2) the model by Cortassa et al. (2006) [74] ("Cortassa", in blue), and (3) the NCX model used by Mahajan et al. (2008) [6] ("Mahajan", in green). The $[Ca^{2+}]_i$ transient of the model by Dash and Beard (2008) [4] ("Dash") was omitted as it was identical to the $[Ca^{2+}]_i$ transient of the Mahajan NCLX model except for a marginally higher peak $[Ca^{2+}]_i$. Plot shows the last AP of a 525 s simulation.

MCU We ran one simulation for 525 s with a BCL of 350 ms for each MCU model: (1) Magnus [106], (2) Nguyen [5], and (3) Dash model [4]. For all three MCU models we used the Mahajan NCLX and the Dash NCLX model, respectively, as these were the most realistic models from the previous analysis. However, the $[Ca^{2+}]_{mito}$ and the $[Ca^{2+}]_i$ transients were almost identical with both NCLX models and for all three MCU models with adjusted V_{max}^{uni} (data not shown).
Then, we ran a simulation with changing BCLs to test for heart rate dependent differences in mitochondrial Ca^{2+} dynamics. The simulation was started with a BCL of 500 ms for 200 s, then the BCL was set to 250 ms for 200 s, and then again to a BCL of 500 ms for 200 s. The parameters V_{max} for NCLX and MCU were set to 0.0001 mM/ms and 0.0275 mM/ms, respectively, according to [240]. The $[Ca^{2+}]_i$ and $[Ca^2]_{mito}$ transients are shown in Figure 35A and Figure 35C (black lines), respectively. The $[Ca^{2+}]_i$ and the $[Ca^{2+}]_{mito}$ increased marginally during the first 200 s with a BCL of 500 ms. Decreasing the BCL to 250 ms increased the $[Ca^{2+}]_{mito}$ almost linearly to ∼1 µM and increased the $[Ca^{2+}]_i$ to ∼1.5 µM. Increasing the BCL to 500 ms again, reduced the $[Ca^{2+}]_{mito}$ to its starting value of ∼0.4 µM within 200 s. The $[Ca^{2+}]_i$ declined considerably as well, but did not reach its starting value within 200 s. Then, the simulation was repeated with V_{max}^{uni} reduced to 10 % (Figure 35B and 35C, in blue). The behaviour of the $[Ca^{2+}]_i$ was similar to the previous simulation, but the peak value after 200 s pacing with a BCL of 250 ms was higher with a value of ∼1.7 µM. The $[Ca^{2+}]_{mito}$ was reduced to almost zero within 100 s and the change of the BCL had only a minor effect.

VDAC The Dash MCU model was fitted to experimental data of respiring mitochondria, whereas the Nguyen MCU model was fitted to mitoplasts. Mitoplasts are lacking the OMM with VDAC. We compared both models by computing the J_{uni} for the Dash MCU model and the Nguyen MCU model, respectively, changing the $[Ca^{2+}]_i$ from 10^{-5} µM to 1 µM using a $[Ca^{2+}]_{mito}$ of 0.1 µM. The J_{uni} of the Nguyen model was squared to consider the cooperative binding of Ca^{2+} to the MCU used in the Dash MCU model and to allow the comparison of both models. In Figure 36 the results using an IMP of 180 mV are shown with solid lines and the results using an IMP of 90 mV are shown with dashed lines. J_{uni} increased considerably with increasing $[Ca^{2+}]_i$ using a IMP of 180 mV and increased less, if an IMP of 90 mV was used. J_{uni} of the Dash model increased more with IMP of 180 mV compared to the Nguyen model and it increased less with IMP of 90 mV compared to the Nguyen model. If $[Ca^{2+}]_{mito}$ was increased, J_{uni} decreased marginally more for the Dash model (data not shown).

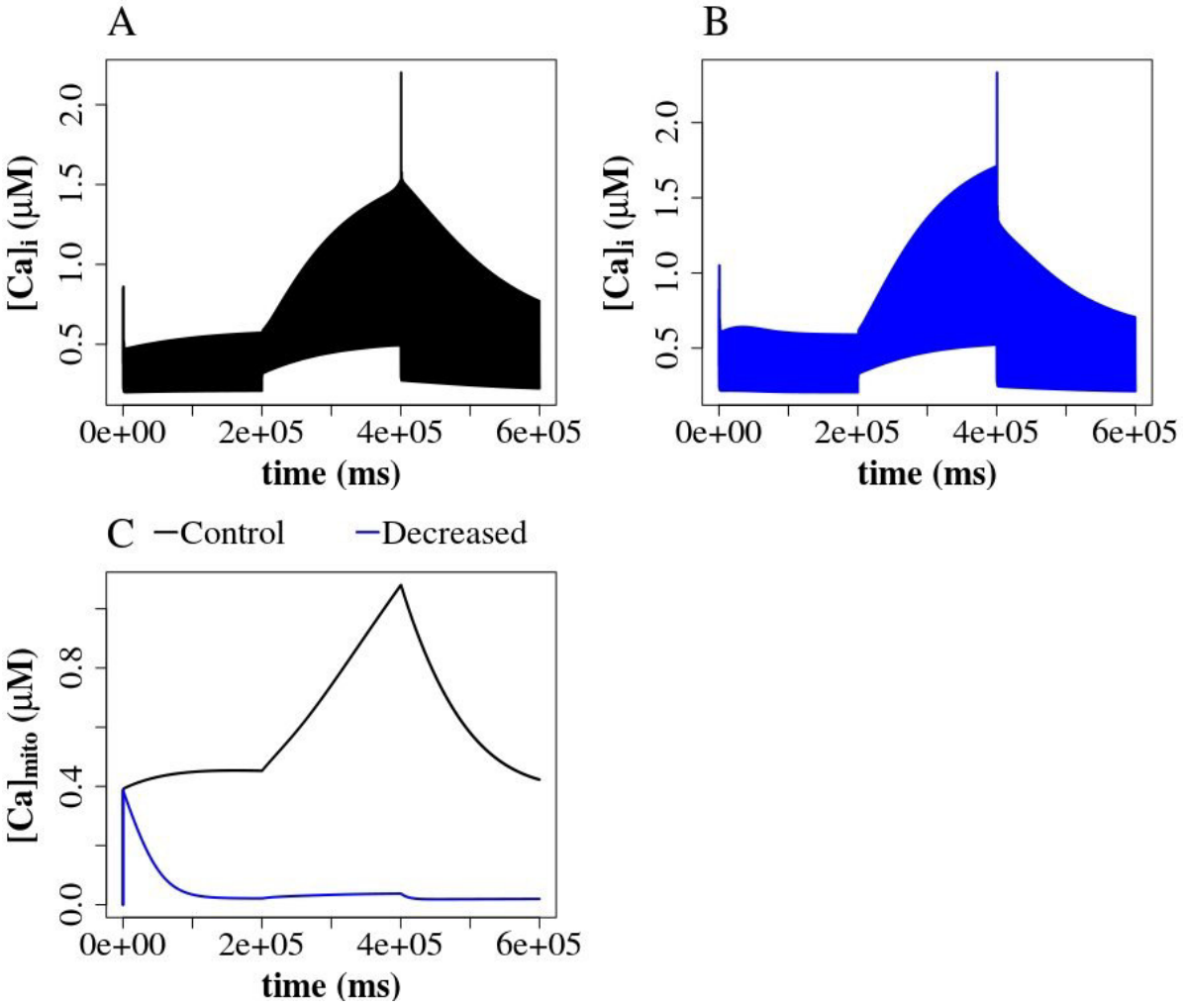

Figure 35: **The transients of $[Ca^{2+}]_i$ and $[Ca^{2+}]_{mito}$ during pacing:** At low frequency (BCL = 500 ms) for 200 s, then at high frequency (BCL = 250 ms) for 200 s, followed by a return to low frequency (BCL = 500 ms). **(A)** - $[Ca^{2+}]_i$ with $V_{max}^{uni} = 0.0275$ mM/ms ("Control"). **(B)** - $[Ca^{2+}]_i$ with V_{max}^{uni} decreased to 10 %. **(C)** - $[Ca^{2+}]_{mito}$ with control V_{max}^{uni} (in black) and decreased V_{max}^{uni} (in blue).

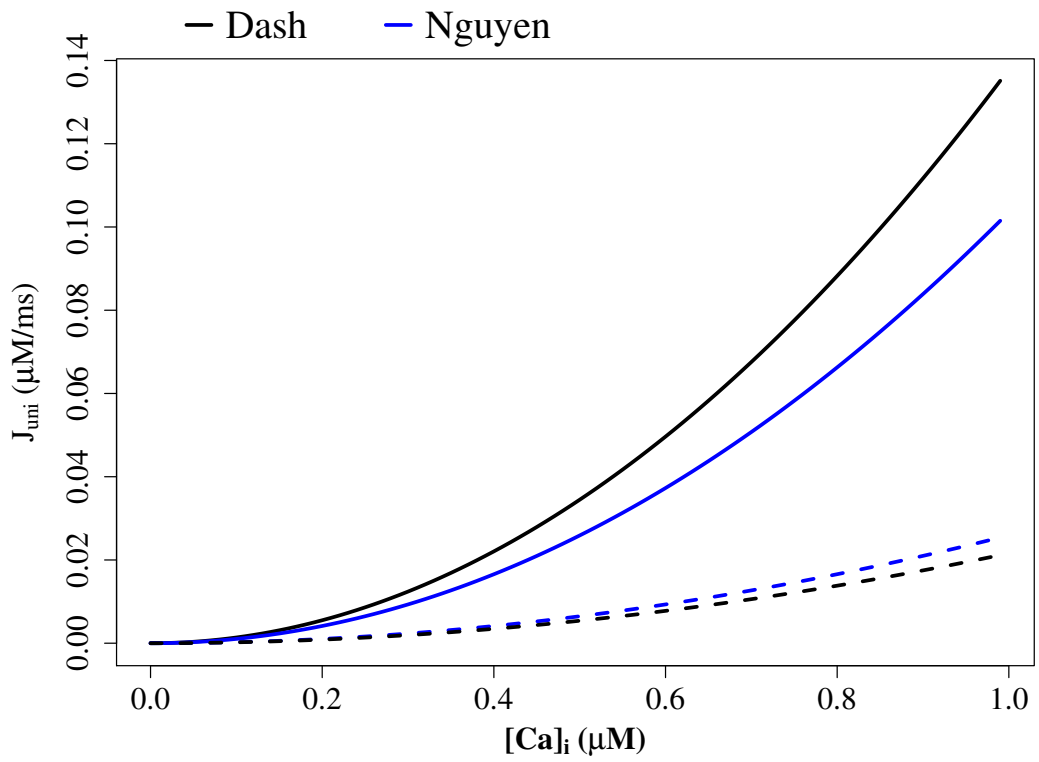

Figure 36: **The comparison of Dash MCU model [4] and Nguyen MCU model [5]:** J_{uni} of the Dash NCLX model at IMP of 180 mV (black, solid line) and at IMP of 90 mV (black, dashed line). J_{uni} of the Nguyen NCLX model at IMP of 180 mV (blue, solid line) and at IMP of 90 mV (blue, dashed line).

The effect of introducing mitochondria to the ODE-Mahajan model is shown by the $[Ca^{2+}]_i$ for the last three APs of a 525 s simulation with a BCL of 350 ms in Figure 37. The peak $[Ca^{2+}]_i$ was marginally higher and the resting $[Ca^{2+}]_i$ was marginally lower without mitochondria. This effect increased with increasing V_{max}^{uni}. However, if V_{max}^{uni} was increased to 0.011 μM/ms, Ca^{2+} alternans occurred. If V_{max}^{uni} was reduced below 0.0022 μM/ms, the $[Ca^{2+}]_i$ was unaffected. The minor change of the $[Ca^{2+}]_i$ transient did not affect the AP shape.

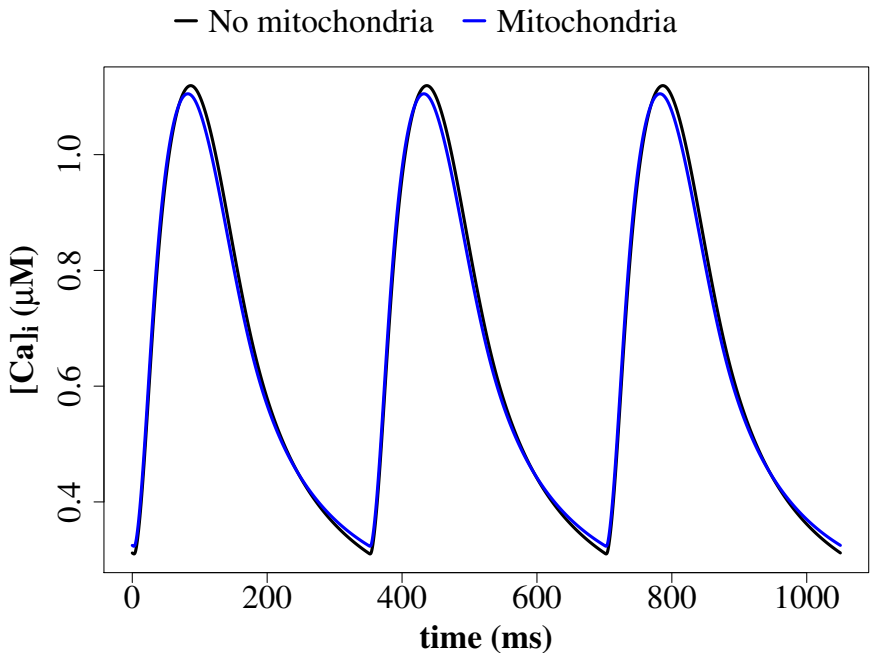

Figure 37: **Comparison of the $[Ca^{2+}]_i$ of the ODE-Mahajan model [6] with and without mitochondria:** using the MCU and NCLX model by Dash and Beard (2008)[4]. The plots show the last three APs of a 535 s simulation with a BCL of 350 ms.

6.3.2 Mitochondria model in the whole cell model

We ran a simulation of our whole cell model without the mitochondria in which the $[Ca^{2+}]_i$ showed a pronounced first peak followed by the principal peak (Figure 38, in black). Then we incorporated the mitochondria and ran the same simulation for four APs with a BCL of 350 ms. The $[Ca^{2+}]_i$ of the last three APs is shown (Figure 38, in blue). The first peak $[Ca^{2+}]_i$ of each AP was reduced with the incorporated mitochondria, whereas the principal peak was increased from ∼0.65 μM to ∼0.8μM. The resting $[Ca^{2+}]_i$ was marginally higher with the mitochondria and the $[Ca^{2+}]_i$ transient started earlier.
The $[Ca^{2+}]_{mito}$ of all 120 half mitochondria for the four APs is shown with black lines and the mean $[Ca^{2+}]_{mito}$ is shown in red in Figure 39. The $[Ca^{2+}]_{mito}$ of all mitochondria increased during systole and remained constant during diastole. However, the total increase of $[Ca^{2+}]_{mito}$ clearly differed between the individual mitochondria. The mean $[Ca^{2+}]_{mito}$ increased from 0.3 μM to ∼0.403 μM during 1400 ms.

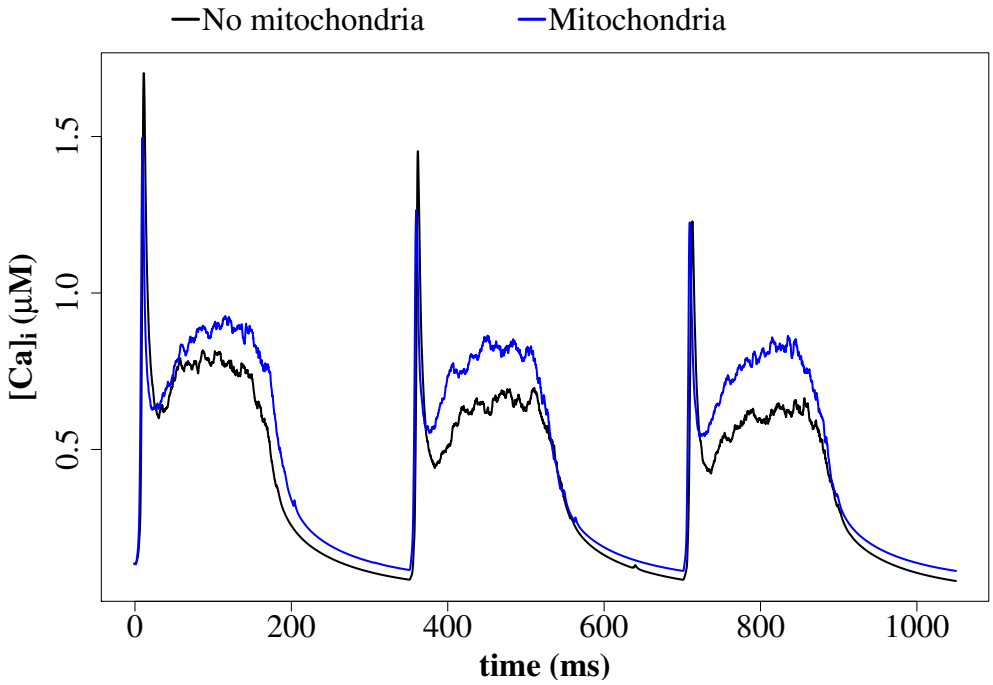

Figure 38: **Comparison of the $[Ca^{2+}]_i$ of the whole cell model with and without mitochondria:** using the MCU and NCLX model by Dash and Beard (2008)[4]. Plots show the second till fourth APs of a simulation with a quarter of a z-disc.

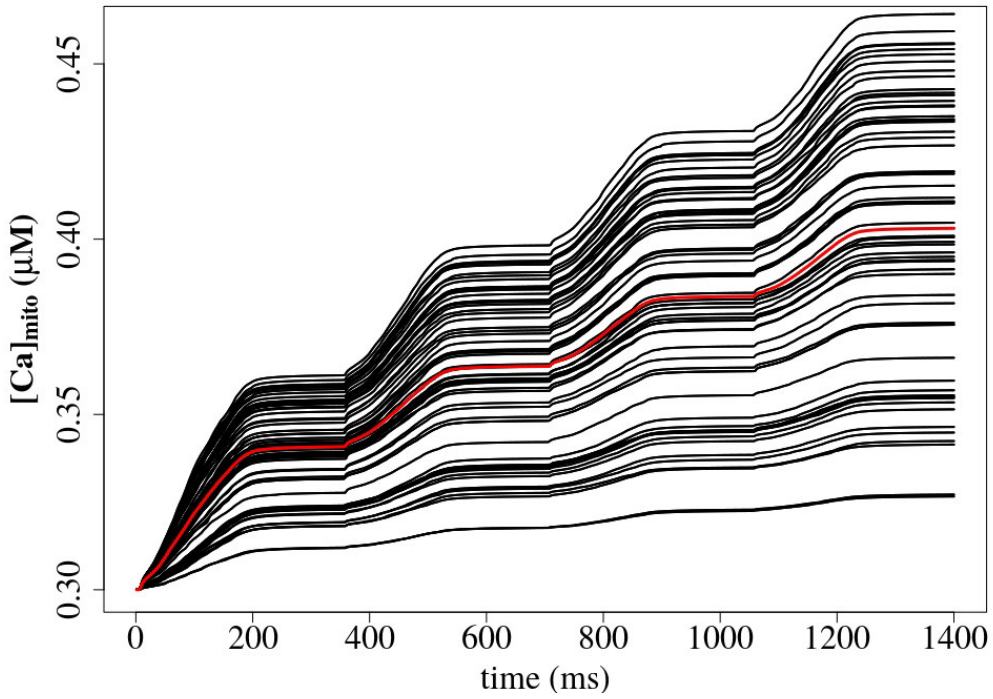

Figure 39: **$[Ca^{2+}]_{mito}$ for each mitochondrion (black) and mean $[Ca^{2+}]_{mito}$ (red):** Plots show the four APs of a simulation with a quarter of a z-disc.

6.4 The role of mitochondria

We used the mitochondria model of Magnus and Keizer (1997) [106] of a prancreatic β-cell. This model is widely used and was extended by others (for example [74], [80]) for a cardiac myocyte. This was possible because the Ca^{2+} influx into the mitochondria is similar for heart and liver [46]. We wanted to use a simple mitochondria model to investigate initially its influence on the Ca^{2+} cycling. We were not interested for the time being in the energy supply of the mitochondria and we therefore neglected the TCA cycle, which is incorporated in other mitochondria models.
There are a variety of models for NCLX and MCU. The NCLX flux of the Magnus model and of the Cortassa model is not zero at the Nernst equilibrium potential [241]. Cortassa extended the Magnus model by a dependency of $[Ca^{2+}]_i$, but in our simulations Ca^{2+} alternans occurred, if we reduced V_{max}^{nclx} considerably to achieve the same steady state $[Ca^{2+}]_{mito}$ as with the other NCLX models. We did not aim for Ca^{2+} alternans and therefore we discarded this model for subsequent analyses. We successfully adapted the Mahajan NCX model to the mitochondria. The NCLX model of Nguyen (2007) [5] was not considered, because this model was generalized by Dash and Beard (2008) [4]. There is also a NCLX model by Padhan et al. (2010) [242] which considers proton inhibition, but this is only important in pathological conditions. The simulation results for the adapted Mahajan NCLX model and the Dash NCLX model were the same under the tested conditions.
The Magnus MCU model is thermodynamically not balanced, because of its singularity at $\Delta\Psi = \Delta\Psi^* = 91$ mV [241]. The Nguyen MCU model was fitted to experimental data for mitoplasts and not for respiring mitochondria [241]. Hence, the Dash MCU model was the most realistic model, but differences between the models were not observed in our simulations under the tested conditions. Cortassa et al. (2008) [240] demonstrated that the increase of $[Ca^{2+}]_{mito}$ was reduced, if the value of V_{max}^{uni} was decreased to 10 %. In our simulations $[Ca^{2+}]_{mito}$ was reduced too much so that reducing BCL did not increase $[Ca^{2+}]_{mito}$. In summary, we were only able to show the dependency of MCU on the BCL for the control condition, but not for its reduced activity.
The fact that the Nguyen MCU model was fitted to experimental data of mitoplasts, which lack the OMM with VDAC, and that the Dash MCU model was adapted to respiring mitochondria make both models suitable to reveal difference caused by the gating of Ca^{2+} via the OMM through VDAC. VDAC is thought to be open at an OMP of 0 mV and to be closed at $\pm$60 mV [243]. VDAC favours Ca^{2+} in the closed state, and hence, the Ca^{2+} influx to the mitochondria was expected to be higher at the closed state for the Dash model compared to the Nguyen model and vice versa for the open state. We assumed that VDAC is open, if IMP was $\sim$180 mV and to be closed, if IMP is $\sim$90 mV (according to figures in [244]). We demonstrated that J_{uni} was reduced at OMP of 60 mV in the Dash model compared to the Nguyen model, which indicates that the open VDAC reduced the Ca^{2+} influx. Vice versa, J_{uni} was increased at OMP of 0 mV in the Dash model compared to the Nguyen model, which indicates that the closed VDAC favours the Ca^{2+} influx.
We showed that mitochondria with a high J_{uni} damped the $[Ca^{2+}]_i$ cycling. The peak was slightly lower and the resting value was marginally higher. However, if J_{uni} was too high, Ca^{2+} alternans occurred. Low J_{uni} had no effect on $[Ca^{2+}]_i$ in the ODE-Mahajan model. The MCU and NCLX were regulated only by the average $[Ca^{2+}]$ of the ODE-Mahajan model. It is hypothesized that MCU and NCLX might be regulated by locally

high $[Ca^{2+}]$ of microdomains, because mitochondria are reported to be located near the CRUs [45, 46] and the SR [47, 48].
We successfully incorporated the mitochondria ODE model in our whole cell model and investigated its influence on the $[Ca^{2+}]_i$. The first peak of $[Ca^{2+}]_i$ was reduced by the mitochondria as expected and discussed in Chapter 3.4. However, the principal peak of $[Ca^{2+}]_i$ was increased by the mitochondria. We observed the opposite using the mitochondria model combined with the ODE-Mahajan model. The $[Ca^{2+}]_{\text{mito}}$ increased during four APs and did not show the cycling behaviour as shown with the ODE-Mahajan model. A thorough parameter fitting will be necessary to replicate the cycling behaviour with the ODE-Mahajan model. However, we showed that the $[Ca^{2+}]_{\text{mito}}$ between the mitochondria varied probably because of their different distance to CRUs with open RyRs, and hence, the different $[Ca^{2+}]$ around each mitochondrion. The overall behaviour was the same for all mitochondria.

6.5 Conclusions

We used the ODE-Mahajan model as a framework to incorporate the mitochondria model by Magnus and Keizer (1997) [106]. This model allowed us to investigate different channel models with a reasonable running time. Our aim was to choose MCU and NCLX models which show physiological behaviour of a ventricular cardiac myocyte and to show reported properties of the channels. Both channel models by Dash and Beard (2008) [4] fulfilled these conditions. Moreover, their MCU model is fitted to experimental data of respiring mitochondria which led us to model the VDAC not explicitly, because its influence is already incorporated in the Dash MCU model. However, in future, the development of a VDAC model is of great interest, because VDAC is neglected in studies using mitoplasts and little is known about its kinetics and its role for Ca^{2+} influx to mitochondria. The combined physiological model of a rabbit and the mitochondria model is an excellent model to investigate a large number of hypotheses.
We successfully implemented the mitochondria model in our whole cell model. We showed that the first peak of the $[Ca^{2+}]_i$ was reduced and peaked earlier with the mitochondria. However, the principal peak was increased in contrast to the results with the ODE-Mahajan model. We revealed that the $[Ca^{2+}]_{\text{mito}}$ increased differently fast between the individual mitochondria but the overall profile was the same. Further parameter fitting is necessary for deeper insights, but the first results are promising that the mitochondria implementation will help to better understand the role of mitochondria and their channels in health and disease.

7 Conclusions and outlook

Ca^{2+} is the key mediator of ECC in cardiac myocytes and has been studied for many decades. Dysfunction of Ca^{2+} dynamics are associated with disease and heart failure, which emphasizes the high interest for understanding Ca^{2+}-driven processes in cardiac myocytes and the involved components. However, super-resolution microscopic techniques are just emerging and dynamics of ions in nanometer scale are not well studied. Locally high ion concentrations regulate receptors and are crucial for the forwarding of the chemical signal to the target of contraction. Multi-scale modelling is able to demonstrate the importance of such microdomains for global phenomena. However, it is challenging to merge models of different types and scales in one model.

In this study we developed such a multi-scale, whole cell model of a rabbit cardiac myocyte including Ca^{2+} dynamics at the single channel level up to many z-discs using high performance computing in Chapters 2 and 3. To our knowledge, our model is so far the only whole cell AP model which includes CRUs clustered around the z-discs and spatial resolution of intra-CRU $[Ca^{2+}]$ showing realistic steep $[Ca^{2+}]$ gradients in these microdomains. We used the finite element method, parallel computing and mathematical multi-scale techniques, such as Green Function and quasistatic approximation, to simulate almost one third of a ventricular cardiac myocyte with spatially resolved $[Ca^{2+}]$ and Ca^{2+}-buffers. The size of the domain is scalable by setting the number of z-discs and CRUs. The individual LCCs and RyRs are modelled stochastically using Markov chain models. The modularity of our model allows to easily exchange and investigate different RyR Markov chain models in Chapter 3. The 2-state Markov chain model by Walker et al. (2014) [3] showed the best physiological behaviour in our model compared with the 4-state model by Stern et al. (1999) [1] and the 2-state model by Cannell et al. (2013) [2]. Additionally, the Walker model incorporates modulation of the RyR-opening rate by junctional RyR-lumenal $[Ca^{2+}]$. Initially, induction decay as the sole CICR termination mechanism in an AP could not be demonstrated in our model as strong buffering was necessary. Subsequent parameter fitting solved this problem and a realistic spark frequency during rest has been achieved. We constantly cross-compared the Ca^{2+} dynamics and the shape of the NCX current to literature values. The early local maximum of the $[Ca^{2+}]_i$ was reduced by incorporating mitochondria to our whole cell model as expected in Chapter 6.3.2.

One main issue of implementing such a highly complex whole cell model is the parametrization. The parameters are high in numbers, interlinked, and often not precisely known, because experimental designs vary and different species are differently well studied. Species-dependent parameters cannot easily be transferred from one model to another. Hence, we had to define target values representing key properties of physiological behaviour of a rabbit cardiac myocyte. We were able to sufficiently approximate most of these target values by switching to the SERCA model by Sneyd (2003) [154] with a feedback inhibitor, excluding calsequestrin from the nSR, and adapting parameters of SERCA and the refill flux in Chapter 4. Nevertheless, the peak $[Ca^{2+}]_i$ and the number of sparks per diastole were still too high compared with literature values.

The function and role of NCX is still controversial, because potent and specific inhibitors are lacking. We revealed that NCX is crucial to maintain the physiological Ca^{2+} cycling in a rabbit cardiac myocyte under the restriction that a PMCA current and a background Ca^{2+} current were neglected in our model in Chapter 5. Both were implemented, but they disrupted the Ca^{2+} cycling and a comprehensive parameter scan will be necessary.

In our model NCX is regulated by local $[Ca^{2+}]_i$, which is an advantage over other model approaches. However, the introduction of a locally high $[Na^+]_i$ regulating NCX did not improve the shape of the NCX current despite its shown strong dependency on $[Na^+]_i$ in such that it did not switch earlier to a negative current during an AP. The cellular distribution of NCX is not clear according to the literature and we therefore implemented and investigated a possible high concentration of NCX inside and near the CRUs based on the microscopic study of Jayasinghe et al. (2009) [124], which we called heterogeneous NCX. Unfortunately, the long simulation time of our model restricted the number of NCX conditions, so that we investigated the complete NCX inhibition, homogeneous NCX, and the heterogeneous NCX implementation. The complete NCX inhibition in our whole cell model revealed the importance of the NCX for the Ca^{2+} cycling in rabbit cardiac myocytes. A complete inhibition of NCX was not yet revealed in experiments because of the lacking potent inhibitors. Our heterogeneous NCX reproduced the properties of spark behaviour reported by experimental and modelling approaches except for a reduction of the spark frequency and spark amplitude without pacing. However, it is challenging to cross-compare models with each other, because assumptions, experimental designs, and species differ. A wide-range investigation with a high number of sparks requires more computer resources and sophisticated methods, but might reveal more details about the influence of NCX on spark properties in future. We observed a contribution of NCX to triggering RyRs. Perhaps, it is worthwhile to introduce NCX directly into the CRU model to investigate further immediate effects on LCCs and RyRs. In summary, we support the hypothesis of a high NCX distribution inside and near CRUs, and therefore, we favour our newly implemented heterogeneous NCX. It shows better physiological behaviour than the homogeneous NCX implementation.

Mitochondria play a crucial role as energy supplier for cardiac myocytes. However, we were interested in its role as Ca^{2+}-buffer. We needed to find an appropriate mitochondria model, which we could include in our whole cell model. We therefore combined the mitochondria model by Magnus and Keizer [106] with the ODE-Mahajan model in Chapter 6. We used the combined ODE model to investigate different models for MCU and NCLX. The models differ only marginally under the tested conditions. Nevertheless, we chose the Dash Ca^{2+} channel models to use in our whole cell model, because they were fitted to respiring mitochondria. The inclusion of the mitochondria marginally damped the $[Ca^{2+}]_i$ oscillations in the ODE-Mahajan model. We expected a more pronounced influence of the mitochondria on $[Ca^{2+}]_i$ in our whole cell model, because of the influence of locally high $[Ca^{2+}]_i$ in microdomains on channel kinetics. We successfully implemented the mitochondria model in our whole cell model. The explicit representation of individual mitochondria allowed to show their different behaviour which depends on local $[Ca^{2+}]$. However, some features contradicted the results with the ODE-Mahajan model. Further investigation and parameter fitting will be necessary to reveal, if the differences are based on the spatially resolved $[Ca^{2+}]$ in the whole cell model.

We showed with our detailed whole cell model that microdomains are important for the kinetics of channels. The location of channels relative to other channels or compartments, and hence, microdomains enhance their gating role. This applies to all investigated channels and exchangers, such as RyRs, SERCA, MCU, and NCLX.

Modelling a whole cell with all its compartments, channels, and spatially resolved Ca^{2+} and Ca^{2+}-buffer dynamics is a highly complex and difficult task, but with much potential to reveal new insights in key processes and dysfunctions. Multi-scale modelling asks for high performance computing. We constantly improved the performance of our model,

for example by improving the time-stepping scheme, which was not part of this study, or using a quasistatic approximation for fast processes. Nevertheless, single simulations take hours to weeks to run in parallel fashion using tens to hundreds of CPUs for a subset of a cardiac myocyte. Such time consuming simulations make data collection for statistical evaluation difficult, which weakens the significance of our parameter analysis. We always aimed to use submodels as simple as possible to restrict the number of parameters, but still showing relevant properties to be able to answer biological questions. We cannot exclude that more sophisticated models for the channels and compartments might show better results, but they might come along with performance penalty. We aimed to include the main contributors for Ca^{2+} dynamics in our model, whereas less important channels, such as a PMCA current and background Ca^{2+} current, are not yet investigated thoroughly in our model. Our whole cell model does not include myocardial energetics or contraction as it lacks the TCA cycle, spatially resolved ADP and myofilaments.
Improving and extending a model is an ongoing process. We constantly addressed arising problems. However, the investigated channels and compartments might be re-investigated and further improved in future studies, because many parameters were changed in the meantime. The role of mitochondria for spark properties and for the Ca^{2+} transient might be investigated. Moreover, the influence of the energetics for Ca^{2+} transient, and hence, contraction might be easy to investigate by adding corresponding equations to the mitochondria model. As a starting point, ADP will be spatially resolved in our model. This will allow to investigate the influence of ATP on the SERCA and NCX activity. In future, the aim is to include myofilaments into our model, and hence, to simulate force generation and contraction. Some types of cardiac myocyte dysfunction and diseases can be implemented by small changes of parameters, for example the height of the cleft and the number of RyRs to represent the detubulated cardiac myocyte of heart failure. Our complex, multi-scale model can easily be extended and adapted to new experimental findings. Furthermore, other species with low heart rates can be easily investigated by replacing the electrophysiology module. Further parameter fitting for species with large heart rates will be necessary, because there are considerable differences between small animals with high heart rates and larger animals with low heart rates as we pointed out in Chapter 4.1.2, 5.1.3, and 6.1.2. Our model is highly useful to investigate Ca^{2+} sparks, Ca^{2+} waves, and the role of channels and compartments. Hence, it will belong to the next generation of whole cell models of a cardiac myocyte and will contribute to the development of whole heart models.

A Appendix

A.1 Tables

Table A.1: **Buffering and diffusion parameters**

Parameter	Description	Chapter 3	Chapter 4	Chapter 5 & 6
b_m^{tot}	Total conc. of troponin C (stationary buffer)	53.0 µM	25.0 µM	
b_s^{tot}	Total conc. of calmodulin (mobile buffer)	133. µM	70.0 µM	
B_{sr}^{tot}	Total conc. of calsequestrin (SR buffer)	1500.0 µM		800 µM (jSR)
$b_{Fluo\text{-}4}^{tot}$	Total conc. of Fluo-4	133.0 µM	25.0 µM	
k_s^+	On rate for troponin C binding	0.043 μM^{-1} ms^{-1}		
k_s^-	Off rate for troponin C binding	0.026 ms^{-1}		
k_m^+	On rate for calmodulin binding	0.8 μM^{-1} ms^{-1}	0.023 μM^{-1} ms^{-1}	
k_m^-	Off rate for calmodulin binding	0.2 ms^{-1}	0.238 ms^{-1}	
k_{sr}^+	On rate for calsequestrin binding	0.1 μM^{-1} ms^{-1}	0.07 μM^{-1} ms^{-1}	
k_{sr}^-	Off rate for calsequestrin binding	60.0 ms^{-1}	80.0 ms^{-1}	
$k_{Fluo\text{-}4}^+$	On rate for Fluo-4 binding	0.0488 μM^{-1} ms^{-1}		
$k_{Fluo\text{-}4}^-$	Off rate for Fluo-4 binding	0.0439 ms^{-1}		
D_b^m	Diffusion constant of troponin C	0.04 μm^2 ms^{-1}		
D_B	Diffusion constant of SR buffer	0.01 μm^2 ms^{-1}		
D	Diffusion constant of Ca^{2+}	0.22 μm^2 ms^{-1}		
D_S	Diffusion constant of SR Ca^{2+}	0.20 μm^2 ms^{-1}		
$D_{Fluo\text{-}4}$	Diffusion constant of Fluo-4	0.033 μm^2 ms^{-1}		
τ_d	Refill-flux constant	0.5 ms		4.0 ms
c_0	Starting $[Ca^{2+}]_i$	0.275 µM		

Table A.2: **Exchanger and uptake parameters**

Parameter	Definition	Chapter 3	Chapter 4	Chapter 5 & 6
f_{NCX}^{high}	Maximal factor for g_{NaCa}	2.5	6.0	0.0/1.0/72.0
f_{NCX}^{low}	Minimal factor for g_{NaCa}	1.5	1.0	0.0/1.0/0.66
f_{NCX}^{surf}	Factor for g_{NaCa} at surface	0.5	–	–
K_p	Uptake threshold	0.2 µM		0.4 µM
V_P^{max}	Strength of uptake	0.8 µM ms^{-1}		0.4 µM ms^{-1}
g_{NaCa}	Strength of NCX	0.84 µM ms^{-1}		
k_{sat}	Constant	0.2		
ξ	Constant	0.35		
$K_{m,Nai}$	Constant	12.3 mM		
$K_{m,Nao}$	Constant	87.5 mM		
$K_{m,Cai}$	Constant	0.0036 mM		
$K_{m,Cao}$	Constant	1.3 mM		
c_{naca}	Constant	0.3 µM		

Table A.3: **Physical constants and ionic concentrations**

Parameter	Definition	Chapter 3	Chapter 4 & 5 & 6
C_m	Cell capacitance	3.1. $\times 10^{-4}$ µF	
ν_{cell}	Whole cell volume	2.58 $\times 10^{-5}$ µl	
Ω	Simulated subcell volume	0.72 $\times 10^{-5}$ µl	1.125 $\times 10^{-7}$ µl
x $\times$ y	Cross-section of simulated volume	15 $\times$ 15 µm^2	7.5$\times$ 7.5 µm^2
z	Height of simulated volume	32 µm	2 µm
F	Faraday constant	96.5 C mmol^{-1}	
R	Universal gas constant	8.315 Jmol^{-1} K^{-1}	
T	Temperature	308 K	
$[Na^+]_o$	External sodium concentration	136 mM	
$[K^+]_i$	Internal potassium concentration	140 mM	
$[K^+]_o$	External potassium concentration	5.4 mM	
c_{ext}	External Ca^{2+} concentration	2.0 mM	1.8 mM
$\nu_{\text{sr}}/\nu_{\text{cell}}$	Ratio of SR to cell volume	0.1	0.08
$\nu_{\text{jsr}}/\nu_{\text{cell}}$	Ratio of jSR to cell volume	0.005	
$\nu_{\text{cyt}}/\nu_{\text{cell}}$	Ratio of cytosolic volume to cell volume	0.895	0.915
κ	Constant in Equation (18)	1 nm^{-1}	
ϕ_0	Constant in Equation (18)	-2.2	

Table A.4: **LCC and RyR parameters** for models by Stern et al. (1999) [1], Cannell et al. (2013) [2] and Walker et al. (2014) [3].

Parameter	Definition	Chapter 3	Chapter 4 & 5 & 6
N_c	Number of CRUs	5120	77
N_{RyR}	Average number of RyRs per CRU	50	63
N_{LCC}	Average number of LCCs per CRU	12.5	12.6
$r_{RyR,LCC}$	Ratio of RyRs and LCCs	4.0	5.0
LCC parameters			
g_{LCC}	LCC single channel conductance	0.000546 μm^3 ms^{-1}	
k_p^0	Threshold for Ca-induced inactivation	405.0 μM	90.0 μM
$\bar{c}_p$	Threshold for Ca dependence of transition rate k_6	270.0 μM	60.0 μM
τ_{po}	Time constant of activation	1 ms	
r_1	Opening rate	0.3 ms^{-1}	
r_2	Closing rate	3 ms^{-1}	
s_1'	Inactivation rate	0.00195 ms^{-1}	
k_1'	Inactivation rate	0.00413 ms^{-1}	
k_2	Inactivation rate	0.0001 ms^{-1}	
k_2'	Inactivation rate	0.00224 ms^{-1}	
T_{Ba}	Time constant	450 ms	
RyR parameters (Stern et al. (1999) [1] as modified by [87])			
g_{RyR}	RyR permeability	4 μm^3 s^{-1}	–
k_{om}	Activation rate	60 s^{-1}	–
k_{im}	Inactivation rate	5 s^{-1}	–
k_{ac}^{max}	Maximal activation rate	928.8 s^{-1}	–
k_{in}^{max}	Maximal inactivation rate	7.8 s^{-1}	–
K_{jsr}	Half max. value for c_{jsr}-effect on RyR	550 μM	–
K_{ac}	Activation threshold	8.5 μM	–
K_{in}	Inactivation threshold	8.5 μM	–
λ	Asymmetric inactivation	27.5	–
RyR parameters (Cannell et al. (2013) [2])			
g_{RyR}	RyR permeability	4 μm^3 s^{-1}	–
k_{open}	Opening rate	4.57×10^5 ${c_{di}}^{2.12}$ s^{-1}	–
k_{open}^{max}	Maximal opening rate	800 s^{-1}	–
k_{close}	Closing rate	245 ${c_{di}}^{-0.27}$ s^{-1}	–
RyR parameters (Walker et al. (2014) [3])			
g_{RyR}	RyR permeability	1.1 μm^3 s^{-1}	3.1 μm^3 s^{-1}
η	Ca^{2+} Hill coefficient	2.1	
k_{open}	Opening rate	$k^+ \phi c_{di}^{\eta}$	
k^+	Opening rate constant	0.02 $\times 10^{-4} ms^{-1}$ $\mu M^{-\eta}$	0.15 $\times 10^{-4} ms^{-1}$ $\mu M^{-\eta}$
k_{close}	Closing rate	0.5 s^{-1}	
ϕ	$[Ca^{2+}]_{jsr}$- dependent regulation term	$\phi_b + ([Ca^{2+}]_{jsr}/\phi_k)^4$	–
ϕ_k	$[Ca^{2+}]_{jsr}$- dependent regulation affinity	1.5 mM	–
ϕ_b	$[Ca^{2+}]_{jsr}$- dependent regulation intercept	0.8025	–

Table A.5: **Ionic current conductances**

Parameter	Definition	Value
g_{Na}	Peak I_{Na} conductance	12.0 mS μF^{-1}
$g_{to,f}$	Peak $I_{to,f}$ conductance	0.11 mS/μF^{-1}
$g_{to,s}$	Peak $I_{to,s}$ conductance	0.04 mS/μF^{-1}
g_{K1}	Peak I_{K1} conductance	0.3 mS/μF^{-1}
g_{Kr}	Peak I_{Kr} conductance	0.0125 mS/μF^{-1}
g_{Ks}	Peak I_{Ks} conductance	0.1386 mS/μF^{-1}
g_{NaK}	Peak I_{NaK} conductance	1.5 mS/μF^{-1}

Table A.6: **Target values for SR parameter fitting**

Parameter	Target value
APD_{90}	∼185 ms
Peak $[Ca^{2+}]_i$	∼1.1 µM
$[Ca^{2+}]_{nSR}$ depletion	20 % - 60 %
$[Ca^{2+}]_{nSR}$	∼80 µmol/l cytosol
$[B_{sr}]$	< 2.9 mM SR
τ_d	∼4 ms

Table A.7: **Normalized percentages of NCX to determine the NCX factor (f_{NCX})**

Distance [µm]	% of punctate NCX	Volume factor	Percentage [%]
0.05	5.2	1	100
0.1	17.9	7	49.2
0.15	19.3	19	19.5
0.2	14.8	37	7.7
0.25	8.7	61	2.7
0.3	7.2	91	1.5
0.35	7.1	127	1.1
0.4	4.2	169	0.5
0.45	3.7	217	0.3
0.5	2.9	271	0.2
0.55	2.1	331	0.1

Table A.8: **The comparison of NCX models**

Parameter	No NCX	Homogeneous NCX	Heterogeneous NCX
APD_{90}	-	192.4 ms	192.6 ms
Peak $[Ca^{2+}]_i$	$\sim$ 30.0	2.48 µM	1.84 µM
Time-to-peak of $[Ca^{2+}]_i$	-	112.5 ms	101.5 ms
Peak RyR flux	-	2.71 µM/s	2.16 µM/s
Sparks/diastole	-	1.0	0.0
nSR depletion	-	14.6 %	14.0 %
Ca^{2+} removal	-	24.2 %	21.2 %

Table A.9: **The comparison of NCX models with 50 % LCC activity**

Parameter	No NCX	Homogeneous NCX	Heterogeneous NCX
APD_{90}	115.3	121.8 ms	140.6 ms
Peak $[Ca^{2+}]_i$	2.2 µM	0.99 µM	1.02 µM
Time-to-peak of $[Ca^{2+}]_i$	65.7 ms	55.3 ms	68.2 ms
Peak RyR flux	2.35 µM/s	2.05 µM/s	1.95 µM/s
Sparks/diastole	4.75	1.5	2.25
nSR depletion	15.9 %	11.9 %	9.9 %

Table A.10: **The comparison of homogeneous and heterogeneous NCX distribution depending on global $[Na^+]_i$**

Parameter	Homogeneous NCX		Heterogeneous NCX	
$[Na^+]_i$	15.42 mM	20.42 mM	15.42 mM	20.42 mM
APD_{90}	169.7 ms	163.2 ms	180.2 ms	161.6 ms
Peak $[Ca^{2+}]_i$	4.34 µM	7.53 µM	3.83 µM	6.26 µM
Time-to-peak of $[Ca^{2+}]_i$	97.04 ms	92.2 ms	101.9 ms	87.0
Peak RyR flux	2.65 µM/s	3.37 µM/s	2.65 µM/s	3.61 µm/s
Sparks/diastole	3.0	2.5	3.0	2.75
nSR depletion	15.7 %	18.0 %	9.9 %	17.2 %

Table A.11: **The comparison of homogeneous and heterogeneous NCX distribution depending on local $[Na^+]_i$**

Parameter	Homogeneous NCX		Heterogeneous NCX	
$[Na^+]_i$	13.0 mM	15.0 mM	13.0 mM	15.0 mM
APD_{90}	180.4 ms	174.4 ms	183.6 ms	209.9 ms
Peak $[Ca^{2+}]_i$	1.03 µM	0.94 µM	0.72 µM	0.81 µM
Time-to-peak of $[Ca^{2+}]_i$	136.6 ms	110.38 ms	117.5	128.8
Peak RyR flux	2.15 µM/s	0.75 µM/s	1.88 µM/s	2.06 µm/s
Sparks/diastole	3.0	0.5	0.25	2.75
nSR depletion	12.6 %	12.4 %	11.8 %	11.9 %

Table A.12: **Mitochondria parameters: oxidative phosphorylation (adapted from [74])**

Parameter	Definition	Value
r_a	Sum of products of rate constants	6.394 10^{-10}
r_b	Sum of products of rate constants	1.762 10^{-13}
r_{c1}	Sum of products of rate constants	2.656 10^{-19}
r_{c2}	Sum of products of rate constants	8.632.394 10^{-27}
r_1	Sum of products of rate constants	2.077 10^{-18}
r_2	Sum of products of rate constants	1.728 10^{-9}
r_3	Sum of products of rate constants	1.059 10^{-26}
ρ^{res}	Concentration of electron carries	0.05 mM
K_{res}	Equilibrium constant of respiration	1.35 10^{18}
$\rho^{res(F)}$	Concentration of electron carries	0.0045 mM
$\Delta\Psi_B$	Phase boundary potential	0.05 V
g	Correction factor for voltage	0.85
p_a	Sum of products of rate constants	1.656 10^{-10} s^{-1}
p_b	Sum of products of rate constants	3.373 10^{-7} s^{-1}
p_{c1}	Sum of products of rate constants	9.651 10^{-14} s^{-1}
p_{c2}	Sum of products of rate constants	4.585 10^{-14} s^{-1}
p_1	Sum of products of rate constants	1.346 10^{-8}
p_2	Sum of products of rate constants	7.739 10^{-7}
p_3	Sum of products of rate constants	6.65 10^{-15}
ρ^{F1}	Concentration of F_1F_0-ATPase	0.0875 mM
K_{F1}	Equilibrium constant of ATP hydrolysis	1.71 10^6
P_i	Inorganic phosphate concentration	20.0 mM
C_m	Total sum of mito adenine nucleotides	10.0 mM
V_{max}^{ANT}	Maximal rate of ANT	2.0833 mM s^{-1}
$[ADP]_i$	Cytoplasmic ADP_i concentration	0.02 mM
$[ATP]_i$	Cytoplasmic ATP_i concentration	6.5 mM
g_H	Ionic conductance of the inner membrane	0.001 mM s^{-1} V^{-1}
ΔpH	pH gradient across the inner membrane	- 0.6
C_{mito}	Inner membrane capacitance	1.812 mM V^{-1}
ν_{mito}/ν_{cell}	Ratio of mitochondrial to cell volume	0.35

Table A.13: **Mitochondria parameters: Ca^{2+} dynamics of the model by Magnus and Keizer (1997) [106]**

Parameter	Definition	Value
$[Na^+]_{mito}$	Mitochondrial Na^+ concentration	5 mM
$\Delta\Psi^\circ$	Offset membrane potential	0.091 V
K_{act}	Activation constant	3.8 10^{-4} mM
K_{trans}	K_d for translocated Ca^{2+}	0.019 mM
L	K_{eq} for conformational transitions in uniporter	110.0
n_a	Uniporter activation cooperativity	2.8
b	$\Delta\Psi_m$ dependence of NCLX	0.5
K_{Na}	NCLX Na^+ constant	9.4 mM
K_{Ca}	NCLX Ca^{2+} constant	3.75 10^{-4} mM
n	NCLX cooperativity	3.0
f	Fraction of free $[Ca^{2+}]_m$	0.0003

Table A.14: **V_{max} values for NCLX and MCU models**

Model	V_{max}^{NCLX}	V_{max}^{uni}
Magnus [106]	1.8 10^{-3} µM s^{-1}	0.025 mM s^{-1}
Mahajan [6]	1.8 10^{-3} µM s^{-1}	–
Cortassa [240]	1.0 10^{-4} µM s^{-1}	–
Nguyen [5]	–	2.2 10^{-6} mM s^{-1}
Dash [4]	1.710^{-2} µM s^{-1}	2.2 10^{-3} mM s^{-1}

References

[1] M. D. Stern, L.-S. Song, H. Cheng, J. S. Sham, H. T. Yang, K. R. Boheler, and E. Ríos, "Local control models of cardiac excitation-contraction coupling a possible role for allosteric interactions between ryanodine receptors," *J. Gen. Phys.*, vol. 113, pp. 469–489, 1999.

[2] M. B. Cannell, C. H. Kong, M. S. Imtiaz, and D. R. Laver, "Control of sarcoplasmic reticulum Ca^{2+} release by stochastic RyR gating within a 3D model of the cardiac dyad and importance of induction decay for CICR termination," *Biophys. J.*, vol. 104, pp. 2149 – 2159, 2013.

[3] M. A. Walker, G. S. Williams, T. Kohl, S. E. Lehnart, M. S. Jafri, J. L. Greenstein, W. J. Lederer, and R. L. Winslow, "Superresolution modeling of calcium release in the heart," *Biophys. J.*, vol. 107, pp. 3018 – 3029, 2014.

[4] R. K. Dash and D. A. Beard, "Analysis of cardiac mitochondrial Na^+-Ca^{2+} exchanger kinetics with a biophysical model of mitochondrial Ca^{2+} handling suggests a 3:1 stoichiometry," *J. Physiol.*, vol. 586, pp. 3267–3285, 2008.

[5] M. H. Nguyen, S. J. Dudycha, and M. S. Jafri, "Effect of Ca^{2+} on cardiac mitochondrial energy production is modulated by Na^+ and H^+ dynamics," *Am. J. Physiol. Cell. Physiol.*, vol. 292, pp. C2004 – C2020, 2007.

[6] A. Mahajan, Y. Shiferaw, D. Sato, A. Baher, R. Olcese, L.-H. Xie, M.-J. Yang, P.-S. Chen, J. G. Restrepo, A. Karma, A. Garfinkel, Z. Qu, and J. N. Weiss, "A rabbit ventricular action potential model replicating cardiac dynamics at rapid heart rates," *Biophys. J.*, vol. 94, pp. 392–410, 2008.

[7] E. J. Benjamin, M. J. Blaha, S. E. Chiuve, M. Cushman, S. R. Das, R. Deo, S. D. de Ferranti, J. Floyd, M. Fornage, C. Gillespie, C. R. Isasi, M. C. Jiménez, L. C. Jordan, S. E. Judd, D. Lackland, J. H. Lichtman, L. Lisabeth, S. Liu, C. T. Longenecker, R. H. Mackey, K. Matsushita, D. Mozaffarian, M. E. Mussolino, K. Nasir, R. W. Neumar, L. Palaniappan, D. K. Pandey, R. R. Thiagarajan, M. J. Reeves, M. Ritchey, C. J. Rodriguez, G. A. Roth, W. D. Rosamond, C. Sasson, A. Towfighi, C. W. Tsao, M. B. Turner, S. S. Virani, J. H. Voeks, J. Z. Willey, J. T. Wilkins, J. H. Y. Wu, H. M. Alger, S. S. Wong, and P. Muntner, "Heart disease and stroke statistica - 2017 update - a report from the American Heart Association," *Circ.*, vol. 135, pp. e1 – e458, 2017.

[8] V. Fuster, R. W. Alxeander, R. A. O'Rouke, R. Roberts, S. B. King III, E. N. Prystowksy, and I. S. Nash, *Hurst's the heart.* New York: McGraw-Hill Medical, 11 ed., 2004.

[9] V. Foster, "Global burden of cardiovacular disease," *J. Am. Coll. Cardiol.*, vol. 64, pp. 520 – 522, 2014.

[10] G. Vilahur, J. J. Badimon, R. Bugiardini, and L. Badimon, "Perspectives: The burden of cardiovascular risk factors and coronary heart disease in Europe and worldwide," *Europ. Heart J. Suppl.*, vol. 16, pp. A7 – A11, 2014.

[11] D. M. Bers, *Excitation-contraction coupling and cardiac contractile force.* Dordrecht, The Netherlands: Kluwer Academic Publishers, 2001.

[12] S. Makino, K. Fukuda, S. Miyoshi, F. Konishi, H. Kodama, J. Pan, M. Sano, T. Takahashi, S. Hori, H. Abe, J. Hata, A. Umezawa, and S. Ogawa, "Cardiomyocytes can be generated from marrow stromal cells *in vivo*," *J. Clin. Invest.*, vol. 103, pp. 697 – 705, 1999.

[13] R. L. Winslow, M. A. Walker, and J. L. Greenstein, "Modeling calcium regulation of contraction, energetics, signaling, and transcription in the cardiac myocyte," *WIREs Syst. Biol. Med.*, vol. 8, pp. 37 – 67, 2016.

[14] E. D. Canale, R. Gordon, and J. J. Smolich, *Cardiac muscle.* Berlin, Heidelberg: Springer, 1986.

[15] F. Hofman, V. Flockerzi, S. Kahl, and J. W. Wegener, "L-type Cav1.2 calcium channels: from *in vitro* findings to *in vivo* function," *Physiol. Rev.*, pp. 303 – 326, 2014.

[16] L.-S. Song, E. A. Sobie, S. McCulle, W. J. Lederer, C. W. Balke, and H. Cheng, "Orphaned ryanodine receptors in the failing heart," *Proc. Natl. Acad. Sci. USA*, vol. 103, pp. 4305 – 4310, 2006.

[17] M. Nivala, E. de Lange, R. Rovetti, and Z. Qu, "Computational modeling and numerical methods for spatiotemporal calcium cycling in ventricular myocytes," *Front. Physiol.*, vol. 3, pp. 1–12, 2012.

[18] J. L. Greenstein and R. L. Winslow, "An integrative model of cardiac ventricular myocyte incorporating local control of Ca^{2+} release," *Biophys. J.*, vol. 83, pp. 2918 – 2945, 2002.

[19] H. Cheng and W. J. Lederer, "Calcium sparks," *Physiol. Rev.*, vol. 88, pp. 1491 – 1545, 2008.

[20] Z. Song, A. Karma, J. N. Weiss, and Z. Qu, "Long-lasting sparks: Multimetastability and release competition in the calcium release unit network," *PLoS Comp. Biol.*, vol. 12, pp. 1 – 24, 2016.

[21] T. M. Hoang-Trong, A. Ullah, and M. S. Jafri, "Calcium sparks in the heart: dynamics and regulation," *Res. and Rep. in Biol.*, vol. 6, pp. 203 – 214, 2015.

[22] A. Varró, D. A. Lathrop, S. B. Hester, P. P. Nánási, and J. G. Papp, "Ionic currents and action potentials in rabbit, rat, and guinea pig ventricular myocytes.," *Basic Res. Cardiol.*, vol. 88, pp. 93 – 102, 1993.

[23] M. M. Maleckar, A. G. Edwards, W. E. Louch, and G. T. Lines, "Studying dyadic structure-function relationships: a review of current modeling approches and new insights into Ca^{2+} (mis)handling," *Clin. Med. Insights: Cardiol.*, vol. 11, pp. 1 – 11, 2017.

[24] A. Fabiato and F. Fabiato, "Contractions induced by a calcium-triggered release of calcium from the sarcoplasmic reticulum of single skinned cardiac cells," *J. Physiol.*, vol. 249, no. 3, pp. 469 – 495, 1975.

[25] M. R. Webb and D. R. Trentham, *Chemical mechanism of myosin-catalyzed ATP hydrolysis*. American Physiology Society: Handbook of Physiology, 1983.

[26] J. Vierheller, W. Neubert, M. Falcke, S. H. Gilbert, and N. Chamakuri, "A multi-scale computational model of spatially resolved calcium cycling in cardiac myocytes: from detailed cleft dynamics to the whole cell concentration profiles," *Front. Physiol.*, vol. 6, pp. 1 – 15, 2015.

[27] M. D. Stern, "Theory of excitation-contraction coupling in cardiac muscle," *Biophys. J.*, vol. 63, pp. 497 – 517, 1992.

[28] M. B. Cannell, J. R. Berlin, and W. J. Lederer, "Effect of membrane potential changes on the calcium transient in single rat cardiac muscle cells," *Science*, vol. 238, pp. 1419 – 1423, 1987.

[29] L. Barcenas-Ruiz and W. G. Wier, "Voltage dependence of intracellular $[Ca^{2+}]_i$ transients in guinea pig ventricular myocytes," *Circ. Res.*, vol. 61, pp. 148 – 154, 1987.

[30] J. Altamirano and D. M. Bers, "Voltage dependence of cardiac excitation-contraction coupling: unitary Ca^{2+} current amplitude and open channel probability," *Circ. Res.*, vol. 101, pp. 590 – 597, 2007.

[31] X. Koh, B. Srinivasan, H. S. Ching, and A. Levechenko, "A 3D Monte Carlo analysis of the role of dyadic space geometry in spark generation," *Biophys. J.*, vol. 90, no. 6, pp. 1999 – 2014, 2006.

[32] A. J. Tanskanen, J. L. Greenstein, A. Chen, S. X. Sun, and R. L. Winslow, "Protein geometry and placement in the cardiac dyad influence macroscopic properties of calcium-induced calcium release," *Biophys. J.*, vol. 92, no. 10, pp. 3379–3396, 2007.

[33] J. Hake and G. T. Lines, "Stochastic binding of Ca^{2+} ions in the dyadic cleft; continuous versus random walk description of diffusion," *Biophys. J.*, vol. 94, pp. 4184–4201, 2008.

[34] J. Hake, A. G. Edwards, Z. Yu, P. M. Kekenes-Huskey, A. P. Michailova, J. A. McCammon, M. J. Holst, M. Hoshijima, and A. D. McCulloch, "Modelling cardiac calcium sparks in a three-dimensional reconstruction of a calcium release unit," *J. Physiol.*, vol. 590, pp. 4403–4422, 2012.

[35] L. Cleemann, W. Wang, and M. Morad, "Two-dimensional confocal images of organization, density, and gating of focal Ca^{2+} release sites in rat cardiac myocytes," *Proc. Natl. Acad. Sci. U.S.A.*, vol. 95, p. 10984 10989, 1998.

[36] A. J. Tanskanen, J. L. Greenstein, B. O'Rourke, and R. L. Winslow, "The role of stochastic and modal gating of cardiac L-type Ca^{2+} channels on early after-depolarizations," *Biophys. J.*, vol. 88, pp. 85–95, 2005.

[37] G. W. Dorn II, "Mitochondrial dynamics in heart disease," *BBA - Mol. Cell. Res.*, vol. 1, pp. 233 – 341, 2013.

[38] D. M. Bers, "Cardiac excitation-contraction coupling," *Nature*, vol. 415, pp. 198 – 205, 2002.

[39] I. M. A. Wolf and A. H. Guse, "Ca^{2+} microdomains in t-lymphocytes," *Front. Oncol.*, vol. 7, pp. 1 – 11, 2017.

[40] D. M. Barry and J. M. Nerbonne, "Myocardial potassium channels: electrophysiological and molceular diversity," *J. Theor. Biol.*, vol. 58, pp. 363 – 394, 1996.

[41] H. Kasai, A. Yao, T. Oyama, H. Hasegawa, H. Akazawa, H. Toko, T. Nagai, K. Kinugawa, O. Kohmoto, K. Maruyama, and T. Takahashi, "Direct measurement of Ca^{2+} concentration in the SR of living cardiac myocytes," *Biochem. and Biophys. Res. Com.*, vol. 314, pp. 1014 – 1020, 2004.

[42] K. D. Philipson and D. A. Nicoll, "Sodium calcium exchange: A molecular perspective," *Ann. Rev. Phys.*, vol. 62, pp. 111 – 133, 2000.

[43] L. Chu, J. L. Greenstein, and R. L. Winslow, "Modeling Na^{2+}-Ca^{2+} exchange in the heart: Allosteric activation, spatial localization, sparks and excitation-contraction coupling," *J. Mol. Cell. Cardiol.*, vol. 99, pp. 174 – 187, 2016.

[44] T. S. Luongo, J. P. Lambert, A. Yuan, X. Zhang, P. Gross, J. Song, S. Shanmughapriya, E. Gao, M. Jain, S. R. Houser, and W. J. Koch, "The mitochondrial calcium uniporter matches energetic supply with cardiac workload during stress and modulates permeabitlity transition," *Cell Reports*, vol. 12, pp. 15 – 22, 2015.

[45] V. Lukyanenko, A. Chikando, and W. J. Lederer, "Mitochondria in cardiomyocyte Ca^{2+} signaling," *Int. J. Biochem. Cell. Biol.*, vol. 41, pp. 1957 – 71, 2009.

[46] G. S. B. Williams, L. Boyman, A. c. Chikando, R. J. Khairallah, and W. J. Lederer, "Mitochondrial calcium uptake," *PNAS*, vol. 110, pp. 19479 – 10486, 2013.

[47] C. Franzini-Armstrong, "ER-mitochondria communication. How privileged?," *Physiol.*, vol. 22, pp. 261 – 268, 2007.

[48] R. T. Dirksen, "Sarcoplasmic reticulum-mitochondrial "through-space" coupling in skeletal muscle," *Appl. Physiol. Nutr. Metab.*, vol. 34, pp. 389 – 395, 2009.

[49] E. J. Griffiths and G. A. Rutter, "Mitochondrial calcium as a key regulator of mitochondrial atp production in mammalian cells," *BBA*, vol. 1787, pp. 1324 – 1333, 2009.

[50] G. S. B. Williams, G. D. Smith, E. A. Sobie, and M. S. Jafri, "Models of cardiac excitation-contraction coupling in ventricular myocytes," *Math. Biosc.*, vol. 226, pp. 1 – 15, 2010.

[51] A. Hodgkin and A. Huxley, "The components of membrane conductance in the giant axon of loligo," *J. Physiol.*, vol. 116, pp. 473–496, 1952.

[52] D. Noble, "A modification of the Hodgkin-Huxley equations applicable to purkinje fibre action and pace-maker potentials," *J. Physiol.*, vol. 160, pp. 317–352, 1962.

[53] G. W. Beeler and H. Reuter, "Reconstruction of the action potential of ventricular myocardial fibres," *J. Physiol.*, vol. 268, pp. 177 –210, 1977.

[54] R. E. McAllister, D. Noble, and R. W. Tsien, "Reconstruction of electrical activity of cardiac Purkinje fibres," *J. Physiol.*, vol. 251, pp. 1– 59, 1975.

[55] D. DiFrancesco and D. Noble, "A model of cardiac electricial activity incorporating ionic pumps and concentration changes," *Phil. trans. R. Soc. Lond. B. Biol. Sci*, vol. 307, pp. 353 – 398, 1985.

[56] A. Fabiato, "Time and calcium dependence of activation and inactivation of calcium-induced release of calcium from the sarcoplasmic reticulum of a skinned canine cardiac purkinje cell," *J. Gen. Physiol.*, vol. 85, pp. 247–289, 1985.

[57] C. H. Luo and Y. Rudy, "A model of the ventricular cardiac action potential: depolarization, repolarization, and their interaction," *Circ. Res.*, vol. 68, pp. 1501–1526, 1991.

[58] C. H. Luo and Y. Rudy, "A dynamic model of the cardiac ventricular action potential. I. simulations of ionic currents and concentration changes.," *Circ. Res.*, vol. 74, pp. 1071–1096, 1994.

[59] C. H. Luo and Y. Rudy, "A dynamic model of the cardiac ventricular action potential. II. afterdepolarizations, triggered activity, and potentiation," *Circ. Res.*, vol. 74, pp. 1097–1113, 1994.

[60] M. S. Jafri, J. J. Rice, and R. L. Winslow, "Cardiac Ca^{2+} dynamics: the role of rynaodine receptor adaptation and sarcoplasmic reticulum load," *Biophys. J.*, vol. 74, pp. 1149 – 1168, 1998.

[61] R. L. Winslow, J. Rice, S. Jafri, E. Marbán, and B. O'Rouke, "Mechanisms of altered excitation-contraction coupling in canine tachycardia-induced heart failure, II: model studies," *Circ. Res.*, vol. 84, pp. 571 – 86, 1999.

[62] G. A. Langer and A. Peskoff, "Calcium concentration and movement in the diadic cleft of the ventricular cell," *Biophys. J.*, vol. 70, pp. 1169 – 1182, 1996.

[63] C. Soeller and M. B. Cannell, "Numerical simulation of local calcium movements during L-type calcium channel gating in the cardiac diad," *Biophys. J.*, vol. 73, pp. 97 – 111, 1997.

[64] V. E. Bondarenko, G. P. Szigeti, G. C. Bett, S. J. Kim, and R. Rasmusson, "Computer model of action potential of mouse ventricular myocytes.," *Am. J. Physiol. Heart Circ. Physiol.*, vol. 287, pp. 1378 – 1403, 2004.

[65] S. Pandit, R. Clark, W. R. Giles, and S. Demir, "A mathematical model of action potential heterogeneity in adult rat left ventricular myocytes," *Biophys. J.*, vol. 81, pp. 3029 – 3051, 2001.

[66] T. R. Shannon, F. Wang, J. Puglisi, C. Weber, and D. M. Bers, "A mathematical treatment of integrated Ca dynamics within the ventricular myocyte," *Biophys. J.*, vol. 87, pp. 3351 – 3371, 2004.

[67] G. Smith, J. Keizer, M. Stern, W. Lederer, and H. Cheng, "A simple numerical model of calcium spark formation and detection in cardiac myocytes," *Biophys. J.*, vol. 75, pp. 15 – 32, 1998.

[68] E. A. Sobie, K. W. Dilly, C. J. dos Dantos, W. J. Lederer, and M. S. Jafri, "Termination of cardiac Ca^{2+} sparks: an investigative mathematical model of calcium-induced calcium release," *Biophys. J.*, vol. 83, pp. 59 – 78, 2002.

[69] L. Izu, J. Mauban, C. Balke, and W. Wier, "Large currents generate cardiac Ca^{2+} sparks," *Biophys. J.*, vol. 80, pp. 88 – 102, 2001.

[70] G. W. Dorn II and T. Force, "Protein kinase cascades in the regulation of cardiac hyperthrophy," *J. Clin. Invest.*, vol. 115, pp. 527 – 537, 2005.

[71] X. Chen., L. Guo, J. Kang, Y. Huo, S. Wand, and W. Tan, "Calcium waves initiating from the anomalous subdiffusive calcium sparks," *J. R. Soc. Interface*, vol. 11, pp. 1 – 10, 2014.

[72] P. D. Mullins and V. E. Bondarenko, "A mathematical model of mouse ventricular myocyte contraction," *PLoS ONE*, vol. 8, pp. 1 – 15, 2013.

[73] J. J. Saucerman, L. L. Brunton, A. P. Michailova, and A. D. McCulloch, "Modeling beta-adrenergic control of cardiac myocyte contractility in silico," *J. Biol. Chem.*, vol. 278, pp. 47997 – 48003, 2003.

[74] S. Cortassa, M. A. Aon, E. Marbán, R. L. Winslow, and B. O'Rouke, "An integrated model of cardiac mitochondrial energy metabolism and calcium dynamics," *Biophys. J.*, vol. 84, pp. 2734 – 2755, 2003.

[75] J. L. Greenstein and R. L. Winslow, "Integrative systems models of cardiac excitation contraction coupling," *Circ. Res.*, vol. 108, pp. 70 – 84, 2011.

[76] R. Hinch, J. L. Greenstein, A. J. Tanskanen, L. Xu, and R. L. Winslow, "A simplified local control model of calcium-induced calcium release in cardiac ventricular myocytes," *Biophys. J.*, vol. 87, pp. 3723–3736, 2004.

[77] J. L. Greenstein, R. Hinch, and R. Winslow, "Mechanisms of excitation-contraction coupling in an integrative model of the cardiac ventricular myocyte," *Biophys. J.*, vol. 90, pp. 77 – 91, 2006.

[78] G. S. B. Williams, M. A. Huertas, E. A. Sobie, M. S. Jafri, and G. D. Smith, "A probability density approach to modeling local control of calcium-induced calcium release in cardiac myocytes," *Biophys. J.*, vol. 92, pp. 2311 – 2328, 2007.

[79] G. S. B. Williams, M. A. Huearts, E. A. Sobie, M. S. Jafri, and G. D. Smith, "Moment closure for local control models of calcium-induced calcium release in cardiac myocytes," *Biophys. J.*, vol. 95, pp. 1689 – 1703, 2008.

[80] A. Hatano, J. Okada, T. Washio, T. Hisada, and S. Sugiura, "A three-dimensional simulation model of cardiomyocyte integrating excitation-contraction coupling and metabolism," *Biophys. J.*, vol. 101, pp. 2601 – 2610, 2011.

[81] M. Nivala, Z. Song, J. N. Weiss, and Z. Qu, "T-tubule disruption promotes calcium alternans in failing ventricular myocytes: Mechanistic insights from computational modeling," *J. Mol. Cell. Cardiol.*, vol. 79, pp. 32 – 41, 2015.

[82] A. Hatano, J. Okada, T. Hisada, and S. Sugiura, "Critical role of cardiac t-tubule system for the maintenance of contractile function revealed by a 3D integrated model of cardiomyocytes," *J. Biomech.*, vol. 45, pp. 815 – 823, 2012.

[83] J. G. Restrepo, J. N. Weiss, and A. Karma, "Calsequestrin-mediated mechanism for cellular calcium transient alternans," *Biophys. J.*, vol. 95, pp. 3767 – 3789, 2008.

[84] J. G. Restrepo and A. Karma, "Spatiotemporal intracellular calcium dynamics during cardiac alternans," *Chaos*, vol. 19, p. 037115, 2009.

[85] G. S. Williams, A. C. Chikando, H. T. Tuan, E. A. Sobie, W. J. Lederer, and M. S. Jafri, "Dynamics of calcium sparks and calcium leak in the heart," *Biophys. J.*, vol. 101, pp. 1287 – 1296, 2011.

[86] E. R. Higgins, P. Goel, J. L. Puglisi, D. M. Bers, M. Cannell, and J. Sneyd, "Modeling calcium microdomains using homogenisation," *J. Theor. Biol.*, vol. 247, pp. 623 – 644, 2007.

[87] T. Schendel and M. Falcke, "Efficient and detailed model of the local Ca^{2+} release unit in the ventricular cardiac myocyte," *Genome Inform.*, vol. 22, pp. 142 – 155, 2010.

[88] M. D. Stern, E. Rios, and V. A. Maltsev, "Life and death of a cardiac calcium spark," *J. Gen. Physiol.*, vol. 142, pp. 257– 274, 2013.

[89] R. Rovetti, X. Cui, A. Garfinkel, J. N. Weiss, and Z. Qu, "Spark-induced sparks as a mechanism of intracellular calcium alternans in cardiac myocytes," *Circ. Res.*, vol. 106, pp. 1582 – 1591, 2010.

[90] N. Gaur and Y. Rudy, "Multiscale modeling of calcium cycling in cardiac ventricular myocyte: macroscopic consequences of microscopic dyadic function," *Biophys. J.*, vol. 100, pp. 2904 – 2912, 2011.

[91] A. P. Wescott, M. S. Jafri, W. Lederer, and G. S. B. Williams, "Ryanodine receptor sensitivity governs the stability and synchrony of local calcium release during cardiac excitation-contraction coupling," *J. Mol. Cell. Cardiol.*, vol. 92, pp. 82 – 92, 2016.

[92] D. Sato, T. R. Shannon, and D. M. Bers, "Sarcoplasmic reticulum structure and functional properties that promote long-lasting calcium sparks," *Biophys. J.*, vol. 110, pp. 382 – 390, 2016.

[93] V. Rajagopal, G. Bass, C. G. Walker, D. J. Crossman, A. Petzer, A. Hickey, I. Siekmann, M. Hoshijima, M. H. Ellisman, E. J. Crampin, and C. Soeller, "Examination of the effects of heterogeneous organization of ryr clusters, myofibrils and mitochondria on Ca^{2+} release patterns in cardiomyocytes," *PLoS Comput. Biol.*, vol. 110, pp. 1 – 31, 2015.

[94] J. Keener and J. Sneyd, *Mathematical Physiology.* New York: Springer, 1998.

[95] T. Schendel, R. Thul, J. Sneyd, and M. Falcke, "How does the ryanodine receptor in the ventricular myocyte wake up: by a single or by multiple open L-type Ca^{2+} channels?," *Eur. Biophys. J.*, vol. 41, pp. 27 – 39, 2012.

[96] C. Soeller, D. Crossman, R. Gilbert, and M. B. Cannell, "Analysis of ryanodine receptor clusters in rat and human cardiac myocytes," *PNAS*, vol. 104, pp. 14958 –14963, 2007.

[97] C. Soeller and D. Baddeley, "Super-resolution imaging of EC coupling protein distribution in the heart," *J. Mol. Cell. Card.*, vol. 58, pp. 32 – 40, 2013.

[98] W. Xie, D. X. Brochet, S. Wei, X. Wang, and H. Cheng, "Deciphering ryanodine receptor array operation in cardiac myocytes," *J. Gen. Physiol.*, vol. 136, no. 2, pp. 129 – 133, 2010.

[99] D. M. Bers and V. M. Stiffel, "Ratio of ryanodine to dihyadropyridine receptors in cardiac and skeletal muscle and implications for E-C coupling," *Am. J. Physiol.*, vol. 264, pp. C1587 – C1593, 1993.

[100] Y. Hou, I. Jayasinghe, D. J. Crossman, and C. Baddeley, D. Soeller, "Nanoscale analysis of ryanodine receptor clusters in dyadic couplings of rat cardiac myocytes," *J. of Mol. and Cell. Card.*, vol. 80, pp. 45 – 55, 2015.

[101] O. Häggström, *Finite markov chains and algorithmic applications*. London Mathematical Society: Cambridge Uni. Press, 2002.

[102] A. Mahajan, Y. Shiferaw, D. Sato, A. Baher, R. Olcese, L. H. Xie, M. J. Yang, P. S. Chen, J. G. Restrepo, A. Karma, A. Garfinkel, Z. Qu, and J. N. Weiss, "CellML of the Mahjan 2008 Action Potential Model." `https://models.cellml.org/workspace/mahajan_shiferaw_sato_baher_olcese_xie_yang_chen_restrepo_karma_garfinkel_qu_weiss_2008`, 2008. Accessed: 2015-7-13.

[103] D. T. Gillespie, "A genereal method for numerically simulating the stoachastic time evolution of coupled chemical reactions," *J. Comp. Physics*, vol. 22, pp. 403 – 434, 1976.

[104] C. Soeller and M. B. Cannell, "Numerical simulation of local calcium movements during L-type calcium channel gating in the cardiac diad," *Biophys. J.*, vol. 73, pp. 97–111, 1997.

[105] A. Takahashi, P. Camacho, J. D. Lechleiter, and B. Herman, "Measurement of intracellular calcium," *Physiol. Rev.*, vol. 79, no. 4, pp. 1089–1125, 1999.

[106] G. Magnus and J. Keizer, "Minimal model of beta-cell mitochondrial Ca^{2+} handling," *Am. J. Physiol.*, vol. 273, pp. C717 – C733, 1997.

[107] J. Lang, *Adaptive Multilevel Solution of Nonlinear Parabolic PDE Systems*, vol. 16 of *Lecture Notes in Computational Science and Engineering*. Springer, Berlin, 2001.

[108] C. Nagaiah, S. Rüdiger, G. Warnecke, and M. Falcke, "Adaptive space and time numerical simulation of reaction-diffusion models for intracellular calcium dynamics," *Appl. Math. and Comp.*, vol. 218, no. 20, pp. 10194 – 10210, 2012.

[109] N. Chamakuri and S. Rüdiger, "Whole-cell simulations of hybrid stochastic and deterministic calcium dynamics in 3D geometry," *J. Comp. Interdis. Sci.*, vol. 3, no. 1-2, pp. 3–18, 2012.

[110] P. Bastian, M. Blatt, A. Dedner, C. Engwer, R. Klöfkorn, R. Kornhuber, M. Ohlberger, and O. Sander, "A generic grid interface for parallel and adaptive scientific computing. Part II: implementation and tests in DUNE," *Computing*, vol. 82, no. 2, pp. 121 – 138, 2008.

[111] H. A. van der Vorst, "Bi-CGSTAB: A fast and smoothly converging variant of bi-cg for the solution of nonsymmetric linear systems," *SIAM J. Sci. Stat. Comput.*, vol. 13, pp. 631–644, 1994.

[112] J. T. Lanner, D. K. Georgiou, A. D. Joshi, and S. L. Hamilton, "Ryanodine receptors: structure, expression, molecular details, and function in calcium release," *CSH Persp. in Biol.*, vol. 2, pp. 1 – 21, 2010.

[113] B. N. Walpoth and B. Erman, "Regulation of ryanodine receptor RyR2 by protein-protein interactions: prediction of a PKA binding site on the N-terminal domain of RyR2 and its relation to disease causing mutations," *F1000Res*, vol. 4, pp. 1 – 9, 2015.

[114] M. Fill and J. A. Copello, "Ryanodine receptor calcium release channels," *Physiol. Rev.*, vol. 82, pp. 893 – 922, 2002.

[115] D. R. Laver, C. H. Kong, M. Imtiaz, and M. Cannell, "Termination of calcium-induced calcium release by induction decay: an emergent property of stochastic channel gating and molecular scale architecture," *J. Mol. Cell. Cardiol.*, vol. 83, pp. 59 – 78, 2002.

[116] H. DeRemigio and G. D. Smith, "The dynamics of stoachstic attrition viewed as an absorption time on terminating Markov chain," *Cell Calcium*, vol. 38, pp. 73 – 86, 2005.

[117] N. F. Otani and R. F. Gilmour, "Memory models for the electrical properties of local cardiac systems," *J. Theor. Biol.*, vol. 187, no. 3, pp. 409–436, 1997.

[118] C. R. Weber, V. Piacentino, K. S. Ginsburg, S. R. Houser, and D. M. Bers, "Na^+-Ca^{2+} exchange current and submembrane $[Ca^{2+}]$ during the cardiac action potential," *Circ. Res.*, vol. 90, pp. 182 – 189, 2002.

[119] L. Boyman, A. C. Chikando, G. S. Williams, R. J. Khairallah, S. Kettlewell, C. W. Ward, G. L. Smith, J. P. Kao, and W. J. Lederer, "Calcium movement in cardiac mitochondria," *Biophys. J.*, vol. 107, no. 6, pp. 1289 – 1301, 2014.

[120] C. Maack, S. Cortassa, M. A. Aon, A. N. Ganesan, T. Liu, and B. O'Rourke, "Elevated cytosolic Na^+ decreases mitochondrial Ca^{2+} uptake during excitation-contraction coupling and impairs energetic adaptation in cardiac myocytes," *Circ. Res.*, vol. 99, no. 2, pp. 172 – 182, 2006.

[121] R. Thul and M. Falcke, "Release currents of IP_3 receptor channel clusters and concentration profiles," *Biophys.J.*, vol. 86, pp. 2660 – 2673, 2004.

[122] K. Bentele and M. Falcke, "Quasi-steady approximation for ion channel currents," *Biophys. J.*, vol. 93, no. 8, pp. 2597 – 2608, 2007.

[123] N. S. Torres, F. B. Sachse, L. T. Izu, J. I. Goldhaber, K. W. Spitzer, and J. H. Bridge, "A modified local control model for Ca^{2+} transients in cardiomyocytes: junctional flux is accompanied by release from adjacent non-junctional RyRs," *J. Mol. Cell. Cardiol.*, vol. 68, pp. 1 – 11, 2014.

[124] I. D. Jayasinghe, M. B. Cannell, and C. Soeller, "Organization of ryanodine receptors, transverse tubules, and sodium-calcium exchanger in rat myocytes," *Biophys. J.*, vol. 97, pp. 2664–2673, 2009.

[125] D. R. L. Scriven, P. Dan, and E. D. W. Moore, "Distribution of proteins implicated in excitation-contraction coupling in rat ventricular myocytes," *Biophys. J.*, vol. 79, pp. 2682–2691, 2000.

[126] D. R. L. Scriven, A. Klimek, K. L. Lee, and E. D. W. Moore, "The molecular architecture of calcium microdomains in rat cardiomyocytes," *Ann. N.Y. Acad. Sci.*, vol. 976, pp. 488–499, 2002.

[127] D. R. Scriven and E. D. Moore, "Ca^{2+} channel and Na^{+}/Ca^{2+} exchange localization in cardiac myocytes," *J. of Mol. and Cell. Cardiol.*, vol. 58, pp. 22–31, 2013.

[128] S. Wray and W. Burdyga, "Sarcoplasmic reticulum function in smooth musle," *Physiol. Rev.*, vol. 90, pp. 113 – 178, 2010.

[129] G. A. Jamieson and D. M. Robinson, *Mammalian cell membranes: Volume 4, Surface Membranes of specific types.* The Butterworth Group, London, Boston: Elsevier Ltd., 1977.

[130] M. Periasamy, P. Bhupathy, and G. J. Babu, "Regulation of sarcoplasmic reticulum Ca^{2+} ATPase pump expression and its relevance to cardiac muscle physiology and pathology," *Cardiovas. Res.*, vol. 77, pp. 265 – 273, 2008.

[131] E. F. Bode, S. J. Briston, C. L. Overend, S. C. O'Neill, A. W. Trafford, and D. Eisner, "Changes of SERCA activity have only modest effects on sarcoplasmic reticulum Ca^{2+} content in rat ventricular myocytes," *J. Physiol.*, vol. 589, pp. 4723 – 4729, 2011.

[132] J. T. Koivumäki, J. Takalo, T. Korhonen, P. Tavi, and M. Weckström, "Modelling sarcoplasmic reticulum calcium ATPase and its regulation in cardiac myocytes," *Phil. Trans. R. Soc. A*, vol. 367, pp. 2181 – 2202, 2009.

[133] I. Altshuler, J. J. Vaillant, S. Xu, and M. E. Cristescu, "The evolutionary history of sarco(endo)plasmic caclium ATPas (SERCA)," *PLoS One*, vol. 7, pp. 1 – 6, 2012.

[134] E. Bovo, P. P. de Tombe, and A. V. Zima, "The role of dyadic organization in regulation of sarcplasmic reticulum Ca^{2+} handling during rest in rabbit ventricular myocytes," *Biophys. J.*, vol. 106, pp. 1902 – 1909, 2014.

[135] U. Schmidt, R. J. Hajjar, D. Lebeche, A. Doaye, and J. K. Gwathmey, "Human heart failure: cAMP stimulation of SR Ca^{2+}-ATPase activity and phosphorylation level of phsospholamban," *Am. J. Physiol.*, vol. 277, pp. H474 – 80, 1999.

[136] A. El-Armouche, T. Pamminger, D. Ditz, O. Zolk, and T. Eschenhagen, "Decreased protein and physpohorylation level of the protein phosphatase inhibitor-1 in failing human hearts," *Cardiovasc. Res.*, vol. 61, pp. 87 – 93, 2004.

[137] P. Bhupathy, G. J. Babu, and M. Periasamy, "Sarcolipin and phospholamban as regulators of cardiac sarcoplasmic reticulum Ca^{2+} ATPase," *J. Mol. Cell. Cardiol.*, vol. 42, pp. 903 – 911, 2009.

[138] N. A. Beard, D. R. Laver, and A. F. Dulhunty, "Calsequestrin and the calcium release channel of skelatal and cardiac muscle," *Progress in Biophys. and Mol. Biol.*, vol. 85, pp. 33 – 69, 2004.

[139] R. D. Mitchell, H. K. Simmermann, and L. R. Jones, "Ca^{2+} binding effects on protein conformation and protein interactions of canine cardiac calsequestrin," *J. Biol. Chem*, vol. 263, pp. 1376 – 1381, 1988.

[140] A. Herzog, C. Szegedi, I. Jona, F. W. Herberg, and M. Varsanyi, "Surface plasmon resonance studies prove the interaction of skeletal reticular Ca^{2+} release channel/ryanodine receptor with calsequestrin," *FEBS Lett.*, vol. 472, pp. 73 – 77, 2000.

[141] L. Zhang, J. Kelley, G. Schmeisser, Y. M. Y.M. Kobyashi, and L. R. Jones, "Complex formation between junctin, triadin, calsequestrin, and ryanodine receptor. Proteins of the cardiac junctional sarcoplasmic reticulum membrane," *J. Biol. Chem*, vol. 272, pp. 23389 – 23397, 1997.

[142] D. Terenyev, S. Viatchenko-Karpinski, H. H. Valdivia, A. Escobar, and S. Györke, "Luminal Ca^{2+} controls termination and refractory behavior of Ca^{2+}-induced Ca^{2+} release in cardiac myocytes," *Circ. Res.*, vol. 91, pp. 414 – 420, 2002.

[143] T. Guo, X. Ai, T. R. Shannon, S. M. Pogwuzd, and D. M. Bers, "IntraSarcoplasmic reticulum free $[Ca^{2+}]$ and buffering in arrythmogenic failing rabbit heart," *Circ. Res.*, vol. 120, pp. 1 – 9, 2007.

[144] J. W. M. Bassani, W. Yuan, and D. M. Bers, "Fractional SR Ca release is regulated by trigger Ca and SR content in cardiac myocytes," *Am. J. Physiol.*, vol. 268, pp. C1313 – 9, 1995.

[145] T. R. Shannon, K. S. Ginsburg, and D. M. Bers, "Reverse mode of the sarcoplasmic reticulum calcium pump and load-dependent cytosolic calcium decline in voltage-clamped cardiac ventricular myocytes," *Biophys. J.*, vol. 78, pp. 322 – 333, 2000.

[146] Y. Shiferaw, M. A. Watanabe, A. Garfinkel, J. N. Weiss, and A. Karma, "Model of intracullular calcium cycling in ventricular myoctes," *Biophys. J.*, vol. 85, pp. 3666–3686, 2003.

[147] M. Harada, Y. Tsuji, Y. S. Ishiguro, H. Takanari, Y. Okuno, Y. Inden, H. Honjo, J.-K. Lee, T. Murohara, I. Sakuma, K. Kamiya, and I. Kodama, "Rate-dependent shortening of action potential duration increases ventricular vulnerability in failing rabbit heart," *Am. J. of Physiol.*, vol. 300, pp. H565 – H573, 2011.

[148] J. I. Goldhaber, L.-H. Xie, T. Duong, C. Motter, K. Khuu, and J. N. Weiss, "Action potential duration restitution and alternans in rabbit ventricular myocytes," *Circ. Res.*, vol. 96, pp. 459 – 466, 2003.

[149] S. Kettlewell, P. Cabrero, S. A. Nicklin, J. A. T. Dow, S. Davies, and G. L. Smith, "Changes of intra-mitochondrial Ca^{2+} in adult ventricular cardiomyocytes examined using novel fluorescent Ca^{2+} indicator targeted to mitochondria," *J. of Mol. and Cell. Card.*, vol. 46, pp. 891 – 901, 2009.

[150] E. A. Sobie and W. J. Lederer, "Dynamic local changes in sarcoplasmatic reticulum calcium: physiological and pathological roles," *J. Mol. Cell. Cardiol.*, vol. 52, pp. 304–311, 2012.

[151] T. R. Shannon, K. S. Ginsburg, and D. M. Bers, "Potentiation of fractional sarcoplasmic reticulum calcium release by total and free intra-sarcoplasmic reticulum calcium concentration," *Biophys. J.*, vol. 78, pp. 334 – 343, 2000.

[152] C. J. Fravre, J. Schrenzel, J. Jacquet, D. P. Lew, and K. KRause, "Highly supralinear feedback inhibition of Ca^{2+} uptake by the Ca^{2+} load of intraceullular stores," *J. Biol. Chem*, vol. 271, pp. 14925 – 14930, 1996.

[153] T. R. Shannon, G. Chu, E. G. Kranias, and D. M. Bers, "Phospholamban decreases the energetic efficiency of the sarcoplasmic reticulum Ca pump," *J. Biol. Chem*, vol. 276, pp. 7195 – 7201, 2001.

[154] J. Sneyd, K. Tsaneva-Atanasova, J. I. Bruce, S. V. Straub, D. R. Giovannucci, and D. Yule, "A model of calcium waves in pancreatic and parotid acinar cells," *Biophys. J.*, vol. 85, pp. 1392 – 1405, 2003.

[155] E. R. Higgins, M. Cannell, and J. Sneyd, "A buffering SERCA pump in models of calcium dynamics," *Biophys. J.*, vol. 91, pp. 141 – 163, 2006.

[156] D. Terenyev, Z. Kubalova, G. Valle, A. Nori, S. Vedamoorthyrao, R. Terenyeva, S. Viatchenko-Karpinski, D. M. Bers, S. C. Williams, P. Volpe, and S. Gyroke, "Modulation of SR Ca release by luminal Ca and calsequestrin in cardiac myocytes: effects of CASQ2 mutations linked to sudden cardiac death," *Biophys. J.*, vol. 95, pp. 2037 – 2048, 2008.

[157] G. Meissner, "Isolation and characterization of two types of sarcoplasmic reticulum vesicles," *BBA*, vol. 389, pp. 51 – 68, 1975.

[158] A. O. Jorgensen, A. Kalnins, and MacLennan, "Localization of sarcoplasmic reticulum proteins in rat skeletal muscle by immunofluorescence," *J. Cell. Biology*, vol. 80, pp. 372 – 384, 1979.

[159] M. P. Blaustein and W. J. Lederer, "Sodium/calcium exchange: Its physiological implications," *Physiol. Rev.*, vol. 79, pp. 763–854, 1999.

[160] F. Marinelli, L. Almagor, R. Hiller, M. Giladi, D. Khananshvili, and J. D. Faraldo-Gómez, "Sodium recognition by the Na^+/Ca^{2+} exchanger in the outward-facing conformation," *PNAS*, vol. 111, pp. E5354 – E5362, 2014.

[161] T. M. Kang and D. W. Hilgemann, "Multiple transport modes of the cardiac Na^+/Ca^{2+} exchanger," *Nature*, vol. 427, pp. 544 – 548, 2004.

[162] X. Ren and K. D. Phlipson, "The topology of the cardiac Na^+/Ca^{2+} exchanger NCX1," *J. Mol. Cell. Cardiol.*, vol. 57, pp. 68 – 71, 2013.

[163] L. Y. Michel, S. Verkaart, W. J. H. Koopman, P. H. G. M. Willems, J. G. J. Hoenderop, and R. J. M. Bindels, "Function and regulation of the Na^+-Ca^2 exchanger NCX3 splice variants in brain and skeletal muscle," *J. Bio. Chem.*, vol. 289, pp. 11293 – 11303, 2014.

[164] M. Brini and E. Carafoli, "The plasma membrane Ca^{2+} ATPase and the plasma membrane sodium calcium exchanger cooperate in the regulation of cell calcium," *CCH Persp. in Biol.*, vol. 3, pp. 1 –17, 2011.

[165] D. M. Bers, "Calcium cycling and signaling in cardiac myocytes," *Ann. Rev. Physiol.*, vol. 70, pp. 23–49, 2008.

[166] T. Iwamoto, Y. Watanabe, S. Kita, and M. P. Blaustein, "Na^+/Ca^{2+} exchange inhibitors: a new class of calcium regulators," *Cardiovasc. Hematol. Disord. Drug Targets*, vol. 7, pp. 188 – 198, 2007.

[167] H. Tanaka, K. Nishimaru, T. Aikawa, W. Hirayama, Y. Tanaka, and K. Shigenobu, "Effect of SEA0400, a novel inhibitor of sodium-calcium exchanger, on myocardial ionic currents," *Brit. J. Pharmacol.*, vol. 135, pp. 1096 – 1100, 2002.

[168] G. Barrientos, D. D. Bose, W. Feng, I. Padilla, and I. N. Padilla, "The Na^+/Ca^{2+} exchange inhibitor 2-(2-(4-(4-nitrobenzyloxy)phenyl)ethyl)isothiourea methanesulfonate (KB-R7943) also blocks ryandoine receptors type 1 (RyR1) and type 2 (RyR2) channels," *Mol. Pharmacol.*, vol. 76, pp. 560 – 568, 2009.

[169] M. Ottolia, N. Torres, J. J. Bridge, K. D. Philipson, and J. I. Goldhaber, "Na/Ca exchange and contraction of the heart," *J. Mol. Cell. Cardiol.*, vol. 61, pp. 28 – 33, 2013.

[170] M. J. Shattock, M. Ottolia, D. M. Bers, M. P. Blaustein, A. Boguslavskyi, J. Bossuyt, J. H. B. Bridge, Y. Chen-Izu, C. E. Clancy, A. Edwards, J. Goldhaber, J. Kaplan, J. B. Lingrel, D. Pavlovic, K. Philipson, K. R. Sipido, and Z.-J. Xie, "Na^+/Ca^{2+} exchange and Na^+/K^+-ATPase in the heart," *J. Physiol.*, vol. 593, pp. 1361 – 1382, 2015.

[171] J. W. Bassani, R. A. Bassani, and D. M. Bers, "Relaxation in rabbit and rat cardiac cells: species-dependent differences in cellular mechanisms," *J. Physiol.*, vol. 476, pp. 279 – 293, 1994.

[172] C. Pott, K. D. Philipson, and J. I. Goldhaber, "Excitation-contraction coupling in Na^+-Ca^{2+} exchanger knockout mice reduced transsarcolemmal Ca^{2+} flux," *Circ. Res.*, vol. 97, pp. 1288 – 1295, 2005.

[173] K. R. Sipido, P. G. Volders, M. A. Vos, and F. Verdonck, "Altered Na/Ca exchange activity in cardiac hyperthrophy and heart failure: a new target for therapy?," *Cardiovasc. Res.*, vol. 53, pp. 782 – 805, 2002.

[174] C. Lee, N. S. Dhalla, and L. V. Hryshko, "Therapeutic potential of novel Na^+/Ca^{2+} exchange inhibitors in attenuating ischemia-reperfusion injury," *Can. J. Cardiol.*, vol. 21, pp. 509 – 516, 2005.

[175] G. Antoons, R. Willems, and K. R. Sipido, "Alternative strategies in arrhythmia therapy: evaluation of Na/Ca exchange as an anti-arrhytmic target," *Pharmacol. Ther.*, vol. 134, pp. 26 – 42, 2012.

[176] W. J. Lederer, E. Niggli, and R. W. Hadle, "Sodium-calcium exchange in excitable cells: fuzzy space," *Science*, vol. 248, p. 283, 1990.

[177] P. Dan, E. Lin, J. Huang, P. Biln, and G. F. Tibbits, "Three-dimensional distribution of cardiac Na^+-Ca^{2+} exchanger and ryanodine receptor during development," *Biophys. J.*, vol. 93, pp. 2504 – 2518, 2007.

[178] S. Despa, F. Brette, C. H. Orchard, and D. Bers, "Na/Ca exchange and Na/K-ATPase function are equally concentrated in transeverse tubules of rat ventricular myocytes," *Biophys. J.*, vol. 85, pp. 3388 – 3396, 2003.

[179] K. Acsai, G. Antoons, L. Livshitz, Y. Rudy, and K. R. Sipido, "Microdomain [Ca^{2+}] near ryanodine receptors reported by L-type Ca^{2+} and Na^+/Ca^{2+} exchange currents," *J. Physiol.*, vol. 589, pp. 2569 – 2583, 2011.

[180] W. Wang, A. Landstrom, Q. Wang, M. L. Muncro, D. Beavers, M. J. Ackerman, C. Soeller, and X. H. Wehrens, "Reduced junctional Na^+/Ca^{2+}-exchanger activity contributes to sarcoplasmic reticulum Ca^{2+} leak in junctophilin-2-deficient mice," *Am. J. Physiol. Heart Circ. Physiol.*, vol. 307, pp. H1317 – H1326, 2014.

[181] E. A. Sobie, M. B. Cannell, and J. H. B. Bridge, "Allosteric activation of Na^+-Ca^{2+} exchanger by L-type Ca^{2+} current augments the trigger flux for SR Ca^{2+} release in ventricular myocytes," *Biophys. J.*, vol. 94, pp. L54 – L56, 2008.

[182] P. Neco, B. Rose, N. Huynh, R. Zhang, J. H. B. Bridge, K. D. Philipson, and J. I. Goldhaber, "Sodium-calcium exchange is essential for effective triggering of calcium release in mouse heart," *Biophys. J.*, vol. 99, pp. 755 – 764, 2010.

[183] R. Larbig, N. Torres, J. H. B. Bridge, J. I. Goldhaber, and K. D. Philipson, "Activation of reverse Na^+-Ca^{2+} exchange by the Na^+ current augments the cardiac Ca^{2+} transient: evidence from NCX knockout mice," *Biophys. J.*, vol. 588, pp. 3267 – 3276, 2010.

[184] Z. Su, K. Sugishita, M. Ritter, F. Li, K. W. Spitzer, and W. H. Barry, "The sodium pump modulates the influence of I_{Na} on $[Ca^{2+}]_i$ transients in mouse ventricular myocytes," *Biophys. J.*, vol. 80, pp. 1230 – 1237, 2001.

[185] S. E. Litwin, "Na-Ca exchange and the trigger for sarcoplasmic reticulum Ca release: studies in adult rabbit ventricular myocytes," *Biophys. J.*, vol. 75, pp. 359 – 371, 1998.

[186] J. A. Wasserstrom and A. M. Vites, "The role of Na^+-Ca^{2+} exchange in activation of excitation-contraction coupling in rat ventricular myocytes," *Biophys. J.*, vol. 493, pp. 529 – 542, 1996.

[187] C. Han, P. Tavi, and M. Weckström, "Role of Na^+-Ca^{2+} exchanger as an alternative trigger of CICR in mammalian cardiac myocytes," *Biophys. J.*, vol. 82, pp. 1483 – 1496, 2002.

[188] J. I. Goldhaber and K. D. Philipson, "Cardiac sodium-calcium exchange and efficient excitation-contraction coupling: Implications for heart disease," *Adv. Exp. Med. Biol.*, vol. 961, pp. 355 – 364, 2013.

[189] N. S. Torres, R. Larbig, A. Rock, J. I. Goldhaber, and J. H. Bridge, "Na^+ currents are required for efficient excitation-contraction coupling in rabbit ventricular myocytes: a possible contribution of neuronal Na^+ channels," *J. Physiol.*, vol. 588, pp. 4249 – 4260, 2010.

[190] K. R. Sipido, M. Maes, and F. Van de Werf, "Low efficiency of Ca^{2+} entry through the Na^+-Ca^{2+} exchanger as trigger for Ca^{2+} release from the sarcoplasmic reticulum. A comparison between L-type Ca^{2+} current and the reverse-mode Na^+-Ca^{2+} exchange," *Circ. Res.*, vol. 81, pp. 1034 – 1044, 1997.

[191] J. S. Sham, L. Cleeman, and M. Morad, "Gating of the cardiac Ca^{2+} release channel: the role of Na^+ current and Na^+-Ca^{2+} exchange," *Science*, vol. 255, pp. 850 – 853, 1992.

[192] R. A. Bouchard, R. B. Clark, and W. R. Giles, "Role of sodium-calcium exchange in activation of contraction in rat ventricle," *J. Physiol.*, vol. 472, pp. 391 – 413, 1993.

[193] J. I. Goldhaber, S. T. Lamp, D. O. Walter, A. Garfinkel, G. H. Furkumato, and J. N. Weiss, "Local regulation of the threshold for calcium sparks in rat ventricular myocytes: role of sodium-calcium exchange," *J. Physiol.*, vol. 520, pp. 431 – 438, 1999.

[194] D. Sato, S. Despa, and D. M. Bers, "Can the sodium-calcium exchanger initiate or suppress calcium sparks in cardiac myocytes?," *Biophys. J.*, vol. 102, pp. L31 –L33, 2012.

[195] A. Zahradníková, I. Valent, and I. Zahradník, "Frequency and release flux of calcium sparks in rat cardiac myocytes: a relation to RYR gating," *J. of Gen. Physiol.*, vol. 136, pp. 101 – 116, 2010.

[196] T. J. Hund and Y. Rudy, "Rate dependence and regulation of action potential and calcium transient in a canine cardiac ventricular cell model," *Circ.*, vol. 110, pp. 3168 – 3174, 2004.

[197] J. Fan and Z. Yu, "A univariate model of caclium release in the dyadic cleft of cardiac myocytes," *Conf. Proc. IEEE Eng. Med. Biol. Soc*, vol. 2009, pp. 4499 – 4503, 2009.

[198] A. W. Trafford, M. E. Diaz, S. C. O'Neill, and D. Eisner, "Comparison of subsarcolemmal and bulk calcium concentration during spontaneous calcium release in rat ventricular myocytes," *J. Physiol.*, vol. 488, pp. 577 – 586, 1995.

[199] K. H. ten Tusscher, D. Noble, P. J. Noble, and A. V. Panfilov, "A model for human ventricular tissue," *Am. J. Physiol. Heart Circ. Physiol.*, vol. 286, pp. 15763 – 1589, 2004.

[200] Z. Yang, C. Pascarel, D. S. Steele, K. Komukai, F. Brette, and C. H. Orchard, "Na^+-Ca^{2+} exchange activity is localized in the t-tubules of rat ventricular myocytes," *Cell. Biol.*, vol. 91, pp. 315 – 322, 2002.

[201] M. J. Thomas, I. Sjaastad, K. Andersen, P. J. Helm, J. A. Wasserstorm, O. M. Sejersted, and O. P. Ottersen, "Localization and function of the Na^+-Ca^{2+} exchanger in normal and detubulated rat cardiomyocytes," *J. Mol. Cell. Cardiol.*, vol. 35, pp. 1325 – 1337, 2003.

[202] D. A. Eisner and K. R. Sipido, "Sodium calcium exchange in the heart - necessity or luxury?," *Circ. Res.*, vol. 95, pp. 549 – 551, 2004.

[203] C. Pott, S. A. Henderson, J. I. Goldhaber, and K. D. Philipson, "Na^+/Ca^{2+} exchanger knockout mice - Plasticity of cardiac excitation-contraction coupling," *Ann. N.Y. Acad. Sci.*, vol. 1099, pp. 270 – 275, 2007.

[204] M. Ibrhaim, P. Kukadia, U. Siedlecka, J. E. Cartledge, M. Navaratnarajah, S. Tokar, C. von Doorn, V. T. Tsang, J. Gorelik, M. H. Yacoub, and C. M. Terracciano, "Cardiomyocyte Ca^{2+} handling and structure is regulared by degree and duration of mechanical load variation," *J. Cell. Mol. Med.*, vol. 12, pp. 2910 – 2918, 2012.

[205] L. Biesmans, N. Macquaide, F. R. Heinzel, v. Bito, G. L. Smith, and K. R. Sipido, "Subcellular heterogeneity of ryanodine receptor properties in ventricular myocytes with low t-tubule density," *PLoS ONE*, vol. 6, pp. 1 – 11, 2012.

[206] S. Guatimosim, C. Guatimosim, and L.-S. Song, "Imaging calcium sparks in cardiac myocytes," *Methods Mol. Biol.*, vol. 689, pp. 205 – 214, 2012.

[207] V. M. Shkryl and L. A. Blatter, "Ca^{2+} release events in cardiac myocytes up close: insights from fast confocal imaging," *PLoS ONE*, vol. 8, pp. 1 – 12, 2013.

[208] A. Mattiazi, M. Argenziano, Y. Aguilar-Sanches, G. Mazzocchi, and A. L. Escobar, "Ca^{2+} sparks and Ca^{2+} waves are the subcellular events underlying Ca^{2+} overload during ischemia and reperfusion in perfused intact hearts," *J. Mol. Cell. Card.*, vol. 79, pp. 69 – 78, 2015.

[209] H. Lodish, A. Berk, S. L. Zipursky, P. Matsudaira, d. Baltimore, and J. Darnell, *Molecular Cell Biology.* New York: W. H. Freeman, 2000.

[210] P. A. Martorana, P. Van Even, B. Wüsten, and J. Schaper, "Increase in number and decrease in size of mitochondrial profiles in myocytes of the right ventricle of dogs with experimental emphysema," *Am. Rev. Respir. Dis.*, vol. 134, pp. 580 – 584, 1985.

[211] K. N. Papanicolaou, R. J. Khairallah, G. A. Ngoh, A. Chikando, I. Luptak, K. M. O'Shea, D. D. Riley, J. J. Lugus, W. S. Colucci, W. J. Lederer, W. C. Stanley, and K. Walsh, "Mitofusin-2 maintains mitochondrial structure and contributes to stress-induced permeability transition in cardiac myocytes," *Mol. Cell. Biol.*, vol. 31, pp. 1309 – 1328, 2011.

[212] S.-B. Ong and D. J. Hausenloy, "Mitochondrial morphology and cardiovascular disease," *Cardiovasc. Res.*, vol. 88, pp. 16 – 29, 2010.

[213] H. Hoitzing, I. G. Johnston, and N. S. Jones, "What is the function of mitochondrial networks? A theoretical assessment of hypotheses and proposal for future research," *Bioessays*, vol. 37, pp. 687 – 700, 2015.

[214] J. M. Hollander, D. Thapa, and D. L. Sheperd, "Physiological and structural differences in spatially distinct subpopulations of cardiac mitochondria: influence of cardiac pathologies," *Am. J. Physiol. Heart Circ. Physiol.*, vol. 307, pp. H1 – H14, 2014.

[215] E. N. Dedkova and L. A. Blatter, "Measuring mitochodnrial function in intact cardiac myocytes," *J. Mol. Cell. Cardiol.*, vol. 52, pp. 48 – 61, 2012.

[216] M. Colombini, "VDAC: The channel at the interface between mitchondria and the cytosol," *Mol. and Cell. Biochem.*, vol. 256/257, pp. 107 – 115, 2004.

[217] J. J. Lemasters and E. Holmuhamedov, "Voltage-dependent anion channel (VDAC) as mitochondrial governator - Thinking outside the box," *BBA*, vol. 1762, pp. 181 – 190, 2006.

[218] R. A. Nafikov and D. C. Beitz, "Carbohydrates and lipid metabolism in farm animals," *J. Nutr.*, vol. 137, pp. 702 – 705, 2007.

[219] K. S. McCommis and B. N. Finck, "Mitochondrial pyruvate transport: a historical perspective and future research directions," *Biochem. J.*, vol. 466, pp. 433– 454, 2015.

[220] W. Stanley, F. A. Recchia, and G. D. Lopaschuck, "Myocardial substrate metabolism in the normal and failing heart," *Physiol. Rev.*, vol. 85, pp. 1093 – 1129, 2005.

[221] E. Barth, G. Stammler, B. Speiser, and J. Schaper, "Ultrastructural quantitation of mitochondria and myofilaments in cardiac muscle from 10 different animal species including man," *J. Mol. Cell. Cardiol.*, vol. 24, pp. 669 – 681, 1992.

[222] C. Pinali, H. Bennett, J. B. Davenport, A. W. Trafford, and A. Kitmitto, "Three-dimensional reconstruction of cardiac sarcoplasmic reticulum reveals a continous network linking transverse-tubules," *Circ. Res.*, vol. 113, pp. 1219 – 1230, 2013.

[223] A.-C. Wei, T. Liu, S. Cortassa, R. L. Winslow, and B. O'Rouke, "Mitochondrial Ca^{2+} influx and efflux rates in guinea pig cardiac mitochondria: Low and high affinity effects of cyclosporine A," *BBA*, vol. 1813, pp. 1373 – 1581, 2011.

[224] R. Palty, E. Ohana, M. Hershfinkel, M. Volokita, V. Elgazar, O. Beharier, W. F. Silverman, M. Argaman, and I. Sekler, "Lithium-calcium exchange is mediated by a distinct potassium-independent sodium-calcium exchanger," *J. Biol. Chem.*, vol. 279, pp. 25234 – 25340, 2004.

[225] L. Boyman, G. S. B. Williams, D. Khananshvili, I. Sekler, and W. J. Lederer, "NCLX: The mitochondrial sodium calcium exchanger," *J. Mol. Cell. Cardiol.*, vol. 59, pp. 205 – 213, 2013.

[226] K. Oxenoid, Y. Dong, C. Cao, T. Cui, Y. Sancak, A. L. Markhard, Z. Grabarek, L. Kong, Z. Liu, B. Ouyang, Y. Cong, V. K. Mootha, and J. J. Chou, "Architecture of the mitochondrial calcium uniporter," *Nature*, vol. 533, pp. 269 – 273, 2016.

[227] G. W. Dorn II and C. Maack, "SR and mitochondria: calcium cross-talk between kissing cousins," *J. Mol. Cell. Cardiol.*, vol. 5, pp. 42 – 49, 2013.

[228] S. G. Tewari, Y. Zhou, B. J. Otto, R. K. Dash, W.-M. Kwok, and D. A. Beard, "Markov chain Monte Carlo based analysis of post-translationally modified VDAC gating kinetics," *Frontiers in Physiol.*, vol. 5, pp. 1–10, 2014.

[229] J. Kerner, K. Lee, B. Tandler, and C. L. Hopper, "VDAC proteomics: post-translation modifications," *BBA*, vol. 1818, pp. 1502 – 1525, 2012.

[230] K. W. Kinnally, M. L. Campo, and H. Tedeschi, "Mitochondrial channel activity studied by patch- clamping mitoplasts," *J. Bioenerg. Biomembr.*, vol. 21, pp. 497 – 506, 1989.

[231] Y. Kirichock, G. Krapivinsky, and D. E. Clapham, "The mitochondrial calcium uniporter is a highly selective ion channel," *Nature*, vol. 427, pp. 360 – 364, 2004.

[232] M. S. Jafri, S. J. Dudycha, and B. O'Rourke, "Cardiac energy metabolism: models of cellular respiration," *Annu. Rev. Biomed. Eng*, vol. 3, pp. 57 – 81, 2001.

[233] S. V. Lemeshko and V. V. Lemeshko, "Metabolically derived potential on the outer membrane of mitchondria: A computational model," *Biophys. J.*, vol. 79, pp. 2785 – 2800, 2000.

[234] D. A. Beard, "A biophysical model of mitochondrial respiratory system and oxidative phosphorylation," *PLoS Comp. Biol.*, vol. 1, pp. 0252 – 0264, 2005.

[235] F. Wu, F. Yang, K. C. Vinnakota, and D. A. Beard, "Computer modeling of mitochondrial tricarboxylic acid cycle, oxidative phoshorylation, metabolite transport, and electrophysiology," *J. Bio. Chem.*, vol. 282, pp. 24525 – 24537, 2007.

[236] L. Yang, P. Korge, J. N. Weiss, and Z. Qu, "Mitochondrial oscillations and waves in cardiac myocytes: insights from computational models," *Biophys. J.*, vol. 98, pp. 1428 – 1438, 2010.

[237] B. O'Rouke and L. A. Blatter, "Mitochondrial Ca^{2+} uptake: Tortoise or hare?," *J. Mol. Cell. Cardiol.*, vol. 46, pp. 767 – 774, 2009.

[238] S. Boncompagni, A. E. Rossi, M. Micaroni, G. V. Beznoussenko, R. S. Polishchuk, R. T. Dirksen, and F. Protasi, "Mitochondria are linked to calcium stores in striated muscle by developmentally regulated tethering structures," *Mol. Biol. Cell.*, vol. 20, pp. 1058 – 1067, 2009.

[239] G. Báthori, G. Csordás, C. Garcia-Perez, E. Davies, and G. Hajnoóczky, "Ca^{2+}-dependent control of the permeability properties of the mitochondrial outer membrane and voltage-dependent anion-selective channel (VDAC)," *J. Biol. Chem.*, vol. 281, pp. 17347 – 17358, 2006.

[240] S. Cortassa, M. A. Aon, B. O'Rouke, R. Jacques, H. Tseng, E. Marbán, and R. L. Winslow, "A computational model integrating electrophysiology, contraction, and mitochondrial bioenergetics in the ventricular myocyte," *Biophys. J.*, vol. 91, pp. 1564 – 1589, 2006.

[241] R. K. Dash, F. Qi, and D. A. Beard, "A biophysically based mathematical model for the kinetics of mitochondrial calcium uniporter," *Biophys. J.*, vol. 96, pp. 1318 – 1332, 2009.

[242] R. K. Pradhan, D. A. Beard, and R. K. Dash, "A biophysically based mathematical model for the kinetics of mitochondrial Na^+-Ca^{2+} antiporter," *Biophys. J.*, vol. 98, pp. 218 – 230, 2010.

[243] V. V. Lemeshko, "Model of the outer membrane potential generation by the inner membrane of mitochondria," *Biophys. J.*, vol. 82, pp. 684 – 692, 2002.

[244] V. V. Lemeshko, "VDAC electronics: 2. A new, anaerobic mechanism of generation of the membrane potentials in mitochondria," *BBA*, vol. 1838, pp. 1801 – 1808, 2014.

Erklärung zum Eigenanteil an der Dissertationsschrift

Das Zellmodel, welches in der vorliegenden Arbeit vorgestellt, (weiter)entwickelt und für Analysen verwendet wurde, besteht aus drei Teilen. Das CRU-Model wurde von Thomas Schendel und Wilhelm Neubert erstellt. Das Elektrophysiologie-Model wurde von Mahajan et al. veröffentlicht. Die Dynamik der Volumenkonzentrationen wird durch ein System partieller Differentialgleichungen beschrieben, das mit Finite-Element-Methoden integriert wird, die von Nagaiah Chamakuri und Wilhelm Neubert auf der Grundlage der DUNE C++-Bibliothek implementiert wurden.
Nagaiah Chamakuri, Stephen Gilbert, Wilhelm Neubert und ich verbesserten kontinuierlich das Model. Die Federführung in Bezug auf numerische Methoden oblag dabei Nagaiah Chamakuri und Wilhelm Neubert. Stephen Gilbert und ich waren zu gleichen Teilen für die Parameterisierung und die biologischen Aspekte zuständig.
Im dritten Kapitel stelle ich die Konzeption, Literaturrecherche, Implementierung, Datenauswertung und die Ergebnisdiskussion für das RyR-Modelles vor. Dieses Kapitel war eine Zusammenarbeit mit Stephen Gilbert. Die Simulationsergebnisse des dritten Kapitels führten zur Festlegung der RyR-bezogenen Parameter.
Alle im vierten Kapitel beschriebenen Simulationen sind eigenständig konzipiert, durchgeführt, graphisch dargestellt und analysiert worden inklusive der notwendigen Gleichungs- und Parameteranpassungen. Die Ergebnisse führten auch zu weiteren Anpassungen der Parameter.
Im fünften Kapitel implementierte ich einen räumlich aufgelösten Natrium-Kalzium-Austauscher. Nagaiah Chamakuri untersützte mich bei den numerischen Methoden und überprüfte die mathematische Richtigkeit. Die Simulationen und Analysen führte ich eigenständig durch.
Im sechsten Kapitel implementierte ich das Mitochondrienmodell von Magnus und Keizer in C++ und verband dieses mit dem bereits existierenden Mahajan-Model. Die Simulationen und Analysen in diesem Kapitel führte ich eigenständig durch. Ich integrierte das Mitochondrienmodell in Zusammenarbeit mit Nagaiah Chamakuri und Wilhelm Neubert in das Ganzzell-Modell.

List of publications

1.) J. Vierheller
Exploratory Data Analysis.
In: Lamprecht, A. L., Margaria, T. (eds.) Process Design for Natural Scientists. CCIS, vol. 500, pp. 110 - 126, Springer, Heidelberg, (2014)

2.) N. Bordag, S. Klie, K. Jürchott, J. Vierheller, H. Schiewe, V. Albrecht, J.-C. Tonn, C. Schwartz, C. Schichor, and J. Selbig
Glucocorticoid (dexamethasone)-induced metabolome changes in healthy males suggest prediction of response and side effects.
Scientific Reports, vol. 5, pp. 1- 12, (2015)

3.) J. Vierheller*, W. Neubert, M. Falcke, S. H. Gilbert, and N. Chamakuri*
A multiscale computational model of spatially resolved calcium cycling in cardiac myocytes: from detailed cleft dynamics to the whole cell concentration profiles.
Front. Physiol., vol. 6, pp. 1 - 15 (2015)

4.) N. Chamakuri, W. Neubert, S. Gilbert, J. Vierheller, G. Warnecke, M. Falcke
Multiscale modeling and numerical simulation of calcium cycling in cardiac myocytes
In review

*contributed equally

Acknowledgement

I would like to thank my supervisors Prof. Martin Falcke, and Prof. Hermann-Georg Holzhütter for giving me the opportunity to work on this fascinating, complex project and for their support, their advice, and patient guidance.
Moreover, I am grateful for the financial support of the German Research Foundation (DFG) via the GRK 1722 and GRK 1558, which allowed me to undertake this research and to attend conferences and workshops. I want to thank especially the coordinator of the GRK 1722, Prof. Edda Klipp who makes the graduate school such a great, interdisciplinary success. I am grateful for the vivid, encouraging and inspiring atmosphere of the graduate schools.
I want to thank the former and current members of the Mathematical Cell Physiology group at the MDC. Special thanks go to PhD Stephen Gilbert, Wilhelm Neubert and Prof. Nagaiah Chamakuri who constantly improved with me the model and provided a lot of help and input. I also want to thank Dr. Wolfgang Giese for his editorial advices and the cooperator PhD Johann Schreddelseker for his lively discussion about mitochondria.
I must express my very profound gratitude to my parents and to my fiancé Marcus Straka for having faith in me, providing me with unfailing support and continuous encouragement throughout my years of study and through the process of researching and writing this thesis.
I also want to thank my friends Dr. Kathleen Garz, Annika Busse, Christin Hoffmann and Dr. Stefan Reschke for their careful editing, moral support, and encouragement. This accomplishment would not have been possible without them. Thank you.

Selbstständigkeitserklärung

Hiermit erkläre ich, dass ich die vorliegende Arbeit selbstständig und nur mit den angegebenen Hilfen und Hilfsmitteln angefertigt zu habe.

Berlin, den 19.10.2017 Janine Vierheller